Single-component multilayered self-assembling nanoparticles presenting rationally designed glycoprotein trimers as Ebola virus vaccines

Linling He[1*], Anshul Chaudhary[1*], Xiaohe Lin[1*], Cindy Sou[1], Sonu Kumar[1], Timothy Ngo[1], Ezra Kosviner[1], Robyn L. Stanfield[1], Ian A. Wilson[1†], and Jiang Zhu[1,2†]

[1]Department of Integrative Structural and Computational Biology, [2]Department of Immunology and Microbiology, [3]Skaggs Institute for Chemical Biology, The Scripps Research Institute, La Jolla, California 92037, USA

[*] These authors contributed equally to this work

[†] Co-corresponding authors (to whom correspondence should be addressed)

IAW: Phone (858) 784-9706; Email: wilson@scripps.edu

JZ: Phone (858) 784-8157; Email: jiang@scripps.edu

KEYWORDS

Ebola virus (EBOV) vaccine; glycoprotein (GP); nanoparticle vaccine; GP2 stalk; heptad repeat 1-C ($HR1_C$); viral hemorrhagic fever (VHF)

TEASER (130 characters)

We rationally redesigned the EBOV glycoprotein and engineered single-component multilayered nanoparticles as vaccine candidates

ABSTRACT (150 words)

The Ebola virus (EBOV) glycoprotein (GP) can be recognized by neutralizing antibodies (NAbs) and is the main target for vaccine design. We first investigated the contribution of the stalk and the heptad repeat 1-C ($HR1_C$) region to GP metastability. Specific stalk and $HR1_C$ modifications in a mucin-deleted form (GPΔmuc) increased trimer yield, while alteration of $HR1_C$ exerted a more complex effect on thermostability. Crystal structures were determined to validate these rationally designed GPΔmuc trimers in their unliganded state. We then displayed a modified GPΔmuc trimer on engineered nanoparticles with encapsulated locking domains (LD) and a cluster of helper T-cell epitopes. In mice and rabbits, GP trimers and nanoparticles elicited cross-ebolavirus NAbs as well as non-NAbs that enhance in-vitro infection. Next-generation sequencing (NGS) revealed B-cell profiles that are specific to vaccine platforms. This study provides insight into GP metastability and paves the way for development of an effective, pan-ebolavirus nanoparticle vaccine.

INTRODUCTION

The Ebola virus (EBOV), a member of the *Ebolavirus* genus in the *Filoviridae* family (*1*), can cause a severe human disease known as viral hemorrhagic fever (VHF) (*2, 3*). EBOV was solely responsible for the largest filovirus outbreak in history during 2013-2016, which spread across nine African countries with 28,600 cases and 11,325 deaths (*4*). A further EBOV outbreak in 2019 led to 2103 deaths (*5*) and was declared an international emergency on July 17, 2019 by the World Health Organization (WHO). In recent years, significant progress has been made to counter this deadly virus. Neutralizing antibodies (NAbs) have now been established as effective therapeutics for EBOV infection (*6-9*), as demonstrated by the ZMapp cocktail of murine chimeric antibodies (*10, 11*), as well as human antibodies (*12, 13*). Vaccines based on diverse delivery systems have been tested in humans (*14-17*), of which rVSV-ZEBOV – a replication-competent recombinant vesicular stomatitis virus (VSV) expressing a *Zaire* EBOV glycoprotein (GP) (*18-21*) – is the most advanced vaccine candidate that was deployed during the 2018-2019 outbreak. However, GP-specific antibody titers were not noticeably increased seven days after vaccination with rVSV-ZEBOV in humans (*15, 22*), in contrast to prior findings in nonhuman primates (NHPs) (*23*). In addition, a recent study reported neurotropism of rVSV-ZEBOV that resulted in damage to the eye and brain in neonatal mice (*24*). Antibody-dependent enhancement (ADE) of infection was also found for EBOV antibodies isolated from human survivors (*25*), suggesting that weak/non-NAbs induced by a suboptimal vaccine may cause adverse effects. Currently, no EBOV vaccine has been approved by the U.S. Food and Drug Administration (FDA) for use in humans.

EBOV GP, a trimer of GP1-GP2 heterodimers responsible for cell entry (*26*), is recognized by the humoral immune system during natural infection (*27-29*). The 2013-2016 outbreak led to an ongoing campaign to identify and characterize NAbs for EBOV (*30*) and other filoviruses such

as Marburg virus (MARV) (*31-33*). As a result, large panels of NAbs were isolated from human survivors, vaccinated humans, and immunized animals (*12, 34-39*). Crystallography (*40-43*) and electron microscopy (EM) (*44-47*) have revealed multiple sites of vulnerability on EBOV GP. A recent study of 171 monoclonal antibodies (mAbs) defined eight classes of epitopes (*48*), six of which can be recognized by broadly neutralizing antibodies (bNAbs) (*9*). Over the last decade, HIV-1 vaccine research has been driven largely by an antibody-based strategy focusing on bNAb identification, structural analysis of bNAb-envelope glycoprotein (Env) interactions, and rational immunogen design (*49, 50*). An important milestone in recent HIV-1 vaccine research was the development of native-like Env trimers, which have emerged as a promising platform for HIV-1 vaccine design (*51, 52*). In contrast to the growing number of EBOV (b)NAbs and their structures with GP, little attention has been given to the rational design of EBOV GP. As class-I viral fusion proteins (*53, 54*), HIV-1 Env and EBOV GP are inherently metastable, which is a property that has been studied in depth for HIV-1 Env (*55-57*), but not yet for EBOV GP. Another advance in the HIV-1 vaccine field was to display stabilized Env trimers on self-assembling nanoparticles (NPs) (*58, 59*). While recombinant virus-like particles (VLPs) can protect against EBOV challenge in animals (*60-62*), the difficulties in manufacturing have hampered their further development as human vaccines (*63*). Therefore, display of stabilized GP trimers on NPs may provide a promising solution for developing VLP-type EBOV vaccines, but this possibility has yet come to fruition.

In this study, we explore the causes of EBOV GP metastability and design multilayered NP vaccines for in vivo evaluation. To facilitate GP purification, we developed an immunoaffinity column based on mAb100 (*12, 42*) that is specific for native-like, trimeric GP. We first examined the contribution of two regions in GP2, namely, the stalk and the heptad repeat 1-C ($HR1_C$) region, to GP metastability in a mucin-deleted *Zaire* EBOV GP construct (GPΔmuc). We extended the

soluble GP ectodomain (GP_{ECTO}) in the stalk region from residue 632 (C terminus of HR2) to 637 and introduced a W615L mutation based on comparison of EBOV and MARV GPs. We also assessed eight proline mutations in $HR1_C$, a region equivalent to the HR1 bend that is essential to HIV-1 Env metastability (*55-57*), for their ability to prevent GP transition from pre- to post-fusion states. While both stalk and $HR1_C$-proline mutations increased trimer yield, the latter exhibited a more complex effect on GP thermostability. In addition, newly engineered inter-protomer disulfide bonds (SS) were found to increase the trimer stability. Crystal structures were determined for two redesigned GPΔmuc constructs to validate the stalk and $HR1_C$-proline mutations on an atomic level. We then displayed a redesigned GPΔmuc trimer on ferritin, E2p, and I3-01 NPs. Locking domains (LD) and helper T-cell epitopes were incorporated into E2p and I3-01 60-mers (*55, 64*) to stabilize the NP shell from the inside and to create multilayered NP carriers. In mice and rabbits, GP trimers and NPs induced distinct antibody responses with enhanced pseudoviral infection observed for some vaccines. Next-generation sequencing (NGS) of GP-specific B cells revealed different patterns for NPs that presented large trimeric spikes versus smaller antigens, such as hepatitis C virus (HCV) E2 core (*65*). Our study thus reports on the critical factors for EBOV GP metastability, single-component multilayered self-assembling NPs for development of VLP-type vaccines, and vaccine candidates that warrant further evaluation in NHPs and humans.

RESULTS

Tag-free immunoaffinity purification of EBOV GP trimers

EBOV GP contains a heavily glycosylated mucin-like domain (MLD), which shields the glycan cap and neutralizing epitopes in GP1 and GP2 (**Fig. 1A**). A soluble, mucin-deleted form of *Zaire* EBOV GP (GPΔmuc) that produced the first (*40*) and later high-resolution (*66*) crystal structures was used as a basic construct to investigate GP metastability (**Fig. 1A**). In HIV-1 vaccine research,

immunoaffinity chromatography (IAC) columns based on bNAbs 2G12 and PGT145 (*67*, *68*) have been widely used for the purification of native-like Env trimers. While 2G12 targets a glycan patch on a single gp120, PGT145 binds the trimer apex and can separate closed trimers from partially open and misfolded Envs. These two bNAb columns have also been used to purify HIV-1 gp140-presenting NPs (*55*, *64*, *69*). Similarly, GP-specific antibody columns may prove useful for EBOV vaccine research. Corti et al. recently identified two potent NAbs, mAb114 and mAb100, from a human survivor (*12*). Misasi et al. elucidated the structural basis for neutralization by mAb114, which targets the receptor binding site (RBS), and mAb100, which interacts with the GP1/GP2 interface and internal fusion loop (IFL) of two GP protomers (*42*). Here, we examined the utility of mAb114 and mAb100 in IAC columns. The GPΔmuc constructs with and without a C-terminal foldon trimerization motif were transiently expressed in 250 ml HEK293F cells and purified on an antibody column prior to size-exclusion chromatography (SEC) using a Superdex 200 10/300 GL column and blue native polyacrylamide gel electrophoresis (BN-PAGE). With mAb114, both GPΔmuc samples showed aggregate (~9ml), dimer (~12ml), and monomer (~13.5-14ml) peaks in the SEC profiles, but only GPΔmuc-foldon showed a visible trimer peak (~10.5-11ml) in SEC and a faint band of slightly less than 440 kD on the BN gel (**Fig. 1B**). Following mAb100 purification, GPΔmuc produced low overall yield, whereas GPΔmuc-foldon demonstrated high trimer purity with no dimer and monomer peaks. Consistently, GPΔmuc-foldon registered a single trimer band on the BN gel (**Fig. 1C**). Taken together, while both mAb114 and mAb100 can be used to purify GP, mAb100 offers an effective IAC method for purifying native-like trimers due to its recognition of a quaternary epitope. The stark difference in trimer yield between the two GPΔmuc constructs after mAb100 purification suggests a strong tendency for trimer dissociation without foldon.

Effect of the HR2 stalk on EBOV GP metastability

Previously, we demonstrated that the gp41 ectodomain ($gp41_{ECTO}$) is the source of HIV-1 Env metastability (*55*). Unlike HIV-1 Env (*70, 71*), in which the gp41 HR2 helix is packed against the bottom of the gp41 HR1 helix and the gp120 C1/C5 loops and forms extensive interactions at the trimer base (*70, 71*), EBOV GP possesses a long, extended HR2 stalk (**Fig. 1A**, right). Even in the high-resolution GPΔmuc structures (*66, 72, 73*), the HR2 stalk still contains less helical content than most coiled-coils in the Protein Data Bank (PDB), ~15 aa vs ~30 aa, and becomes less regular and unwound towards the C terminus, suggesting an inherent instability in HR2 (**Fig. 1D**, left). Recently, King et al. solved a 3.17 Å-resolution structure for the MARV GPΔmuc trimer in complex with a therapeutic human mAb, MR191 (*32*). Surprisingly, the MARV HR2 stalk adopted a well-formed coiled-coil with canonical sidechain packing along the three-fold axis (**Fig. 1D**, right). To identify the cause of this difference, we obtained EBOV and MARV GP sequences from the Virus Pathogen Database and Analysis Resource (ViPR, https://www.viprbrc.org). A total of 274 EBOV GPs and 87 MARV GPs were used for sequence conservation analysis of the region spanning the CX_6CC motif and the HR2 stalk, aa 601-632 for EBOV and aa 602-633 for MARV, respectively (**Fig. 1D**, middle). Most inward-facing amino acids were conserved except for W615 in EBOV, and L616 in MARV. Indeed, structural analysis revealed a critical difference at this position: the three W615s in EBOV GP (PDB: 5JQ3) formed a wide triangle at the neck of the coiled-coil with a Cα distance of 11.1 Å and a Cβ distance of 9.0 Å; in contrast, with the smaller and more hydrophobic L616, a Cα distance of 10.5 Å and a Cβ distance of 8.3 Å were observed in MARV GP (PDB: 6BP2). This finding suggests that a W615L mutation may stabilize the EBOV GP trimer. To further examine the effect of the HR2 stalk, we created three GPΔmuc constructs by replacing aa 617-632 with a GCN4 leucine zipper (PDB: 2WPZ, aa 3-33) and by extending the C terminus to D637 and N643 to include a newly identified bNAb epitope (*74*) that spans HR2

and the membrane-proximal external region (MPER), termed "L" and "Ext", respectively (**fig. S1A**). D637 is also important for proteolytic cleavage by tumor necrosis factor alpha-converting enzyme (TACE), which causes GP to shed from the surface of the virus (*75*). Of note, a double mutation (P612G/W615F) was introduced to the GPΔmuc-2WPZ construct between the upstream CX_6CC motif and the HR2 coiled-coil to reduce the structural strain. These three constructs were characterized by SEC and BN-PAGE following transient expression in 250-ml 293 F cells and mAb114 purification. Indeed, all three designs increased trimer yield with GPΔmuc-2WPZ showing the most visible trimer peak in SEC (**fig. S1B**). Consistently, trimer bands were observed for all three constructs on the BN gel when purified with mAb100, albeit with less intensity for GPΔmuc-L and -Ext (**fig. S1C**, left). Upon mAb100 purification, all three GPΔmuc variants showed more visible trimer bands than wildtype GPΔmuc (**fig. S1C**, right), supporting the notion that the HR2 stalk is critical to GP trimer stability.

We next combined the W615L mutation and the "L" extension in a single construct named GPΔmuc-W615L-L-foldon, or simply GPΔmuc-WL^2-foldon (**Fig. 1E**). This construct, along with GPΔmuc-foldon, was expressed transiently in 1-liter 293 F cells and purified using an mAb100 column prior to SEC on a HiLoad Superdex 200 16/600 GL column (**Fig. 1F**). In three production runs, GPΔmuc-WL^2-foldon consistently outperformed the wildtype construct, showing a two-fold higher trimer peak in the SEC profile and an ~2.6-fold greater trimer yield after SEC (1.3 mg vs 0.5 mg). Thermostability was assessed by differential scanning calorimetry (DSC) for two purified GP trimers (**Fig. 1G**). The thermal denaturation midpoint (T_m) value of the stalk-stabilized trimer was 3 ºC higher than that of the wildtype trimer (67 ºC vs 64 ºC). Consistently, stalk stabilization also increased the onset temperature (T_{on}) from 52.4 ºC to 62.5 ºC, with a narrower half width of the peak ($\Delta T_{1/2}$) than the wildtype trimer (3.8 ºC vs. 5.1 ºC). Antigenicity was assessed for four

mAb100/SEC-purified EBOV GP trimers in enzyme-linked immunosorbent assay (ELISA) (**Fig. 1H** and **fig. S1, D to E**). Ten antibodies were tested, including three NAbs targeting the base (KZ52 (*76*), c2G4 and c4G7 (*10*)), two human NAbs (*12*) – mAb100 (IFL) and mAb114 (RBS), a non-NAb directed to the glycan cap (c13C6 (*10*)), and four pan-ebolavirus bNAbs targeting the HR2-MPER epitope (BDBV223 (*74*)) and IFL (ADI-15878, ADI-15946 (*37, 38*), and CA45(*36*)). The GPΔmuc trimer showed notably improved antibody binding with respect to the GP_{ECTO} trimer with an up to 7.6-fold difference in half maximal effective concentration (EC_{50}), indicating that MLD can shield much of the GP from antibody recognition. The two HR2 stalk modifications led to slightly increased recognition of RBS by mAb114 and IFL by CA45, respectively, although the EC_{50} values only showed moderate changes. A 40% reduction in EC_{50} was observed for GPΔmuc-WL^2-foldon binding to BDBV223, confirming that the C terminal extension into MPER can indeed improve the recognition of this conserved bNAb epitope at HR2-MPER (*74*). King et al. proposed two scenarios for EBOV GP to expose the BDBV223 epitope: one HR2 helix is splayed apart from the coiled-coil or the whole GP is lifted/tilted from the membrane (*74*). It is perhaps more plausible that EBOV GP may adopt an "open stalk" similar to the parainfluenza virus 5 (PIV5) fusion (F) protein, which has a similar long HR-B stalk (*77*). Taken together, these two HR2 stalk mutations can improve trimer yield, thermostability, and antigenicity for EBOV GP.

Effect of the $HR1_C$ bend on EBOV GP metastability

Structures of the prefusion glycoprotein and the postfusion six-helix-bundle have been determined for HIV-1 Env (*70, 71, 78*) and EBOV GP (*40, 79*). In a previous study (*56*), we identified the N terminus of HR1 ($HR1_N$, aa547-569) as a major cause of HIV-1 Env metastability, as this region undergoes a drastic conformational change during fusion. We and others have stabilized diverse HIV-1 Envs by replacing the 22-aa $HR1_N$ with an optimized 8-aa loop (*55-57, 80*). The equivalent

region in EBOV GP (aa576-583), $HR1_C$ (*40*), forms a 21-nm triangular interior at around the two-thirds of the height of the chalice that spans 94-Å wide at the rim (**Fig. 2A**). This prefusion $HR1_C$ bend will refold to two helical turns in the center of a long helix in the postfusion state (**Fig. 2B**, left). Here, we hypothesized that $HR1_C$ is essential to EBOV GP metastability. Since $HR1_C$ in wildtype EBOV GP is equivalent in length (8 aa) to a truncated engineered $HR1_N$ in the prefusion-optimized HIV-1 Env (*55, 56*), metastability in EBOV GP may not be as sensitive to $HR1_C$ length and likely requires a different solution. We thus hypothesized that proline mutation to one of the eight residues in $HR1_C$, termed P^1 to P^8, may rigidify the $HR1_C$ bend and improve EBOV GP trimer stability (**Fig. 2B**, right). Similar proline mutations in $HR1_N$ have effectively stabilized HIV-1 Env trimers (*56, 68*). To examine this possibility, eight GPΔmuc-W615L variants, each with a proline mutation in $HR1_C$, but without the L extension and C-terminal foldon, were tested experimentally. All constructs were transiently expressed in 250-ml 293 F cells and purified using an mAb114 column. The proline mutation at most positions in $HR1_C$ showed little effect on the distribution of GP species except for T577P (P^2) and L579P (P^4), which displayed evidence for a trimer peak at ~11ml in the SEC profiles (**Fig. 2C**). In a separate experiment, all eight constructs were transiently expressed in 250-ml 293 F cells and purified using an mAb100 column. Only P^2 and P^4 produced any measurable trimer yield, with a higher SEC peak observed for P^2 that corresponds to well-formed trimers (**Fig. 2C**). The mAb100-purified GP was analyzed by BN-PAGE, which showed a trimer band for P^2 and P^4 (**Fig. 2D**). Overall, the T577P mutation (P^2) can considerably increase trimer yield, while the L579P mutation (P^4) exhibits a less pronounced effect.

Next, the T577P mutation (P^2) was incorporated into the GPΔmuc-WL^2-foldon construct, resulting in a construct named GPΔmuc-WL^2P^2-foldon. This construct was expressed transiently

in 1-liter 293 F cells and purified using an mAb100 column for SEC characterization on a HiLoad Superdex 200 16/600 GL column. In three production runs, GPΔmuc-WL^{2}P^2-foldon generated a trimer peak that was two- and four-fold higher than GPΔmuc-WL^2-foldon and wildtype GPΔmuc-foldon, respectively, with an average yield of 2.6 mg after SEC (**Fig. 2E**, left). Protein collected in the range of 55.5-62.0 ml was analyzed by BN-PAGE, which displayed a trimer band across all fractions without any hint of impurity (**Fig. 2E**, right). The thermostability of GPΔmuc-WL^{2}P^2-foldon was determined by DSC after mAb100 and SEC purification. Unexpectedly, two transition peaks were observed in the thermogram, one registered at a lower T_m of 61.6 ºC and the other at a higher T_m of 68.2 ºC (**Fig. 2F**, left). To this end, a second construct bearing the L579P mutation (P^4), termed GPΔmuc-WL^{2}P^4-foldon, was also assessed by DSC (**Fig. 2F**, right). Although only one peak was observed in the thermogram with a T_m of 67.0 ºC, a slight widening at the onset of the peak suggested a similar unfolding behavior upon heating. DSC thus revealed the complexity associated with a proline-rigidified HR1$_C$ bend, which may increase the trimer yield at the cost of reducing or modifying the GP thermostability profile. The antigenicity of GPΔmuc-WL^{2}P^2-foldon was assessed using the same panel of 10 antibodies by ELISA (**figs. S1F-S1G**) and bio-layer interferometry (BLI) (**Fig. 2G**). The T577P mutation (P^2) exhibited comparable antigenic profiles to GPΔmuc-WL^2-foldon (**fig. S1G**), with a 40% reduction in EC_{50} observed for bNAb BDBV223, which targets HR2-MPER. The BLI profiles were almost indistinguishable between wildtype and redesigned GPΔmuc-foldon trimers, with all having relatively fast on-rates and slow off-rates. A two-fold higher signal at the lowest concentration (12.5 nM) was observed for GPΔmuc-WL^{2}P^2-foldon binding to bNAb BDBV223 (**Fig. 2G**), consistent with the ELISA data.

Our results thus demonstrate the importance of HR1$_C$ to EBOV GP metastability and a perhaps unexpected sensitivity of HR1$_C$ to proline mutation. Recently, Rutten et al. tested proline

mutations in $HR1_C$ along with a K588F mutation to stabilize filovirus GP trimers (*81*). While a similar increase in trimer yield was observed for the T577P mutant, the reported thermostability data appeared to be inconsistent with our DSC measurement. Further investigation is warranted to fully understand the role of $HR1_C$ in filovirus-cell fusion and its impact on GP stability.

GP stabilization with disulfide bond mutations

Engineered disulfide (SS) bonds have been used to stabilize viral glycoproteins, as demonstrated for HIV-1 Env (*68*), respiratory syncytial virus (RSV) F (*82*), and Lassa virus (LASV) GP complex (GPC) (*83*). Since EBOV GP already contains an endogenous SS bond linking GP1 and GP2 (C53-C609), we examined whether inter-protomer SS bonds can be used to stabilize trimer formation and lock the GP in a "closed" trimer. Based on a high-resolution EBOV GPΔmuc structure (PDB: 5JQ3), we identified inter-protomer amino acid pairs whose C_α-C_α distances are within a cutoff of 4.72 Å as defined by Rosetta (*84*). A total of nine pairs were identified (**fig. S2A**). After visual inspection, three were removed as they may interfere with an existing SS bond or a hydrophobic cluster. The remaining six were divided into three groups: the IFL-head group (SS1/2/4), the IFL-NHR group (SS/5), and the HR2 group (SS6) (**fig. S2B**). Six GPΔmuc-SS constructs without C-terminal foldon were designed and then characterized by SEC following transient expression in 250-ml 293 F cells and mAb114 purification (**fig. S2C**). Diverse SEC profiles were observed, with SS2 showing a notable trimer peak, consistent with a band of slightly below 440 kD on the BN gel (**fig. S2D**, left). The mAb100-purified materials were also analyzed by BN-PAGE (**fig. S2D**, right), with trimer bands observed for SS2, SS3, and SS5. Antigenicity was assessed for the three SS mutants in ELISA using six antibodies (**fig. S2E-S2G**). While all three SS mutants slightly outperformed wildtype GPΔmuc, SS2 showed higher affinity for NAbs targeting the base and IFL.

In summary, a well-positioned inter-protomer SS bond can stabilize EBOV GP in a native-like trimer conformation without any loss in binding to existing NAbs.

Crystallographic analysis of redesigned EBOV GPΔmuc trimers

To understand how the stalk and $HR1_C$ mutations affect EBOV GP, we solved crystal structures for the unliganded GPΔmuc-foldon with WL^2 and WL^2P^2 at 2.3 Å and 3.2 Å, respectively (**fig. S3** and **Fig. 3**). Both proteins showed a three-lobed, chalice-like trimer structure (*40, 66*). WL^2/WL^2P^2 yielded Cα root-mean-square deviations (RMSD) of 0.92/1.57 Å (for 367/382 residues) at a single protomer level and 1.25/1.23 Å (for 1103/1145 residues) at the trimer level, respectively, to a high-resolution GP structure (PDB: 5JQ3) (*66*). WL^2P^2 yielded a more complete structure than WL^2 at the glycan cap (R302-V310) and the HR2 stalk (I627-D637) (**fig. S3** and **Fig. 3**). In the WL^2P^2 structure, the glycan cap covers the RBS with glycan moieties visible for N238/N257/N268 in GP1 and for N563 in GP2, while in the WL^2 structure for N238/N257 in GP1 and N563/N618 in GP2 (**fig. S3B**). GP1 consists mainly of β-strands which form a broad semi-circular groove that clamps the α3 helix and the β19-β20 strands in GP2 (**Fig. 3A**). The T577P mutation appeared to have a minimum effect on the conformation of the $HR1_C$ bend, as indicated by a Cα RMSD of 0.19 Å for this 8-aa segment (**Fig. 3B**, left). In the WL^2P^2 structure, the backbone carbonyl (CO) groups of R574, A575, and T576 in one protomer formed moderate-to-strong hydrogen bonds with the guanidinium moiety of the R164 side chain in an adjacent protomer, whereas only one CO-NH distance was within the 3.5 Å cutoff in wildtype GPΔmuc (*66*). We hypothesized that a bulky, inward-facing W615 at the top of the coiled-coil destabilizes the HR2 stalk and a W615L mutation would improve its packing (**Fig. 1D**). Indeed, W615L exerted a positive effect on the stalk structure (**Fig. 3B**, bottom center and right). The Cα-Cα/Cβ-Cβ distances between two W615s of adjacent protomers in wildtype GPΔmuc (*66*), 11.1/9.0 Å, were reduced to 10.1/8.0 Å and 10.6/8.2 Å in

WL^2 and WL^2P^2, respectively (**fig. S3** and **Fig. 3B**, bottom center and right). As a result, the coiled-coil region in the EBOV HR2 stalk added one more helical turn (D624-V631), thus resembling the MARV HR2 stalk (**Fig. 1D**, right). The "L" extension in the WL^2P^2 structure could be fully modeled to D637 as a well-ordered loop anchored to the C-terminal foldon motif (**Fig. 3B**, bottom center), rendering a complete HR2 stalk and partial MPER. Superposition of HR2 stalks, from R596 up to D637, yielded Cα RMSD values of 1.46 Å, 2.05 Å, and 1.85 Å with respect to EBOV-Mayinga (PDB: 5JQ3), SUDV (PDB: 3S88), and BDBV (PDB: 6EA5) GPs, respectively (**Fig. 3B**, right), suggesting inherent structural variability in the stalk of ebolavirus GP.

The WL^2P^2 structure was then compared to a recently reported *Makona* GPΔmuc structure (PDB: 6VKM, 3.5 Å) containing the T577P/K588F mutation (**fig. S4**). In total, 353 of 398 residues in the WL^2P^2 structure matched the double mutant with a Cα RMSD of 0.89 Å. A more complete cathepsin cleavage loop (between β13 and β14, aa 190-210) was modeled in WL^2P^2 than in the double mutant, showing 10 more flanking residues, five on each side, of the loop that bridges over the IFL and interacts with IFL-directed NAbs such as mAb100 (*42*). In addition, we observed more electron density for the β18 loop in the glycan cap (aa 294-310) and the stalk than was modeled in the double mutant (**fig. S4B**, top right). For the $HR1_C$ bend, WL^2P^2 showed a Cα RMSD of 0.26 Å and more favorable hydrogen bonding patterns (**fig. S4B**, bottom left). A Cα RMSD of 1.7 Å was obtained for the IFL region between the two structures (**fig. S4B**, bottom right). Lastly, the WL^2P^2 structure was docked into a panel of known GP/antibody complexes (**fig. S5A**). Overall, WL^2P^2 preserved all critical GP-antibody contacts (**fig. S5B**). The mAb100/GP complex is of most interest, as mAb100 was used for GP purification. Cryo-EM has revealed additional electron density near the mAb100 light chain that likely corresponds to portions of the cathepsin cleavage loop (*42*), but this density was not observed in a 6.7 Å-resolution crystal structure of the same

complex (PDB: 5FHC) (*42*). In the WL^2P^2 structure, the flanking region on the β13 side was modeled to H197 (**fig. S4**), which would be in the proximity of mAb100 light chain in the docked WL^2P^2/mAb100 model. Collectively, our structures validated the rationally designed mutations, in addition to providing atomic details for some regions that were not present in previous structures. The WL^2P^2 structure also provides an explanation for the increased trimer yield, where more favorable inter-protomer hydrogen bonds are formed, although the fundamental cause of the two-peak thermogram remains unclear.

Display of EBOV GPΔmuc trimers on multilayered hyperstable nanoparticles

It is well known that a minimum of 20-25 epitopes spaced by 5-10 nm can effectively activate B cells in vivo (*85*). VLPs are intrinsically immunogenic due to their large size and dense display of antigens and are more suitable for direct uptake by dendritic cells (DC) and clustering of B cell receptors (BCRs) (*86*). Although recombinant VLPs can protect animals against EBOV challenge (*60-62*), they may not be optimal vaccine candidates due to their abnormal structure (14 μm-long viral filaments) and manufacturing difficulties (*63*). Self-assembling protein NPs thus provide an alternative to recombinant VLPs for vaccine development (*58, 59*). Previously, we displayed HIV-1 Env trimers on 24- and 60-meric NPs, which elicited tier-2 NAb responses more effectively than trimers in mice and rabbits (*55, 64*). We also reported NPs presenting an optimized HCV E2 core and demonstrated cross-genotype NAb responses in mice (*65*). Here, we tested these protein NPs as "multivalent carriers" to display redesigned GPΔmuc trimers for in vivo assessment.

To explore this possibility, we modeled the GPΔmuc trimer on ferritin (FR), E2p, and I3-01, resulting in GP-presenting NPs with diameters of 34.5 nm, 45.9 nm, and 49.2 nm, respectively (**Fig. 4A**). Superposition of the GPΔmuc C termini onto the FR and E2p N termini yielded Cα

RMSD values of 7.0 Å and 5.5 Å, suggesting that GPΔmuc can be fused to FR with a short G_4S linker and to E2p without linker, respectively. However, the large spacing between the N termini of I3-01 subunits (~50.5 Å) requires a long linker to connect with the C termini of a GPΔmuc trimer, which form a long, narrow stalk. Based on computational modeling, a 10-aa $(G_4S)_2$ linker would suffice and result in a Cα RMSD of 0.8 Å. Here, we first displayed two GPΔmuc trimers, wildtype and WL^2P^2, on FR, E2p, and I3-01 with a 5-aa linker, no linker, and a 10-aa linker, respectively. All six constructs were transiently expressed in 100-ml ExpiCHO cells followed by mAb100 purification and SEC on a Superose 6 10/300 GL column (**Fig. 4B**). WL^2P^2 outperformed wildtype GPΔmuc with greater NP yield and purity. Based on molecular weight (m.w.), the SEC peaks at ~15 ml correspond to the unassembled GP-NP species, suggesting an inherent instability for wildtype E2p and I3-01. The mAb100-purified GPΔmuc-WL^2P^2-presenting NP samples were further analyzed by negative stain EM (**Fig. 4C**), showing NPs mixed with impurities.

Previously, we demonstrated the use of a pan-reactive T-cell epitope as both a linker and as a built-in T-cell help in an HIV-1 NP construct based on I3-01 (*55*), suggesting that additional structural and functional components can be incorporated into such large 60-mers. Here, we sought to stabilize the E2p and I3-01 NPs via engineering. To this end, we fused a dimeric locking domain (LD) to the C terminus of an NP subunit, and then a T-cell epitope to the C terminus of an LD (**Fig. 4D**). We hypothesized that LD can stabilize the non-covalent NP-forming interface and the T-cell epitopes can form a cluster at the NP core to elicit a strong T-cell response upon vaccination. To test this hypothesis, we selected nine LDs of 100 residues or less from 815 homodimers in PDB (**fig. S6A**). Based on structural modeling, LDs 1-7 were tested for E2p and five LDs (4-5 and 7-9) were tested for to I3-01, all displaying GPΔmuc-WL^2P^2. Following transient expression in 100-ml ExpiCHO cells and mAb100 purification, 12 LD-containing NP samples were characterized by

SEC (**Fig. 4E**). Notably, LD4 and LD7 increased the NP peak (UV_{280} value) by 5- and 2.5-fold for E2p and I3-01, respectively, with substantially improved NP purity. Further incorporation of a T-cell epitope, PADRE, did not alter E2p properties but negatively impacted I3-01 (**Fig. 4F**). An I3-01 variant, termed I3-01v9 (or 1VLW-v9 (*55*)), could retain NP yield and purity (**Fig. 4F**). A total of seven GP-NP samples, with three variants for each 60-mer, were further analyzed by BN-PAGE (**Fig. 4G**). FR and two E2p variants displayed a single high m.w. band corresponding to well-formed NPs, whereas wildtype E2p and all three I3-01 samples showed additional low m.w. bands at 232-440 kD on the gel, indicative of unassembled GP-NP species. The mAb100/SEC-purified GPΔmuc-WL^2P^2-presenting FR, E2p-LD4-PADRE (E2p-L4P), and I3-01v9-LD7-PADRE (I3-01v9-L7P) samples were analyzed by negative stain EM (**Fig. 4H**). In addition to well-formed NPs for all three samples, an array of GPΔmuc spikes could be seen on the surface of FR and E2p-L4P NPs, consistent with SEC and BN-PAGE. Antigenicity was assessed for the three NPs by ELISA against the same antibody panel (**Fig. 4I** and **fig. S6**, **B** and **C**). Compared to the WL^2P^2 trimer, these NPs exhibited an epitope-specific binding pattern. Overall, multivalent display on NPs improved antibody recognition of the RBS and glycan cap in GP1 and reduced antibody binding for bNAbs targeting the base and IFL at the GP1/GP2 interface and the GP2 stalk. This finding raised some concerns that these conserved bNAb epitopes at the GP base and IFL on the NP-displayed trimers may not be as accessible as on the soluble trimers. To this end, BLI was performed to further probe antibody recognition of various GP epitopes (**Fig. 4J** and **fig. S6, D** to **G**). Using comparable molar concentrations of GP, the three NPs showed notably higher binding signals than the soluble trimer (**Fig. 4J**), suggesting that GP-presenting NPs may be more effective in promoting BCR clustering due to the avidity effect. Based on these findings, FR, E2p-

L4P, and I3-01v9-L7P NPs presenting a redesigned GPΔmuc trimer were selected for in vivo evaluation.

Immunogenicity of EBOV GP trimers and NPs in BALB/c mice

We immunized BALB/c mice four times with three-week intervals to obtain an initial readout of immunogenicity for three EBOV GP/GPΔmuc trimers and three NPs (**Fig. 5A**). A soluble GP_{ECTO} trimer, GP-foldon, was included to represent the wildtype GP (with MLD) used by EBOV vaccines in clinical testing (*14-17*). For the I3-01v9-L7P group, mice were immunized with 20μg mAb100-purified protein instead of 50μg mAb100/SEC-purified protein due to the low yield of this NP. We first assessed the GP-specific antibody response in mouse sera using GPΔmuc-WL^2P^2-1TD0 as a probe, which utilized trimerization motif 1TD0 (PDB: 1TD0) (**Fig. 5B** and **fig. S7, A** to **C**). Both GPΔmuc groups significantly outperformed the GP_{ECTO} group throughout the immunization with P values < 0.0064 (**Fig. 5B**, top), suggesting that MLD can shield GP from antibody recognition. In contrast, little difference was found between the two GPΔmuc groups, with WL^2P^2 showing a slightly higher average EC_{50} titer at w2 and w5 that was reversed at later time points. Compared to the GPΔmuc-WL^2P^2 trimer group, all NP groups showed lower EC_{50} titers except for the E2p-L4P NP group at w2, which yielded a modest P value of 0.0381 (**Fig. 5B**, bottom). This finding was somewhat unexpected, as significant differences were found between soluble E2 core and NP groups at both w2 and w5 in a recent HCV vaccine study (*65*), suggesting that antibody titers of antigen-presenting NPs may be influenced by antigen size, structure, and epitope distribution. NP display may occlude antibody access to the base and stalk epitopes, which are the targets of many bNAbs (*9*). This result may also be attributed to other factors such as dosage, as noted in our recent study (*65*). As the NP carrier accounts for 21-33% of the total mass of an NP vaccine and the same

dose (50 μg protein) has been used for all vaccine groups except for the I3-01v9-L7P NP group, mice in the NP groups would receive much less GP antigen than mice in the trimer only group.

We then validated the ebolavirus pseudoparticle (ebolavirus-pp) neutralization assay (*12*) using a panel of 10 antibodies against EBOV-Makona (**Fig. 5C**) and a BDBV strain (**Fig. 5D**) in 293 T cells. As expected, early EBOV NAbs KZ52 (*76*), c2G4, and c4G7 (*10*) neutralized EBOV but not BDBV. NAbs mAb100 and mAb114 (*12*) neutralized both ebolavirus species with different potencies. Four bNAbs (*9*), three directed to IFL and one targeting HR2-MPER, cross-neutralized EBOV and BDBV. A non-NAb, c13C6, which is part of a therapeutic antibody cocktail (*10*) and binds the glycan cap (*45*), appeared to enhance pseudoviral infection. The ebolavirus-pp assay was also performed in TZM-bl cells (**fig. S7D**), which were used to screen small-molecule inhibitors (*72*). While all the tested NAbs/bNAbs blocked pseudovirus infection, c13C6 exhibited a similar pattern of enhancement. When tested against pseudoparticles bearing the murine leukemia virus (MLV) Env, MLV-pps, c13C6 increased the MLV-pp infection while NAbs and bNAbs remained non-reactive (**fig. S7E**). Given what appeared to be a consistent pattern for c13C6 in pseudovirus assays, similar non-NAb responses in the analysis of animal samples hereafter would be referred to as “c13C6-like”. We next assessed the immunized mouse samples against EBOV (**Fig. 5E**) and BDBV (**Fig. 5F**) in the ebolavirus-pp assay. Immunoglobulin G (IgG) was purified from the mouse serum at the last time point (w11) to eliminate non-specific, anti-viral activities (*55, 65*). Distinct patterns of antibody response were observed, suggesting the elicitation of NAbs and c13C6-like non-NAbs. Among the three trimer groups, while GP_{ECTO} showed a moderate NAb response with signs of enhancement observed for 2-4 mice, an increase in both NAb and c13C6-like responses was noted for GPΔmuc, suggesting that the removal of MLD exposes both NAb epitopes and the glycan cap, which is a main target for ADE-causing antibodies in human infection (*25*). The WL^2P^2

mutation appeared to have largely reversed the adverse effect caused by the MLD removal. Among the three NPs, E2p-L4P was the best performer and elicited primarily NAb responses. However, a c13C6-like non-NAb response was observed for 2 mice in the FR group and for all mice in the I3-01v9-L7P group. Since only c13C6, but not any of the NAbs and bNAbs, reacted with MLV-pps (**fig. S7E**), we utilized the MLV-pp assay to gauge c13C6-like responses induced by different immunogens (**fig. S7F**). Indeed, the patterns of enhanced MLV-pp infection matched perfectly with the c13C6-like non-NAb responses seen in the ebolavirus-pp assays (**Figs. 5E** and **5F**). In the MLV-pp assay, E2p-L4P NP induced a minimum c13C6-like response comparable to GP_{ECTO}, in which MLD shields GP epitopes from antibody recognition. Our results also suggest that the high level of c13C6-like non-NAb response observed for the GPΔmuc and I3-01v9-L7P groups may be associated with the presence of open trimers and unassembled GP-NP species, respectively.

The mouse data offered useful insights into the effect of various GP forms and NP carriers on vaccine-induced antibody response. In brief, the benefit of NP display may not be fully reflected by binding antibody titers and should be judged by the type of antibodies elicited. The c13C6-like non-NAbs that target the glycan cap and cross-react with small secreted GP (ssGP) (*45*) need to be minimized during vaccination. A multilayered E2p NP with 20 GPΔmuc trimers on the surface elicited a robust NAb response, thus providing a promising vaccine candidate.

Immunogenicity of EBOV GP trimers and NPs in rabbits

Two GPΔmuc trimers, wildtype and WL^2P^2, and three NPs presenting the WL^2P^2 trimer were also assessed in rabbits with four injections over three-week intervals (**Fig. 6A**). Rabbit sera collected at six timepoints during immunization were analyzed by ELISA using the same trimer probe (**Fig. 6B** and **fig. S8, A** and **B**). Of note, rabbits were immunized with 20μg of mAb100/SEC-purified

I3-01v9-L7P NP to reduce c13C6-like responses. Between the two GPΔmuc trimer groups, WL^2P^2 showed higher EC_{50} titers for all time points except for w11, with a P value of 0.0229 obtained for w5 (two weeks after the second injection). Among the three NP groups, a consistent pattern was observed, with the I3-01v9 group showing the highest EC_{50} tier and the FR group the lowest throughout the immunization. A significant difference was found between the I3-01v9-L7P group and the E2p-L4P group for w8, w11, and w13 (four weeks after the last injection), with P values of 0.0021-0.0053. Compared to the GPΔmuc-WL^2P^2 trimer group, the I3-01v9-L7P NP group showed higher EC_{50} tiers for all six time points, with significant P values obtained for w8, w11, and w13. In contrast, the FR and E2p-L4P groups yielded lower EC_{50} titers than their respective trimer group at w2 and w5, but this pattern was reversed at w8 and w11 with modest P values (0.0421 and 0.0492 for FR and E2p, respectively) at w8. However, the advantage of these two NP groups diminished at w11, showing lower EC_{50} tiers than the trimer group at the last time point, w13. Purified IgGs from time points Pre, w2, w5, w8, and w11 were analyzed in ebolavirus-pp and MLV-pp assays (**Fig. 6C** and **fig. S8, C** to **F**). At the last time point, all vaccine groups showed NAb responses with no sign of enhanced pseudovirus infection (**Fig. 6C**), suggesting a different pattern compared to the mixed NAb/c13C6-like responses in mice (**Fig. 5**). Of note, the I3-01v9-L7P NP group yielded higher average IC_{50} (50% inhibitory concentration) titers, at 211.3 μg/ml and 11.72 μg/ml for EBOV and BDBV, respectively, than other groups, supporting the notion that the unassembled GP-NP species, not the I3-01v9 NP, were the cause of c13C6-like responses in mice. Consistently, all vaccine groups at w11 showed no enhancement of MLV-pp infection (**Fig. 6D**). Thus, c13C6-like non-NAbs appeared to be absent in serum toward the end of immunization. Interestingly, rabbit IgGs from the earlier time points demonstrated an increasing NAb response accompanied with a declining c13C6-like non-NAb response (**fig. S8, C** to **F**). In neutralization

assays against EBOV-Makona, enhanced ebolavirus-pp infection was observed for the two trimer groups, the FR group, and the two multilayered NP groups at w2, w5, and w8, and then disappeared at w5, w8, and w11, respectively. The results suggest that vaccine-induced c13C6-like antibodies in rabbits might shift epitopes and gain neutralizing activity through gene conversion, a mechanism employed by the rabbit immune system to rapidly develop functional antibodies (*87*).

B cell response profiles associated with EBOV GP trimers and NPs

Previously, we combined antigen-specific B cell sorting and NGS to obtain a quantitative readout of B cell responses induced by HCV E2 core (E2mc3) and E2mc3-E2p NP (*65*). Diverse heavy-chain variable gene (V_H) usage, a higher degree of V_H mutations, and a broader range of heavy chain complementarity determining region 3 (HCDR3) length were observed for E2p, alluding to a common B cell mechanism for NP vaccines (*65*). In this study, we applied the same strategy to obtain GP-specific B cell profiles for different EBOV vaccines (**Fig. 6E**). We first created an Avi-tagged GPΔmuc-WL^{2}P^2-1TD0 trimer probe to sort GP-specific mouse splenic B cells (**fig. S9A**). Sorted B cells from 25 mice (**fig. S9B**), five per group, were subjected to NGS on Ion GeneStudio S5. The NGS data was analyzed by a mouse Antibodyomics pipeline (*88*) (**fig. S9C**). Detailed B cell profiles were derived to facilitate comparison of different vaccine platforms (**Fig. 6F** and **fig. S9**, **D** to **F**). We mainly focused on the GPΔmuc-WL^{2}P^2-foldon group and the multilayered E2p group to compare B cell responses to GPΔmuc in the trimeric versus NP forms (**Fig. 6F**). In terms of germline gene usage, similar patterns were observed for V_H and V_K genes (**Fig. 6F**, panels 1 and 2). Namely, the redesigned GPΔmuc trimer activated more V_H/V_L genes (9.4/9.4) than its NP form (6/7), with P values of 0.0163 and 0.0076 for V_H and V_L, respectively. In contrast, the E2p NP decorated with 60 HCV E2 cores activated more V_H, but not V_L, genes than the E2 core (*65*). In terms of degree of somatic hypermutation (SHM), no significant difference was found between

the two groups (**Fig. 6F**, panel 3). However, we did observe a visible shift in the SHM distribution for the NP group, which showed higher germline V_H/V_K divergence, on average 6.4%/2.9%, than the trimer group, on average 5.3%/2.6%. In the HCDR3 analysis, two metrics – the average loop length and the RMS fluctuation (RMSF) of loop length – were calculated (**Fig. 6F**, panel 4). Unlike in the HCV study where the RMSF of HCDR3 length yielded a P value of <0.0001 between the E2 core and E2p NP groups (*65*), no significant difference was found between the EBOV GPΔmuc and E2p NP groups. Overall, EBOV and HCV NPs exhibited rather different B cell patterns with respect to their individual antigens. In addition, there were no apparent correlations between B cell profiles and vaccine-induced NAb or c13C6-like response. Our results thus suggest that antigen size, structure, glycosylation, and epitope distribution, other than the NP platform, may contribute critically to shaping the NP vaccine-induced B cell response.

DISCUSSION

With a mortality rate of up to 90%, EBOV has caused significant humanitarian crises, calling for action across sectors to develop effective interventions (*3*). ZMapp (*10, 11*) established the use of NAbs as treatment for patients with Ebola virus disease (EVD) and propelled a community-wide campaign to identify novel NAbs and bNAbs (*8, 9, 30, 48*). In addition, several vaccine candidates have advanced to human trials (*63, 89*). The rVSV-ZEBOV vaccine demonstrated an efficacy of 100% in an open-label, cluster-randomized ring trial (*16*). In a phase 2 placebo-controlled trial of two vectored vaccines (including rVSV-ZEBOV), the antibody titer remained similar between the vaccine and placebo groups at one week post-vaccination and only started to peak after one month (*15*). Recent analysis of human B cell responses to EBOV infection has revealed hurdles in GP-specific NAb response (*28, 29*). NAbs from vaccinated humans showed low levels of SHM (*90*), suggesting a suboptimal B cell response elicited by an otherwise effective vectored vaccine (*91*).

The immune correlates of vaccine protection may not be universal and are likely determined by vaccine platforms in addition to other factors (*92*). As most EBOV vaccines are vector-based (*63, 89*), recombinant protein vaccines remain a promising approach to combat this deadly virus.

Here, we approached EBOV vaccine design with an antibody-based strategy focusing on GP metastability and multivalent display. Previously, we identified an $HR1_N$ bend as the cause of HIV-1 Env metastability (*55, 56*) and optimized an HCV E2 core (*65*). EBOV GP belongs to the class-I fusion protein family (*53, 54*) and is inherently metastable, as is HIV-1 Env. In this study, we probed the cause of EBOV GP metastability by testing various designs targeting the HR2 stalk, the $HR1_C$ bend, and the GP/GP interface (via inter-protomer disulfide bonds). Our results revealed a stabilizing effect of the W615L mutation and the stalk extension, in additional to an unexpected sensitivity of $HR1_C$ (equivalent to HIV-1 $HR1_N$) to specific proline mutations, which increased trimer yield at the cost of causing complex unfolding behaviors as indicated by DSC. Although this pattern was not reported in a recent study of an EBOV-Makona GPΔmuc trimer bearing the T577P mutation (*81*), it is possible that GP metastability may be strain-specific and thus warrants further investigation. Multivalent NP display proved to be a challenging task for EBOV GP due to its tendency for dissociation. Two-component NPs (*93, 94*) and the SpyTag/SpyCatcher ligation system (*95, 96*) have been used in the development of VLP-type vaccines. However, their inherent complexity in production, assembly, and purification, as well as their structural instability *in vivo* and off-target immune response may dampen their potential as human vaccines. Here, we proposed a single-component, multilayered, self-assembling protein NP design for E2p and I3-01 60-mers. Encoded within a single plasmid, such NP vaccines can be readily produced in GMP-compatible CHO cells followed by antigen-specific immunoaffinity purification and SEC, providing a simple and robust manufacturing process. However, immunogenicity studies in mice and rabbits revealed

critical factors that need to be addressed in EBOV vaccine development. The choice of GP_{ECTO} or GPΔmuc as a vaccine antigen may lead to antibody responses targeting different epitopes on GP. Antibody access to GP epitopes at the IFL, the base, and the HR2 stalk may differ in the trimeric and NP forms. In this study, we observed c13C6-like non-NAb responses in animal immunization, which appeared to be associated with open GPs. Single-cell antibody isolation, structural epitope mapping, and live ebolavirus assays may be required to determine the biological relevance of these c13C6-like antibodies induced by vaccination. Nonetheless, the E2p-L4P NP elicited a minimum c13C6-like response in mice, while the I3-01v9-L7P NP without any impurities induced the most effective NAb response in rabbits, providing two promising vaccine candidates.

Future investigation should be directed toward assessment of GPΔmuc-WL[2], which has the highest thermostability, and GPΔmuc-SS2, which is a disulfide-locked trimer, as well as their NPs, which would be expected to further reduce the c13C6-like non-NAb responses. Antibodies isolated from animals immunized with these newly designed EBOV trimers and NPs should provide critical insights into epitope recognition and guide future vaccine development.

MATERIALS AND METHODS

Design, expression and purification of EBOV GPΔmuc and GPΔmuc-presenting NPs

The glycoprotein sequence of Zaire EBOV (strain Mayinga-76) with a T42A substitution was used to design all GP constructs in this study (UniProt ID: Q05320). Wildtype and redesigned GPΔmuc constructs were transiently expressed in HEK293F cells (Thermo Fisher) for biochemical, biophysical, and antigenic analyses. Briefly, 293 F cells were thawed and incubated with FreeStyle™ 293 Expression Medium (Life Technologies, CA) in a shaker incubator at 37°C, 135 rpm and 8% CO_2. When the cells reached a density of 2.0×10^6/ml, expression medium was added

to reduce cell density to 1.0×10^6 ml^{-1} for transfection with polyethyleneimine (PEI) (Polysciences, Inc). Next, 900 μg of plasmid in 25 ml of Opti-MEM transfection medium (Life Technologies, CA) was mixed with 5 ml of PEI-MAX (1.0 mg/ml) in 25 ml of Opti-MEM. After 30-min incubation, the DNA-PEI-MAX complex was added to 1L 293 F cells. Culture supernatants were harvested five days after transfection, clarified by centrifugation at 2200 rpm for 22 min, and filtered using a 0.45 μm filter (Thermo Scientific). GPΔmuc proteins were extracted from the supernatants using an mAb114 antibody column or an mAb100 antibody column. Bound proteins were eluted three times, each with 5ml of 0.2 M Glycine (pH=2.2) and neutralized with 0.5 ml of Tris-Base (pH=9.0). The proteins were further purified by size exclusion chromatography (SEC) on a Superdex 200 Increase 10/300 GL column or a HiLoad Superdex 200 16/600 column (GE Healthcare). GPΔmuc-presenting nanoparticles were produced in ExpiCHO cells (Thermo Fisher). Briefly, ExpiCHO cells were thawed and incubated with ExpiCHO™ Expression Medium (Thermo Fisher) in a shaker incubator at 37 °C, 135 rpm and 8% CO_2. When the cells reached a density of 10×10^6 ml^{-1}, ExpiCHO™ Expression Medium was added to reduce cell density to 6×10^6 ml^{-1} for transfection. The ExpiFectamine™ CHO/plasmid DNA complexes were prepared for 100-ml transfection in ExpiCHO cells following the manufacturer's instructions. For these nanoparticle constructs, 100 μg of plasmid and 320 μl of ExpiFectamine™ CHO reagent were mixed in 7.7 ml of cold OptiPRO™ medium (Thermo Fisher). After the first feed on day one, ExpiCHO cells were cultured in a shaker incubator at 33 °C, 115 rpm and 8% CO_2 following the Max Titer protocol with an additional feed on day five (Thermo Fisher). Culture supernatants were harvested 13 to 14 days after transfection, clarified by centrifugation at 4000 rpm for 25 min, and filtered using a 0.45 μm filter (Thermo Fisher). The mAb100 antibody column was used to extract nanoparticles from the supernatants, which was followed by SEC on a Superose 6 10/300 GL column. For GPΔmuc

583 and GPΔmuc-presenting nanoparticles, protein concentration was determined using UV_{280}
584 absorbance with theoretical extinction coefficients.
585
586 **Blue native polyacrylamide gel electrophoresis**
587 EBOV GPΔmuc and GPΔmuc-presenting NPs were analyzed by blue native polyacrylamide gel
588 electrophoresis (BN-PAGE) and stained with Coomassie blue. The proteins were mixed with
589 sample buffer and G250 loading dye and added to a 4-12% Bis-Tris NativePAGE™ gel (Life
590 Technologies). BN-PAGE gels were run for 2 to 2.5 hours at 150 V using the NativePAGE™
591 running buffer (Life Technologies) according to the manufacturer's instructions.
592
593 **Enzyme-linked immunosorbent assay**
594 Each well of a Costar™ 96-well assay plate (Corning) was first coated with 50 µl PBS containing
595 0.2 µg of the appropriate antigens. The plates were incubated overnight at 4 °C, and then washed
596 five times with wash buffer containing PBS and 0.05% (v/v) Tween 20. Each well was then coated
597 with 150 µl of a blocking buffer consisting of PBS, 40 mg ml^{-1} blotting-grade blocker (Bio-Rad),
598 and 5% (v/v) FBS. The plates were incubated with the blocking buffer for 1 hour at room
599 temperature, and then washed five times with wash buffer. For antigen binding, antibodies were
600 diluted in the blocking buffer to a maximum concentration of 10 µg ml^{-1} followed by a 10-fold
601 dilution series. For each antibody dilution, a total of 50 µl volume was added to the appropriate
602 wells. For animal sample analysis, serum or plasma was diluted by 10-fold for mouse and 50-fold
603 for rabbit in the blocking buffer and subjected to a 10-fold dilution series. For each sample dilution,
604 a total of 50 µl volume was added to the wells. Each plate was incubated for 1 hour at room
605 temperature, and then washed 5 times with PBS containing 0.05% Tween 20. For antibody

binding, a 1:5000 dilution of goat anti-human IgG antibody (Jackson ImmunoResearch Laboratories, Inc), or for animal sample analysis, a 1:2000 dilution of horseradish peroxidase (HRP)-labeled goat anti-mouse or anti-rabbit IgG antibody (Jackson ImmunoResearch Laboratories), was then made in the wash buffer (PBS containing 0.05% Tween 20), with 50 μl of this diluted secondary antibody added to each well. The plates were incubated with the secondary antibody for 1 hour at room temperature, and then washed 5 times with PBS containing 0.05% Tween 20. Finally, the wells were developed with 50 μl of TMB (Life Sciences) for 3-5 min before stopping the reaction with 50 μl of 2 N sulfuric acid. The resulting plate readouts were measured at a wavelength of 450 nm. Of note, the week 2 serum binding did not reach the plateau (or saturation) to allow for accurate determination of EC_{50} titers. Nonetheless, the EC_{50} values calculated in Prism were used as a quantitative measure of antibody titers to facilitate the comparison of different vaccine groups at week 2.

Bio-layer interferometry

The kinetics of GPΔmuc and GPΔmuc-presenting nanoparticle binding to a panel of 10 antibodies was measured using an Octet RED96 instrument (FortéBio, Pall Life Sciences). All assays were performed with agitation set to 1000 rpm in FortéBio 1× kinetic buffer. The final volume for all the solutions was 200 μl per well. Assays were performed at 30 °C in solid black 96-well plates (Geiger Bio-One). 5 μg ml^{-1} of antibody in 1× kinetic buffer was loaded onto the surface of anti-human Fc Capture Biosensors (AHC) for GPΔmuc and of anti-human Fc Quantitation Biosensors (AHQ) for nanoparticles for 300 s. A 60 s biosensor baseline step was applied prior to the analysis of the association of the antibody on the biosensor to the antigen in solution for 200 s. A two-fold concentration gradient of antigen, starting at 400 nM for GPΔmuc trimers, 25 nM for FR NP, and

10 for E2p/I3-01v9 NPs was used in a titration series of six. The dissociation of the interaction was followed for 300 s. Correction of baseline drift was performed by subtracting the mean value of shifts recorded for a sensor loaded with antibody but not incubated with antigen and for a sensor without antibody but incubated with antigen. Octet data were processed by FortéBio's data acquisition software v.8.1. Experimental data were fitted with the binding equations describing a 2:1 interaction to achieve optimal fitting. Of note, GPΔmuc trimer binding was also measured using AHQ to facilitate the comparison of antibody binding with nanoparticles.

Differential scanning calorimetry

Thermal melting curves of WT and redesigned GPΔmuc trimers were obtained with a MicroCal VP-Capillary calorimeter (Malvern). The purified GPΔmuc produced from 293F cells were buffer exchanged into 1×PBS and concentrated to 27–50 μM before analysis by the instrument. Melting was probed at a scan rate of 90 °C·h^{-1} from 25 °C to 110 °C. Data processing, including buffer correction, normalization, and baseline subtraction, was conducted using the standardized protocol from the Origin 7.0 software.

Protein production, crystallization and data collection

Two *Zaire* EBOV GPΔmuc-foldon constructs, one with the W615L mutation and the L extension (to aa 637) and the other with an additional T577P mutation, were expressed in HEK293S cells. The expressed GP was purified using an mAB100 antibody column followed by size-exclusion chromatography (SEC) on a HiLoad Superdex 200 16/600 column (GE Healthcare). The freshly purified samples of GP were used for crystallization. The crystallization experiments were carried out using the sitting drop vapor diffusion method on our automated CrystalMation™ robotic system (Rigaku) at both 4 °C and 20 °C at The Scripps Research Institute (TSRI) (*97*). EBOV GP

was concentrated to ~10 mg/ml in 50 mM Tris-HCl pH 8.0. The reservoir solution contained 12% (w/v) PEG 6000 and 0.1 M sodium citrate, pH 4.5. Diffraction-quality crystals were obtained after two weeks at 20 °C. The EBOV GP crystals were cryoprotected with 25% glycerol, mounted in a nylon loop and flash cooled in liquid nitrogen. Diffraction data were collected for crystals of GPΔmuc-WL^2-foldon and GPΔmuc-WL^2P^2-foldon at Advanced Photon Source (APS) beamline 23ID-D and Stanford Synchrotron Radiation Light source (SSRL) beamline 12-2, at 2.3 Å and 3.2 Å resolution, respectively. The diffraction data sets were processed with HKL-2000 (*98*). The crystal data were indexed in rhombohedral R32 and tetragonal P321 space groups with cell dimensions of GPΔmuc-WL^2-foldon $a = b = 114.58$ Å and $c = 312.38$ Å and GPΔmuc-WL^2P^2-foldon $a = b = 114.06$ Å and $c = 136.22$ Å, respectively (**table S1**). The overall completeness of the two data sets was 96.4% and 99.9%, respectively.

Structure determination and refinement

The structures of EBOV GP were determined by molecular replacement (MR) using Phaser (*99*) from the CCP4i suite (*100*) with the coordinates of *Zaire* Ebola GP (PDB: 5JQ3) and the program MOLREP (*101*). The polypeptide chains were manually adjusted into electron density using Coot (*102*), refined with Refmac 5.5 (*103*) and validated using MolProbity (*104*). The final R_{cryst} and R_{free} values for the refined structures are 19.6% and 22.9% and 28.6% and 33.6% for GPΔmuc-WL^2-foldon and GPΔmuc-WL^2P^2-foldon, respectively. The data processing and refinement parameters are listed in **table S1**.

Electron microscopy (EM) assessment of nanoparticle constructs

The initial EM analysis of EBOV GPΔMuc nanoparticles was conducted at the Core Microscopy Facility at The Scripps Research Institute. Briefly, nanoparticle samples were prepared at the concentration of 0.01 mg/ml. Carbon-coated copper grids (400 mesh) were glow-discharged and 8 µL of each sample was adsorbed for 2 min. Excess sample was wicked away and grids were negatively stained with 2% uranyl formate for 2 min. Excess stain was wicked away and the grids were allowed to dry. Samples were analyzed at 80 kV with a Talos L120C transmission electron microscope (Thermo Fisher) and images were acquired with a CETA 16M CMOS camera.

Animal immunization and sample collection

Similar immunization protocols have been reported in our previous NP vaccine studies (*55, 65*). Briefly, the Institutional Animal Care and Use Committee (IACUC) guidelines were followed with animal subjects tested in the immunization study. Eight-week-old BALB/c mice were purchased from The Jackson Laboratory and housed in ventilated cages in environmentally controlled rooms at The Scripps Research Institute, in compliance with an approved IACUC protocol and AAALAC (Association for Assessment and Accreditation of Laboratory Animal Care) International guidelines. Mice were immunized at weeks 0, 3, 6, and 9 with 200 µl of antigen/adjuvant mix containing 50 µg of vaccine antigen and 100 µl of adjuvant, AddaVax or Adju-Phos (InvivoGen), via the intraperitoneal (i.p.) route. Of note, 20 µg instead of 50 µg of mAb100-purified I3-01v9 protein was used in mouse immunization due to its low yield. Blood was collected two weeks after each immunization. All bleeds were performed through the retro-orbital sinus using heparinized capillary tubes into EDTA-coated tubes. Samples were diluted with an equal volume of PBS and then overlaid on 4.5 ml of Ficoll in a 15 ml SepMate™ tube (STEMCELL Technologies) and spun at 1200 RPM for 10 min at 20 °C to separate plasma and cells. The plasma was heat inactivated at

56 °C for 30 min, spun at 1200 RPM for 10 min, and sterile filtered. The cells were washed once in PBS and then resuspended in 1 ml of ACK Red Blood Cell lysis buffer (Lonza). After washing with PBS, peripheral blood mononuclear cells (PBMCs) were resuspended in 2 ml of Bambanker Freezing Media (Lymphotec). Spleens were also harvested and ground against a 70-μm cell strainer (BD Falcon) to release the splenocytes into a cell suspension. Splenocytes were centrifuged, washed in PBS, treated with 5 ml of ACK lysing buffer (Lonza), and frozen with 3ml of Bambanker freezing media. Purified mouse IgGs at week 11 (w11) were obtained using a 0.2-ml protein G spin kit (Thermo Scientific) following the manufacturer's instructions and assessed in pseudovirus neutralization assays. Rabbit immunization and blood sampling were carried out under a subcontract at ProSci (San Diego, CA). Five groups of female New Zealand White rabbits, four rabbits per group, were immunized intramuscularly (i.m.) with 50 μg of vaccine antigen formulated in 250 μl of adjuvant, AddaVax or Adju-Phos (InvivoGen), with a total volume of 500 μl, at weeks 0, 3, 6, and 9. Of note, 20 μg of mAb100/SEC-purified I3-01v9 NP was used in the rabbit immunization. Blood samples, 20 ml each time, were collected from the auricular artery at day 0 (Pre), weeks 2, 5, 8, and 11. For week 13, more than 100 ml of blood was taken via cardiac puncture for PBMC isolation. Plasma and serum samples were heat inactivated for ELISA binding assays, while purified rabbit IgGs were assessed in pseudovirus neutralization assays.

Pseudovirus neutralization assay

Ebolavirus pseudoviral particle (ebolavirus-pp) neutralization assays were utilized to assess the neutralizing activity of previously reported mAbs and vaccine-induced antibody responses in mice and rabbits. Ebolavirus-pps were generated by co-transfection of HEK293T cells with the HIV-1 pNL4-3.lucR-E- plasmid (the NIH AIDS reagent program: https://www.aidsreagent.org/) and the expression plasmid encoding the GP gene of an EBOV Makona strain (GenBank Accession

number: KJ660346) or a BDBV Uganda strain (GenBank Accession number: KR063673) at a 4:1 ratio by lipofectamine 3000 (Thermo Fisher Scientific). After 48 to 72 h, ebolavirus-pps were collected from the supernatant by centrifugation at 4000 rpm for 10 min, aliquoted, and stored at -80 °C before use. The mAbs at a starting concentration of 10 μg/ml, or purified IgGs at a starting concentration 300 μg/ml for mouse and 1000 μg/ml for rabbit, were mixed with the supernatant containing ebolavirus-pps and incubated for 1 hour at 37°C in white solid-bottom 96-well plate (Corning). Based on recent studies on EBOV infectivity in various cell lines (*72, 105*), HEK293T cells or TZM-bl cells were used for ebolavirus-pp neutralization assays. Briefly, HEK293T cells or TZM-bl cells at 1×10^4 were added to each well and the plate was incubated at 37°C for 48 h. After incubation, overlying media was removed, and cells were lysed. The firefly luciferase signal from infected cells was determined using the Bright-Glo Luciferase Assay System (Promega) according to the manufacturer's instructions. Data were retrieved from a BioTek microplate reader with Gen 5 software, the average background luminescence from a series of uninfected wells was subtracted from each well, and neutralization curves were generated using GraphPad Prism 8.4.3, in which values from wells were compared against a well containing ebolavirus-pp only. The same HIV-1 vectors pseudotyped with the murine leukemia virus (MLV) Env gene, termed MLV-pps, were produced in HEK293T cells and included in the neutralization assays as a negative control. As non-NAb c13C6 exhibited enhanced MLV-pp infection, the MLV-pp assay was also used to detect the c13C6-like, ADE-causing antibody response in immunized animal samples.

Bulk sorting of EBOV GPΔmuc-specific mouse B cells

Spleens were harvested from immunized mice 15 days after the last immunization and cell suspension was prepared. Cells were stained as follows: dead cells were excluded by staining with

Fixable Aqua Dead Cell Stain kit (Thermo Fisher L34957). Receptors FcγIII (CD16) and FcγII (CD32) were blocked by adding 20 µl of 2.4G2 mAb (BD Pharmigen N553142). Cells were then incubated with 10 µg/ml of biotinylated GPΔmuc, WT or UFOg^2. Briefly, GPΔmuc was generated by biotinylation of the individual Avi-tagged EBOV GPΔmuc using biotin ligase BirA according to the manufacturer's instructions (Avidity LLC). Biotin excess was removed by SEC on a HiLoad Superdex 200 16/600 column (GE Healthcare). In the SEC profile, the Avi-tagged GPΔmuc peak is centered at 14.5 ml, while a broader peak of biotin ligase can be found at 65-70 ml (WT) or 60-65 ml (UFOg^2). Cells and biotinylated proteins were incubated for 5 min at 4 °C, followed by the addition of 2.5 µl of anti-mouse IgG fluorescently labeled with FITC (Jackson ImmunoResearch 115-095-071) and incubated for 15 min at 4 °C. Finally, 5 µl of premium-grade allophycocyanin (APC)-labeled streptavidin were added to the cells and incubated for 15 min at 4 °C. In each step, cells were washed with DPBS and the sorting buffer was 0.5 ml FACS buffer. FITC$^+$ APC$^+$ GPΔmuc-specific B cells were sorted using MoFloAstrios into one well of a 96-well plate with 20µl of lysis buffer.

NGS and bioinformatics analysis of mouse B cells

A 5′-rapid amplification of cDNA ends (RACE) protocol has been reported for unbiased sequencing of mouse B cell repertoires. Here, this protocol was applied to bulk-sorted, E2-specific mouse splenic B cells. Briefly, 5´-RACE cDNA was obtained from bulk-sorted splenic B cells of each mouse with SMART-Seq v4 Ultra Low Input RNA Kit for Sequencing (TaKaRa). The immunoglobulin PCRs were set up with Platinum *Taq* High-Fidelity DNA Polymerase (Life Technologies) in a total volume of 50 µl, with 5 µl of cDNA as template, 1 µl of 5´-RACE primer, and 1 µl of 10 µM reverse primer. The 5′-RACE primer contained a PGM/S5 P1 adaptor, while the reverse primer contained a PGM/S5 A adaptor. We adapted the mouse 3´-C_γ1-3/3´-C_μ inner

primers and 3´-mC_κ outer primer as reverse primers for 5´-RACE PCR processing of heavy and light (κ) chains. A total of 25 cycles of PCR was performed and the expected PCR products (500-600 bp) were gel purified (Qiagen). NGS was performed on the Ion S5 GeneStudio system. Briefly, heavy and light (κ) chain libraries from the same mouse were quantitated using Qubit® 2.0 Fluorometer with Qubit® dsDNA HS Assay Kit, and then mixed using a ratio of 3:1 before being pooled with antibody libraries of other mice at an equal ratio for sequencing. Template preparation and (Ion 530) chip loading were performed on Ion Chef using the Ion 520/530 Ext Kit, followed by sequencing on the Ion S5 system with default settings. The mouse *Antibodyomics* pipeline was used to process the raw data and determine distributions for germline gene usage, somatic hypermutation (SHM), germline divergence, and H/KCDR3 loop length.

SUPPLEMENTARY MATERIALS

Supplementary material for this article is available at http://advances.sciencemag.org/cgi/content/full/x/xx/xxx.

fig. S1. Design, screening, and antigenic characterization of EBOV GPΔmuc trimers with modified stalk and $HR1_C$.

fig. S2. Design and characterization of EBOV GPΔMuc trimers with inter-protomer disulfide bonds.

fig. S3. A 2.3 Å-resolution structure of GPΔmuc-W615L-L-foldon, or GPΔmuc-WL^2-foldon.

fig. S4. Structural comparison of Mayinga GPΔmuc-WL^2-foldon and Makona GPΔmuc with the T577P/R588E mutation (PDB: 6VKM).

fig. S5. Structural analysis of known GP/antibody complexes.

fig. S6. Design and characterization of multilayered EBOV GPΔmuc-presenting NPs.

fig. S7. Immunogenicity assessment of EBOV GP/GPΔmuc trimers and GPΔmuc-presenting NPs in BALB/c mice.

fig. S8. Immunogenicity assessment of EBOV GP/GPΔmuc trimers and GPΔmuc-presenting NPs in rabbits.

fig. S9. Unbiased NGS repertoire analysis of bulk-sorted Ebola GP-specific mouse splenic B cells.

Table S1. X-ray crystallographic data collection and refinement statistics.

REFERENCES

1. J. H. Kuhn *et al.*, Virus nomenclature below the species level: a standardized nomenclature for filovirus strains and variants rescued from cDNA. *Arch. Virol.* **159**, 1229-1237 (2014).
2. S. Paessler, D. H. Walker, Pathogenesis of the Viral Hemorrhagic Fevers. *Annu. Rev. Pathol.* **8**, 411-440 (2013).
3. D. Malvy, A. K. McElroy, H. de Clerck, S. Gunther, J. van Griensven, Ebola virus disease. *Lancet* **393**, 936-948 (2019).
4. Ebola outbreak 2014-2016 (https://www.who.int/csr/disease/ebola/en/).
5. Ebola situation reports: Democratic Republic of the Congo (https://www.who.int/ebola/situation-reports/drc-2018/en/).
6. A. P. Cardile, L. G. Downey, P. D. Wiseman, T. K. Warren, S. Bavari, Antiviral therapeutics for the treatment of Ebola virus infection. *Curr. Opin. Pharmacol.* **30**, 138-143 (2016).
7. A. P. Cardile, T. K. Warren, K. A. Martins, R. B. Reisler, S. Bavari, Will There Be a Cure for Ebola? *Annu. Rev. Pharmacol. Toxicol.* **57**, 329-348 (2017).
8. C. E. Mire, T. W. Geisbert, Neutralizing the threat: pan-ebolavirus antibodies close the loop. *Trends Mol. Med.* **23**, 669-671 (2017).
9. L. B. King, J. C. Milligan, B. R. West, S. L. Schendel, E. O. Saphire, Achieving cross-reactivity with pan-ebolavirus antibodies. *Curr. Opin. Virol.* **34**, 140-148 (2019).
10. X. G. Qiu *et al.*, Reversion of advanced Ebola virus disease in nonhuman primates with ZMapp. *Nature* **514**, 47-53 (2014).
11. R. T. Davey *et al.*, A randomized, controlled trial of ZMapp for Ebola virus infection. *N. Engl. J. Med.* **375**, 1448-1456 (2016).
12. D. Corti *et al.*, Protective monotherapy against lethal Ebola virus infection by a potently neutralizing antibody. *Science* **351**, 1339-1342 (2016).
13. M. R. Gaudinski *et al.*, Safety, tolerability, pharmacokinetics, and immunogenicity of the therapeutic monoclonal antibody mAb114 targeting Ebola virus glycoprotein (VRC 608): an open-label phase 1 study. *Lancet* **393**, 889-898 (2019).
14. F. C. Zhu *et al.*, Safety and immunogenicity of a recombinant adenovirus type-5 vector-based Ebola vaccine in healthy adults in Sierra Leone: a single-centre, randomised, double-blind, placebo-controlled, phase 2 trial. *Lancet* **389**, 621-628 (2017).

15. S. B. Kennedy *et al.*, Phase 2 placebo-controlled trial of two vaccines to prevent Ebola in liberia. *N. Engl. J. Med.* **377**, 1438-1447 (2017).
16. A. M. Henao-Restrepo *et al.*, Efficacy and effectiveness of an rVSV-vectored vaccine in preventing Ebola virus disease: final results from the Guinea ring vaccination, open-label, cluster-randomised trial (Ebola Ca Suffit!). *Lancet* **389**, 505-518 (2017).
17. U. N. Sarwar *et al.*, Safety and immunogenicity of DNA vaccines encoding ebolavirus and marburgvirus wild-type glycoproteins in a phase I clinical trial. *J. Infect. Dis.* **211**, 549-557 (2015).
18. S. M. Jones *et al.*, Live attenuated recombinant vaccine protects nonhuman primates against Ebola and Marburg viruses. *Nat. Med.* **11**, 786-790 (2005).
19. X. G. Qiu *et al.*, Mucosal immunization of cynomolgus macaques with the VSV delta G/ZEBOVGP vaccine stimulates strong Ebola GP-specific immune responses. *PLoS One* **4**, e5547 (2009).
20. T. W. Geisbert *et al.*, Single-injection vaccine protects nonhuman primates against infection with Marburg virus and three species of Ebola virus. *J. Virol.* **83**, 7296-7304 (2009).
21. T. W. Geisbert *et al.*, Vesicular stomatitis virus-based Ebola vaccine is well-tolerated and protects immunocompromised nonhuman primates. *PLoS Pathog.* **4**, e1000225 (2008).
22. Y. Lévy *et al.*, Prevention of Ebola virus disease through vaccination: where we are in 2018. *Lancet* **392**, 787-790 (2018).
23. A. Marzi *et al.*, Antibodies are necessary for rVSV/ZEBOV-GP-mediated protection against lethal Ebola virus challenge in nonhuman primates. *Proc. Natl. Acad. Sci. U. S. A.* **110**, 1893-1898 (2013).
24. I. L. McWilliams *et al.*, Pseudovirus rVSV delta G-ZEBOV-GP infects neurons in retina and CNS, causing apoptosis and neurodegeneration in neonatal mice. *Cell Rep.* **26**, 1718-1726.e1714 (2019).
25. N. A. Kuzmina *et al.*, Antibody-dependent enhancement of Ebola virus infection by human antibodies isolated from survivors. *Cell Rep.* **24**, 1802-1815.e1805 (2018).
26. J. E. Lee, E. O. Saphire, Ebolavirus glycoprotein structure and mechanism of entry. *Future Virol.* **4**, 621-635 (2009).
27. A. K. McElroy *et al.*, Human Ebola virus infection results in substantial immune activation. *Proc. Natl. Acad. Sci. U. S. A.* **112**, 4719-4724 (2015).
28. C. W. Davis *et al.*, Longitudinal analysis of the human B cell response to Ebola virus infection. *Cell* **177**, 1566-1582.e1517 (2019).
29. L. E. Williamson *et al.*, Early human B cell response to Ebola virus in four US survivors of infection. *J. Virol.* **93**, e01439-01418 (2019).
30. E. O. Saphire, M. J. Aman, Feverish quest for Ebola immunotherapy: straight or cocktail? *Trends Microbiol.* **24**, 684-686 (2016).
31. A. I. Flyak *et al.*, Mechanism of human antibody-mediated neutralization of Marburg virus. *Cell* **160**, 893-903 (2015).
32. L. B. King *et al.*, The marburgvirus-neutralizing human monoclonal antibody MR191 targets a conserved site to block virus receptor binding. *Cell Host Microbe* **23**, 101-109.e104 (2018).
33. M. L. Fusco *et al.*, Protective mAbs and cross-reactive mAbs raised by immunization with engineered Marburg virus GPs. *PLoS Pathog.* **11**, e1005016 (2015).

34. Z. Y. Keck *et al.*, Macaque monoclonal antibodies targeting novel conserved epitopes within filovirus glycoprotein. *J. Virol.* **90**, 279-291 (2016).
35. K. A. Howell *et al.*, Antibody treatment of Ebola and Sudan virus infection via a uniquely exposed epitope within the glycoprotein receptor-binding site. *Cell Rep.* **15**, 1514-1526 (2016).
36. X. L. Zhao *et al.*, Immunization-elicited broadly protective antibody reveals ebolavirus fusion loop as a site of vulnerability. *Cell* **169**, 891-904.e815 (2017).
37. Z. A. Bornholdt *et al.*, Isolation of potent neutralizing antibodies from a survivor of the 2014 Ebola virus outbreak. *Science* **351**, 1078-1083 (2016).
38. A. Z. Wec *et al.*, Antibodies from a human survivor define sites of vulnerability for broad protection against ebolaviruses. *Cell* **169**, 878–890 (2017).
39. P. Gilchuk *et al.*, Multifunctional pan-ebolavirus antibody recognizes a site of broad vulnerability on the ebolavirus glycoprotein. *Immunity* **49**, 363-374.e310 (2018).
40. J. E. Lee *et al.*, Structure of the Ebola virus glycoprotein bound to an antibody from a human survivor. *Nature* **454**, 177-182 (2008).
41. J. M. Dias *et al.*, A shared structural solution for neutralizing ebolaviruses. *Nat. Struct. Mol. Biol.* **18**, 1424-1427 (2011).
42. J. Misasi *et al.*, Structural and molecular basis for Ebola virus neutralization by protective human antibodies. *Science* **351**, 1343-1346 (2016).
43. Z. A. Bornholdt *et al.*, Host-primed Ebola virus GP exposes a hydrophobic NPC1 receptor-binding pocket, revealing a target for broadly neutralizing antibodies. *Mbio* **7**, (2016).
44. C. D. Murin *et al.*, Structures of protective antibodies reveal sites of vulnerability on Ebola virus. *Proc. Natl. Acad. Sci. U. S. A.* **111**, 17182-17187 (2014).
45. J. Pallesen *et al.*, Structures of Ebola virus GP and sGP in complex with therapeutic antibodies. *Nat. Microbiol.* **1**, 16128 (2016).
46. A. I. Flyak *et al.*, Cross-reactive and potent neutralizing antibody responses in human survivors of natural ebolavirus infection. *Cell* **164**, 392-405 (2016).
47. P. Gilchuk *et al.*, Analysis of a therapeutic antibody cocktail reveals determinants for cooperative and broad ebolavirus neutralization. *Immunity* **52**, 388-403.e312 (2020).
48. E. O. Saphire *et al.*, Systematic analysis of monoclonal antibodies against Ebola virus GP defines features that contribute to protection. *Cell* **174**, 938–952.e913 (2018).
49. L. M. Walker, D. R. Burton, Rational antibody-based HIV-1 vaccine design: current approaches and future directions. *Curr. Opin. Immunol.* **22**, 358-366 (2010).
50. B. F. Haynes, J. R. Mascola, The quest for an antibody-based HIV vaccine. *Immunol. Rev.* **275**, 5-10 (2017).
51. R. W. Sanders, J. P. Moore, Native-like Env trimers as a platform for HIV-1 vaccine design. *Immunol Rev* **275**, 161-182 (2017).
52. A. B. Ward, I. A. Wilson, The HIV-1 envelope glycoprotein structure: nailing down a moving target. *Immunol Rev* **275**, 21-32 (2017).
53. J. M. White, S. E. Delos, M. Brecher, K. Schornberg, Structures and mechanisms of viral membrane fusion proteins: Multiple variations on a common theme. *Crit. Rev. Biochem. Mol. Biol.* **43**, 189-219 (2008).
54. S. C. Harrison, Viral membrane fusion. *Virology* **479**, 498-507 (2015).
55. L. He *et al.*, HIV-1 vaccine design through minimizing envelope metastability. *Sci. Adv.* **4**, aau6769 (2018).

56. L. Kong *et al.*, Uncleaved prefusion-optimized gp140 trimers derived from analysis of HIV-1 envelope metastability. *Nat. Commun.* **7**, 12040 (2016).
57. Y. Aldon *et al.*, Rational design of DNA-expressed stabilized native-like HIV-1 envelope trimers. *Cell Rep.* **24**, 3324-3338.e3325 (2018).
58. P. J. M. Brouwer, R. W. Sanders, Presentation of HIV-1 envelope glycoprotein trimers on diverse nanoparticle platforms. *Curr. Opin. HIV AIDS* **14**, 302-308 (2019).
59. D. W. Kulp, Z. Xu, Protein engineering and particulate display of B-cell epitopes to facilitate development of novel vaccines. *Curr. Opin. Immunol.* **59**, 49-56 (2019).
60. K. L. Warfield *et al.*, Ebola virus-like particle-based vaccine protects nonhuman primates against lethal Ebola virus challenge. *J. Infect. Dis.* **196**, S430-S437 (2007).
61. D. L. Swenson *et al.*, Virus-like particles exhibit potential as a pan-filovirus vaccine for both Ebola and Marburg viral infections. *Vaccine* **23**, 3033-3042 (2005).
62. K. L. Warfield *et al.*, Ebola virus-like particles protect from lethal Ebola virus infection. *Proc. Natl. Acad. Sci. U. S. A.* **100**, 15889-15894 (2003).
63. H. Feldmann, F. Feldmann, A. Marzi, Ebola: Lessons on Vaccine Development. *Annu. Rev. Microbiol.* **72**, 423-446 (2018).
64. L. He *et al.*, Presenting native-like trimeric HIV-1 antigens with self-assembling nanoparticles. *Nat. Commun.* **7**, 12041 (2016).
65. L. L. He *et al.*, Proof of concept for rational design of hepatitis C virus E2 core nanoparticle vaccines. *Sci. Adv.* **6**, eaaz6225 (2020).
66. Y. G. Zhao *et al.*, Toremifene interacts with and destabilizes the Ebola virus glycoprotein. *Nature* **535**, 169-172 (2016).
67. P. Pugach *et al.*, A native-like SOSIP.664 trimer based on an HIV-1 subtype B env gene. *J. Virol.* **89**, 3380-3395 (2015).
68. R. W. Sanders *et al.*, A next-generation cleaved, soluble HIV-1 Env trimer, BG505 SOSIP.664 gp140, expresses multiple epitopes for broadly neutralizing but not non-neutralizing antibodies. *PLoS Pathog.* **9**, e1003618 (2013).
69. K. Sliepen *et al.*, Presenting native-like HIV-1 envelope trimers on ferritin nanoparticles improves their immunogenicity. *Retrovirology* **12**, 82 (2015).
70. D. Lyumkis *et al.*, Cryo-EM structure of a fully glycosylated soluble cleaved HIV-1 envelope trimer. *Science* **342**, 1484-1490 (2013).
71. J.-P. Julien *et al.*, Crystal structure of a soluble cleaved HIV-1 envelope trimer. *Science* **342**, 1477-1483 (2013).
72. F. Shaikh *et al.*, Structure-based in silico screening identifies a potent ebolavirus inhibitor from a traditional Chinese medicine library. *J. Med. Chem.* **62**, 2928-2937 (2019).
73. J. S. Ren, Y. G. Zhao, E. E. Fry, D. I. Stuart, Target identification and mode of action of four chemically divergent drugs against ebolavirus infection. *J. Med. Chem.* **61**, 724-733 (2018).
74. L. B. King *et al.*, Cross-reactive neutralizing human survivor monoclonal antibody BDBV223 targets the ebolavirus stalk. *Nat. Commun.* **10**, 1788 (2019).
75. O. Dolnik *et al.*, Ectodomain shedding of the glycoprotein GP of Ebola virus. *EMBO J.* **23**, 2175-2184 (2004).
76. T. Maruyama *et al.*, Ebola virus can be effectively neutralized by antibody produced in natural human infection. *J. Virol.* **73**, 6024-6030 (1999).

77. H. S. Yin, X. L. Wen, R. G. Paterson, R. A. Lamb, T. S. Jardetzky, Structure of the parainfluenza virus 5 F protein in its metastable, prefusion conformation. *Nature* **439**, 38-44 (2006).
78. J. Liu, W. Shu, M. B. Fagan, J. H. Nunberg, M. Lu, Structural and functional analysis of the HIV gp41 core containing an Ile573 to Thr substitution: Implications for membrane fusion. *Biochemistry* **40**, 2797-2807 (2001).
79. V. N. Malashkevich *et al.*, Core structure of the envelope glycoprotein GP2 from Ebola virus at 1.9-angstrom resolution. *Proc. Natl. Acad. Sci. U. S. A.* **96**, 2662-2667 (1999).
80. Q. Wang *et al.*, Stabilized diverse HIV-1 envelope trimers for vaccine design. *Emerg. Microbes Infect.* **9**, 775-786 (2020).
81. L. Rutten *et al.*, Structure-based design of prefusion-stabilized filovirus glycoprotein trimers. *Cell Rep.* **30**, 4540–4550.e4543 (2020).
82. J. S. McLellan *et al.*, Structure-based design of a fusion glycoprotein vaccine for respiratory syncytial virus. *Science* **342**, 592-598 (2013).
83. K. M. Hastie *et al.*, Structural basis for antibody-mediated neutralization of Lassa virus. *Science* **356**, 923-928 (2017).
84. A. Leaver-Fay *et al.*, ROSETTA3: An object-oriented software suite for the simulation and design of macromolecules. *Methods Enzymol.* **487**, 545-574 (2011).
85. R. Z. Dintzis, B. Vogelstein, H. M. Dintzis, Specific cellular stimulation in the primary immune response: experimental test of a quantized model. *Proc. Natl. Acad. Sci. U. S. A.* **79**, 884-888 (1982).
86. M. F. Bachmann, G. T. Jennings, Vaccine delivery: a matter of size, geometry, kinetics and molecular patterns. *Nat. Rev. Immunol.* **10**, 787-796 (2010).
87. C. R. Winstead, S. K. Zhai, P. Sethupathi, K. L. Knight, Antigen-induced somatic diversification of rabbit IgH genes: Gene conversion and point mutation. *J. Immunol.* **162**, 6602-6612 (1999).
88. C. D. Morris *et al.*, Differential antibody responses to conserved HIV-1 neutralizing epitopes in the context of multivalent scaffolds and native-like gp140 trimers. *mBio* **8**, e00036-00017 (2017).
89. K. A. Martins, P. B. Jahrling, S. Bavari, J. H. Kuhn, Ebola virus disease candidate vaccines under evaluation in clinical trials. *Expert Rev. Vaccines* **15**, 1101-1112 (2016).
90. P. Rijal *et al.*, Therapeutic monoclonal antibodies for Ebola virus infection derived from vaccinated humans. *Cell Rep.* **27**, 172-186.e177 (2019).
91. K. Ewer *et al.*, A monovalent chimpanzee adenovirus Ebola vaccine boosted with MVA. *N. Engl. J. Med.* **374**, 1635-1646 (2016).
92. M. Meyer, D. C. Malherbe, A. Bukreyev, Can Ebola virus vaccines have universal immune correlates of protection? *Trends Microbiol.* **27**, 8-16 (2019).
93. J. Marcandalli *et al.*, Induction of potent neutralizing antibody responses by a designed protein nanoparticle vaccine for respiratory syncytial virus. *Cell* **176**, 1420-1431.e1417 (2019).
94. J. B. Bale *et al.*, Accurate design of megadalton-scale two-component icosahedral protein complexes. *Science* **353**, 389-394 (2016).
95. T. U. J. Bruun, A. M. C. Andersson, S. J. Draper, M. Howarth, Engineering a rugged nanoscaffold to enhance plug-and-display vaccination. *ACS Nano* **12**, 8855-8866 (2018).
96. B. Zakeri *et al.*, Peptide tag forming a rapid covalent bond to a protein, through engineering a bacterial adhesin. *Proc. Natl. Acad. Sci. U. S. A.* **109**, E690-E697 (2012).

97. M.-A. Elsliger *et al.*, The JCSG high-throughput structural biology pipeline. *Acta Crystallogr. Sect. F Struct. Biol. Cryst. Commun.* **66**, 1137-1142 (2010).
98. Z. Otwinowski, W. Minor, Processing of X-ray diffraction data collected in oscillation mode. *Methods Enzymol.* **276**, 307-326 (1997).
99. A. J. McCoy *et al.*, Phaser crystallographic software. *J. Appl. Crystallogr.* **40**, 658-674 (2007).
100. E. Potterton, P. Briggs, M. Turkenburg, E. Dodson, A graphical user interface to the CCP4 program suite. *Acta Crystallogr. D Biol. Crystallogr.* **59**, 1131-1137 (2003).
101. A. Vagin, A. Teplyakov, Molecular replacement with MOLREP. *Acta Crystallogr. D Biol. Crystallogr.* **66**, 22-25 (2010).
102. P. Emsley, B. Lohkamp, W. G. Scott, K. Cowtan, Features and development of Coot. *Acta Crystallogr. D Biol. Crystallogr.* **66**, 486-501 (2010).
103. A. A. Vagin *et al.*, REFMAC5 dictionary: organization of prior chemical knowledge and guidelines for its use. *Acta Crystallogr. D Biol. Crystallogr.* **60**, 2184-2195 (2004).
104. V. B. Chen *et al.*, MolProbity: all-atom structure validation for macromolecular crystallography. *Acta Crystallogr. D Biol. Crystallogr.* **66**, 12-21 (2010).
105. W. E. Diehl *et al.*, Ebola virus glycoprotein with increased infectivity dominated the 2013-2016 epidemic. *Cell* **167**, 1088-1098.e1086 (2016).

Acknowledgments: We thank M. Law and J. Carlos de la Torre at Scripps Research and S. Shresta at La Jolla Institute for Immunology (LJI) for helpful discussions. Diffraction data were collected at the Advanced Photon Source (APS) beamline 23-IDD, and Stanford Synchrotron Radiation Lightsource (SSRL) beamline 12-2. Use of the APS was supported by the DOE, Basic Energy Sciences, Office of Science, under contract no. DE-AC02-06CH11357. Use of the SSRL was supported by the US Department of Energy, Basic Energy Sciences, Office of Science, under contract no. DE-AC02-76SF00515. **Funding:** This work was funded in part by NIH Grants AI129698 (to J.Z.), AI140844 (to J.Z. and I.A.W.), UfoVax/SFP-2018-0416, and UfoVax/SFP-2018-1013 (to J.Z.). **Author contributions:** Project design by L.H., A.C., X.L., I.A.W., and J.Z.; rational design of EBOV GPΔMuc trimers and nanoparticles by L.H. and J.Z.; plasmid design and processing by L.H. and C.S.; antigen production, purification, and biochemical characterization by A.C., L.H., X.L., E.K., and T.N.; EBOV antibody production by X.L., E.K., and T.N.; negative-stain EM by L.H. and J.Z.; DSC measurement by S.K.; crystallography by A.C. and R.L.S.; BLI

by L.H. and J.Z.; mouse serum-antigen ELISA by L.H. and X.L.; serum IgG purification by L.H. and C.S. ebolavirus-pp and MLV-pp neutralization assays by X.L.; antigen-specific mouse B cell sorting by C.S. and L.H.; mouse B cell library preparation and NGS by L.H. and C.S.; bioinformatics analysis by L.H. and J.Z.; Manuscript written by L.H., A.C., X.L., I.A.W., and J.Z. All authors were asked to comment on the manuscript. The TSRI manuscript number is 30009. **Competing interests:** The authors declare that they have no competing interests. **Data and materials availability:** All data and code to understand and assess the conclusions of this research are available in the main text, Supplementary Materials, and the PDB (accession codes 7JPI and 7JPH). Additional data related to this paper may be requested from the lead author.

Figure legends

Fig. 1. Design and characterization of EBOV GPΔmuc trimers with modified HR2 stalk. (**A**) Left: Schematic representation of EBOV GP and GPΔmuc. GP1 N/C termini ($GP1_{N/C}$), mucin-like domain (MLD), internal fusion loop (IFL), heptad repeat regions 1/2 (HR1/HR2), transmembrane region (TM), and cytoplasmic tail (CT) are labeled with *N*-linked glycans indicated as grey (mutated), red, and pink (within MLD) branches. Right: Ribbons and molecular surface models of EBOV GP (PDB: 5JQ3) with GP1 colored in dodger blue and GP2 in yellow. MLD is shown as a grey half oval and the C terminal foldon is shown as a light-green rectangle. **(B)** Schematic representation of mAb114 bound to EBOV GP (left), SEC profiles of mAb114-purified GPΔmuc and GPΔmuc-foldon (middle) from a Superdex 200 10/300 column, and BN-PAGE gel (right). **(C)** Schematic representation of mAb100 bound to EBOV GP (left), SEC profiles of mAb100-purified GPΔmuc and GPΔmuc-foldon (middle) from a Superdex 200 10/300 column, and BN-PAGE gel (right). **(D)** Ribbons models of EBOV HR2 stalk (left) and MARV HR2 stalk (right) with CX_6CC motif and residues of interest indicated. Logo analysis of EBOV and MARV HR2

sequences (middle). **(E)** Schematic representation of GPΔmuc-W615L-L (or WL^2)-foldon. **(F)** SEC profiles of 293F-expressed, mAb100-purified GPΔmuc-foldon and GPΔmuc-WL^2-foldon from a HiLoad Superdex 200 16/600 column for three production runs. **(G)** Thermostability of GPΔmuc-foldon and GPΔmuc-WL^2-foldon, with T_m, $\Delta T_{1/2}$, and T_{on} measured by DSC. **(H)** EC_{50} (μg/ml) values of EBOV GP-foldon, GPΔmuc-foldon, GPΔmuc-W615L-foldon, and GPΔmuc-WL^2-foldon binding to 10 representative antibodies.

Fig. 2. Design and characterization of EBOV GPΔmuc trimers with modified $HR1_C$ bend. **(A)** Ribbons model of a single EBOV GP protomer (PDB: 5JQ3) shown in transparent molecular surface with GP1 colored in dodger blue, GP2 in yellow, and the $HR1_C$ bends from three protomers in red. Left: side view; Right: top view. **(B)** Left: ribbons model of the HR1 region in the prefusion (top) and postfusion (bottom) states with the HR1 region colored in yellow and the $HR1_C$ bend in red. Right: zoomed-in view of the $HR1_C$ bend with the eight residues in this region shown in the stick model and labeled with the proline mutations, P^1-P^8. **(C)** SEC profiles of mAb114-purified GPΔmuc-W615L-P^n variants (n=1 to 8) from a Superdex 200 10/300 column. SEC profiles of mAb100-purified GPΔmuc-W615L-P^2 and -P^4 are shown in the red dotted line. The trimer peak is labeled with the black dashed line. **(D)** BN-PAGE gel of mAb114-purified GPΔmuc-W615L-P^n variants (n=1 to 8). **(E)** SEC profiles of 293F-expressed, mAb100-purified GPΔmuc-W615L-L-P^2 (or WL^2P^2)-foldon from a HiLoad Superdex 200 16/600 column (left) and BN-PAGE gel of SEC fractions 41-63 (55.5-62.0 ml) (right). SEC profiles from three production runs are shown. **(F)** Thermostability of GPΔmuc-WL^2P^2-foldon and GPΔmuc-WL^2P^4-foldon, with Tm, $\Delta T_{1/2}$, and Ton measured by DSC. **(G)** Antigenic profiles of GPΔMuc-foldon and GPΔmuc-WL^2P^2-foldon trimers

measured for 10 representative antibodies. Sensorgrams were obtained from an Octet RED96 instrument using a trimer titration series of six concentrations (400-12.5 nM by twofold dilution).

Fig. 3 Structural characterization of EBOV GP with stalk and HR1$_C$ mutations. (A) The 3.2 Å-resolution crystal structure of EBOV GPΔmuc-WL^{2}P^2-foldon in a ribbon model (top view and side view). GP1 is shown in dodger blue except for the glycan cap, which is in grey. GP2 is shown in yellow with the internal fusion loop (IFL) in pink. *N*-linked glycans at N238, N257, and N563 are shown as a stick model. **(B)** Ribbons model of a GPΔmuc-WL^{2}P^2 protomer in the center with inset images showing structural comparison for the HR1$_C$ bend (left), W615-sorrounding HR2 region (bottom right), and C terminus of the HR2 stalk (right). For the HR1$_C$ bend, WL^{2}P^2 is superimposed onto GPΔmuc (PDB: 5JQ3) (top) with three hydrogen bonds labeled for WL^{2}P^2 (middle) and GPΔmuc (bottom). For the W615-sorrounding HR2 region, WL^{2}P^2 is superimposed onto GPΔmuc (PDB: 5JQ3) (top) with the coiled-coil structure shown for GPΔmuc (left) and WL^{2}P^2 (right). Cα and Cβ distances for residue 615 around the three-fold axis are labeled. For the HR2 C terminus, WL^{2}P^2 is superimposed onto GP structures of SUDV (top), EBOV (middle), and BDBV (bottom) with Cα RMSD values calculated after fitting.

Fig. 4. Design and characterization of EBOV GPΔMuc-presenting nanoparticles. (**A**) Surface models of nanoparticle (NP) carriers and GPΔMuc-presenting NPs. Three NP carriers shown here are 24-meric ferritin (FR) and 60-meric E2p and I3-01. NP size is indicated by diameter (in nm). **(B)** SEC profiles of wildtype GPΔMuc (black) and WL^{2}P^2 (magenta)-presenting FR, E2p, and I3-01 NPs obtained from a Superose 6 10/300 GL column after mAb100 purification. The particle fraction is indicated by a dotted-line box for FR. **(E)** Negative stain EM images of SEC-purified GPΔMuc-WL^{2}P^2-presenting FR, E2p and I3-01 NPs. **(D)** Schematic representation of multilayered

nanoparticle design, in which a dimeric locking (LD) domain is fused to the C-terminus of a NP subunit and a T-cell epitope is fused to the C-terminus of an LD domain. **(E)** SEC profiles of GPΔMuc-WL^{2}P^2-presenting E2p NPs with LDs 1-7 and I3-02 NPs with five LDs (4-5 and 7-9) after mAb100 purification. **(F)** SEC profiles of GPΔMuc-WL^{2}P^2-presenting E2p NP with LD4 and PADRE, or E2p-L4P (left), and I3-01/v9 NP with LD7 and PADRE, or I3-01/v9-L7P (right). I3-01v9 is a variant of I3-01 with a redesigned NP-forming interface. **(G)** BN-PAGE of GPΔMuc-WL^{2}P^2-presenting FR, E2p and I3-01/v9 NPs. LD and PADRE variants are also included for E2p and I3-01/v9. Low molecular weight (m.w.) bands are circled with red dotted lines. **(H)** Negative stain EM images of SEC-purified FR as well as multilayered E2p and I3-01v9 NPs presenting GPΔMuc-WL^{2}P^2. **(I)** EC_{50} (μg/ml) values of GPΔMuc-WL^{2}P^2-foldon and GPΔMuc-WL^{2}P^2-presenting NPs binding to 10 respective antibodies. **(J)** Antigenic profiles of GPΔMuc-WL^{2}P^2-foldon and GPΔMuc-WL^{2}P^2-presenting NPs against 10 antibodies by BLI. Sensorgrams were obtained from an Octet RED96 using an antigen titration series of six concentrations (400-12.5 nM by twofold dilution for trimer, 25-0.78 nM by twofold dilution for FR, and 10-0.31nM for multilayered E2p and I3-01v9) and quantitation biosensors. The peak signals (nm) at the highest concentration are listed in the matrix. Higher color intensity indicates greater binding signal.

Fig. 5. Immunogenicity of EBOV GPΔMuc trimers and nanoparticles in mice. (A) Schematic representation of the mouse immunization protocol. **(B)** Longitudinal analysis of GP-specific antibody titers in immunized mouse sera at weeks 2, 5, 8 and 11. Top panel: EC_{50} titers (fold of dilution) calculated from ELISA binding of mouse sera from three GP trimer groups to the coating antigen, GPΔMuc-WL^{2}P^2. Bottom panel: EC_{50} titers calculated from ELISA binding of mouse sera from three NP groups to the coating antigen, GPΔMuc-WL^{2}P^2, with the GPΔMuc-WL^{2}P^2-

foldon group included for comparison. *P*-values were determined by an unpaired *t* test in GraphPad Prism 8.4.3 and are labeled on the plots, with (*) indicating the level of statistical significance. **(C)** Ebolavirus-pp (Makona) neutralization by 10 antibodies in 293 T cells. **(D)** Ebolavirus-pp (BDBV) neutralization by 10 antibodies in 293 T cells. **(E)** Ebolavirus-pp (Makona) neutralization by mouse serum IgGs in 293 T cells. **(F)** Ebolavirus-pp (BDBV) neutralization by mouse serum IgGs in 293 T cells. In (E) and (F), IgGs were purified from mouse sera of all six vaccine groups at w11, with a starting concentration of 300 μg/ml followed by three-fold dilutions. Due to limited mouse sample availability, neutralization assays were performed only once without duplicate. For mice showing enhanced ebolavirus-pp infection (neutralization%<0.0), data points are shown as dashed lines instead of fitted curves. Data points below -100% are excluded with the lowest values labeled on the neutralization plot and color-coded according to the mouse index.

Fig. 6. Immunogenicity of EBOV GPΔMuc trimers and nanoparticles in rabbits and murine B cell response profiles. (A) Schematic representation of the rabbit immunization protocol. **(B)** Longitudinal analysis of GP-specific antibody titers in immunized rabbit sera at weeks 0, 2, 5, 8, 11, and 13. **(C)** Ebolavirus-pp neutralization by rabbit serum IgGs from two trimer groups and three NP groups in 293 T cells shown for Makona (light blue) and BDBV (orange). **(D)** MLV-pp neutralization by rabbit serum IgGs in 293 T cells as control. Five vaccine groups are shown in a single plot as no MLV-pp neutralization was observed. With sufficient rabbit IgG samples, all neutralization assays in (D) and (E) were performed in duplicate. **(E)** Schematic representation of the strategy used to analyze EBOV GP-specific B cell response that combines antigen-specific bulk sorting of splenic B cells with next-generation sequencing (NGS) and antibodyomics analysis. **(B)** B-cell response profiles for the GPΔMuc-WL^{2}P^2-foldon (left) and GPΔMuc-WL^{2}P^2-E2p-L4P groups (right) and statistical comparison of key parameters derived from the profile analysis (far

right). Panel 1/2: Distribution of germline V_H/V_K genes and statistical comparison of the number of activated V_H/V_K genes (≥1% of the total population); Panel 3: Distribution of V_H/V_K somatic hypermutation (SHM) with percent (%) mutation calculated at the nucleotide (nt) level, and statistical comparison of the average degree of V_H/V_K SHM; Panel 4: Distribution of H/KCDR3 loop length and statistical comparison of two parameters, HCDR3 length and root-mean-square fluctuation (RMSF) of HCDR3 length. The RMSF value is used as an indicator of how much the HCDR3 length varies within the EBOV GP-specific antibodies from each animal.

Figure 1

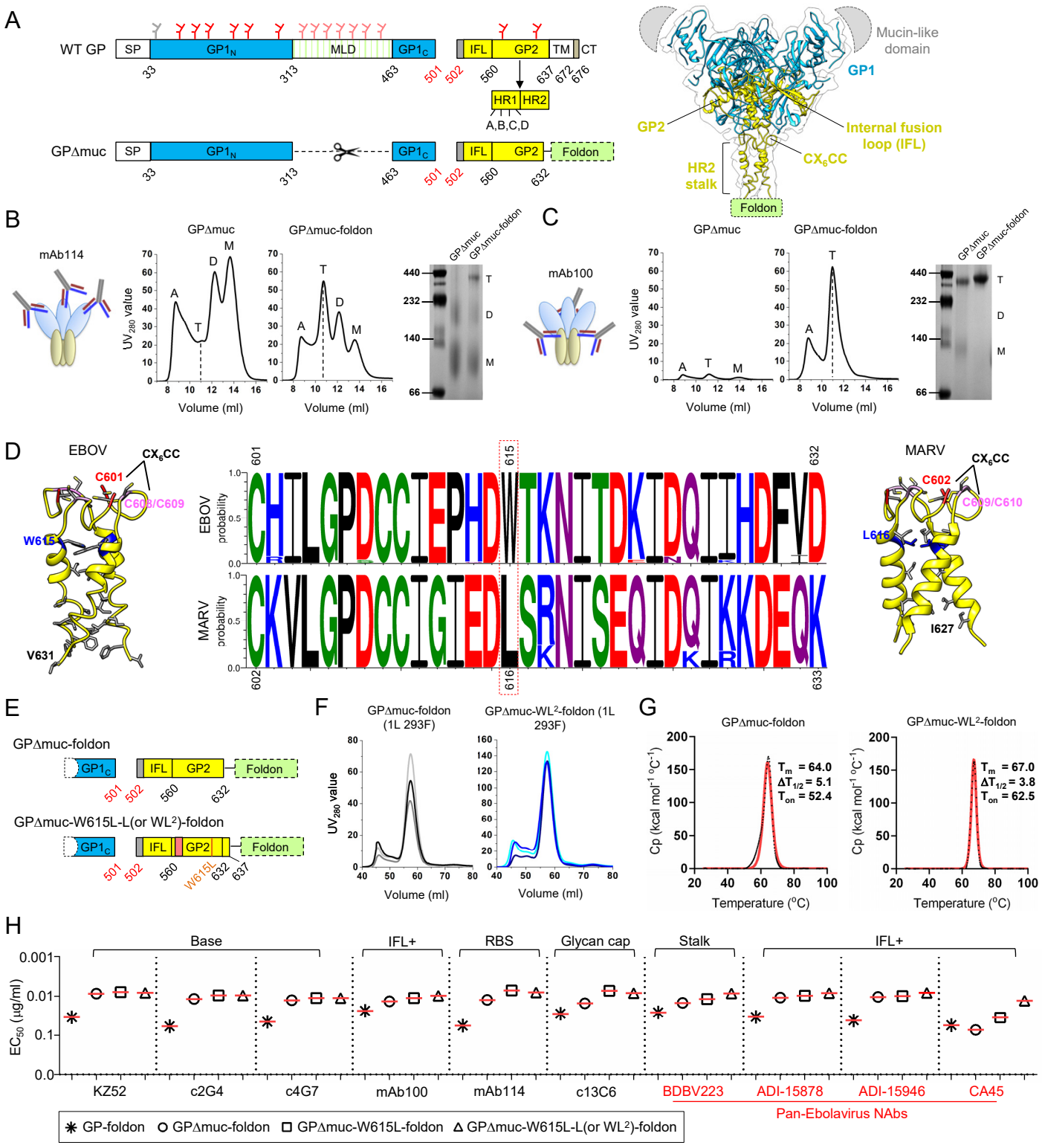
A
WT GP
SP
GP1N
MLD
GP1C
IFL
GP2
TM
CT
HR1
HR2
A,B,C,D
GPΔmuc
Foldon
Mucin-like domain
GP1
GP2
Internal fusion loop (IFL)
CX6CC
HR2 stalk
B
mAb114
GPΔmuc
GPΔmuc-foldon
UV280 value
Volume (ml)
C
mAb100
D
EBOV
MARV
probability
C601
C608/C609
W615
V631
C602
C609/C610
L616
I627
E
GPΔmuc-foldon
GPΔmuc-W615L-L(or WL2)-foldon
W615L
F
GPΔmuc-foldon (1L 293F)
GPΔmuc-WL2-foldon (1L 293F)
G
Tm = 64.0
ΔT1/2 = 5.1
Ton = 52.4
Tm = 67.0
ΔT1/2 = 3.8
Ton = 62.5
Cp (kcal mol-1 °C-1)
Temperature (°C)
H
Base
IFL+
RBS
Glycan cap
Stalk
EC50 (μg/ml)
KZ52
c2G4
c4G7
mAb100
mAb114
c13C6
BDBV223
ADI-15878
ADI-15946
CA45
Pan-Ebolavirus NAbs
GP-foldon
GPΔmuc-foldon
GPΔmuc-W615L-foldon
GPΔmuc-W615L-L(or WL2)-foldon

Figure 2

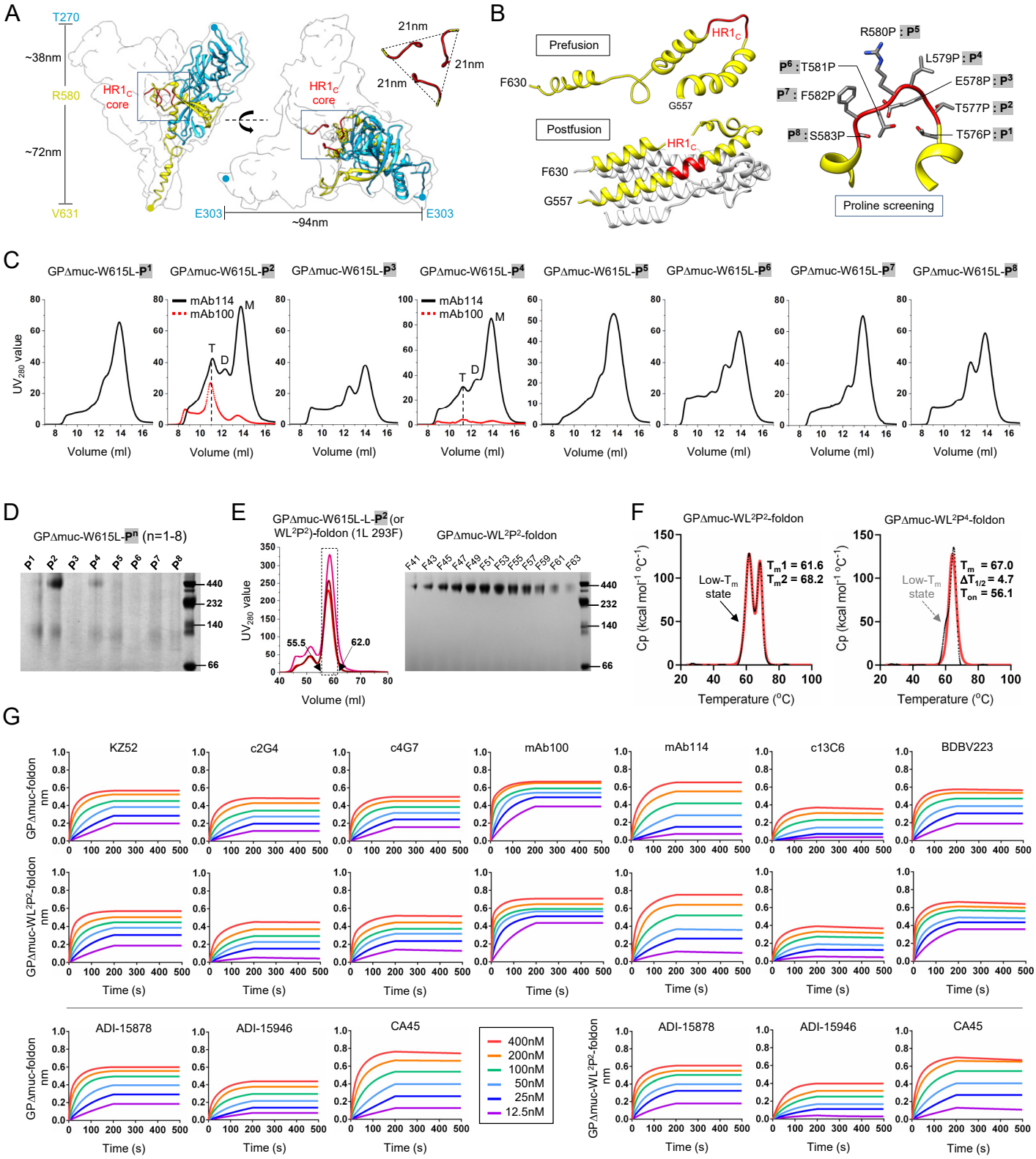
A
T270
~38nm
R580
~72nm
V631
HR1C core
E303
~94nm
21nm
B
Prefusion
F630
HR1C
G557
Postfusion
Proline screening
R580P : P5
L579P : P4
E578P : P3
T577P : P2
T576P : P1
P6 : T581P
P7 : F582P
P8 : S583P
C
GPΔmuc-W615L-P1
GPΔmuc-W615L-P2
GPΔmuc-W615L-P3
GPΔmuc-W615L-P4
GPΔmuc-W615L-P5
GPΔmuc-W615L-P6
GPΔmuc-W615L-P7
GPΔmuc-W615L-P8
mAb114
mAb100
UV280 value
Volume (ml)
D
GPΔmuc-W615L-Pn (n=1-8)
440
232
140
66
E
GPΔmuc-W615L-L-P2 (or WL2P2)-foldon (1L 293F)
GPΔmuc-WL2P2-foldon
55.5
62.0
F
GPΔmuc-WL2P2-foldon
GPΔmuc-WL2P4-foldon
Low-Tm state
Tm1 = 61.6
Tm2 = 68.2
Tm = 67.0
ΔT1/2 = 4.7
Ton = 56.1
Cp (kcal mol-1 °C-1)
Temperature (°C)
G
KZ52
c2G4
c4G7
mAb100
mAb114
c13C6
BDBV223
GPΔmuc-foldon nm
GPΔmuc-WL2P2-foldon nm
Time (s)
ADI-15878
ADI-15946
CA45
400nM
200nM
100nM
50nM
25nM
12.5nM

Figure 3

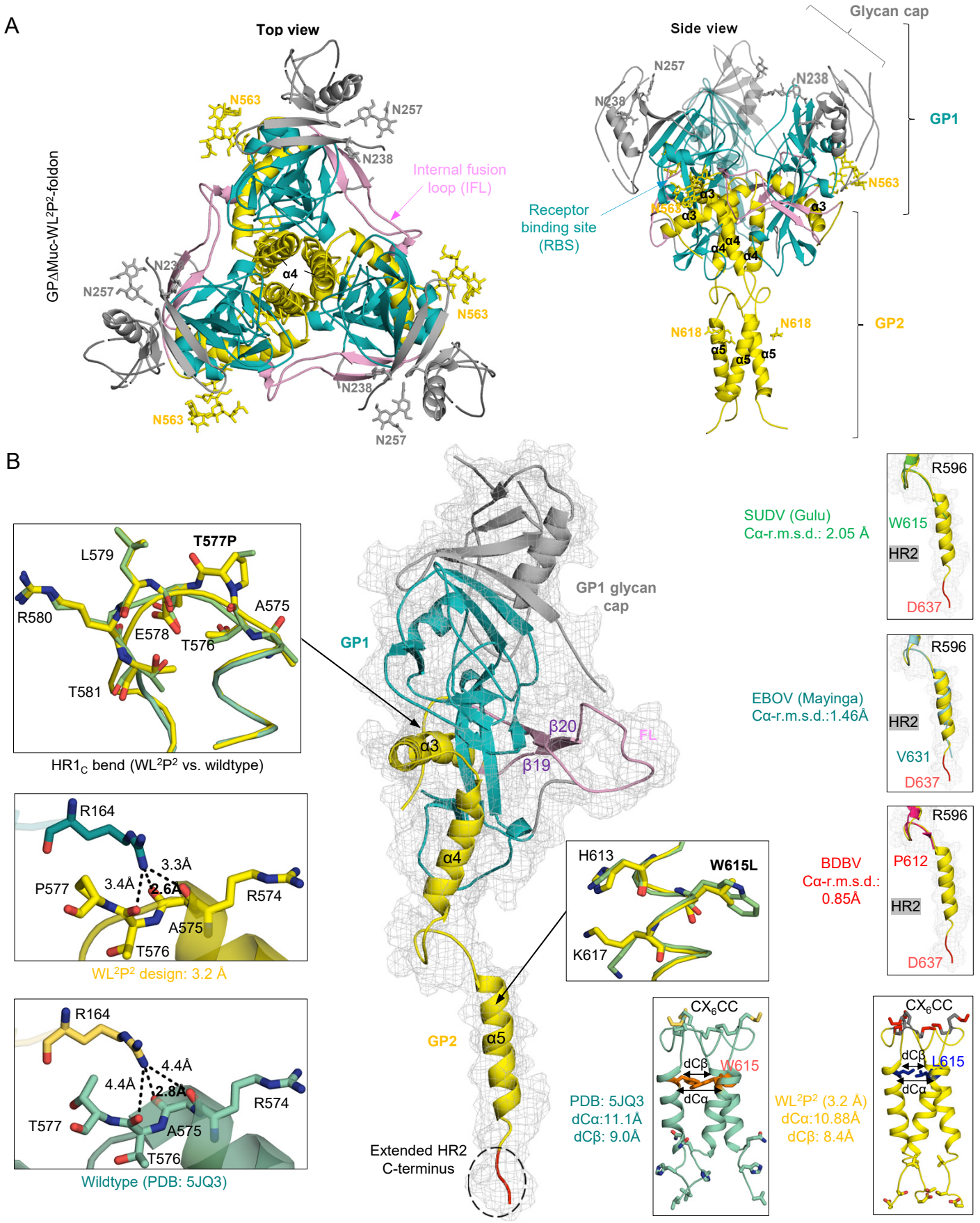
A
Top view
Side view
GPΔMuc-WL²P²-foldon
N563
N257
N238
Internal fusion loop (IFL)
α4
Glycan cap
GP1
Receptor binding site (RBS)
α3
α4
N618
α5
GP2
B
T577P
L579
R580
A575
E578
T576
T581
HR1C bend (WL²P² vs. wildtype)
R164
3.3Å
3.4Å
2.6Å
P577
R574
A575
T576
WL²P² design: 3.2 Å
4.4Å
2.8Å
T577
Wildtype (PDB: 5JQ3)
GP1 glycan cap
GP1
α3
β20
β19
FL
α4
GP2
α5
Extended HR2 C-terminus
H613
W615L
K617
SUDV (Gulu)
Cα-r.m.s.d.: 2.05 Å
R596
W615
HR2
D637
EBOV (Mayinga)
Cα-r.m.s.d.:1.46Å
V631
BDBV
Cα-r.m.s.d.: 0.85Å
P612
CX6CC
dCβ
dCα
W615
PDB: 5JQ3
dCα:11.1Å
dCβ: 9.0Å
L615
WL²P² (3.2 Å)
dCα:10.88Å
dCβ: 8.4Å

Figure 4

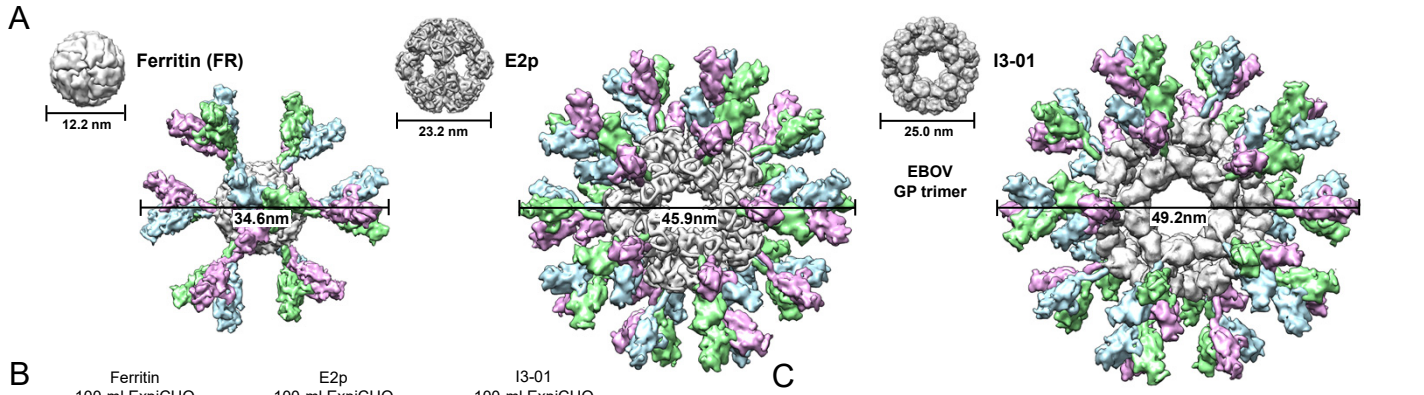

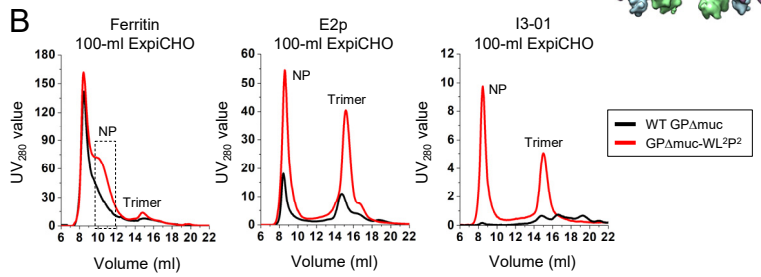

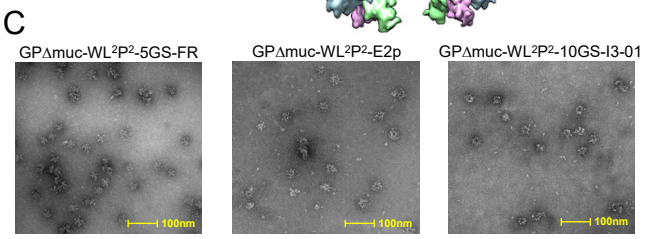

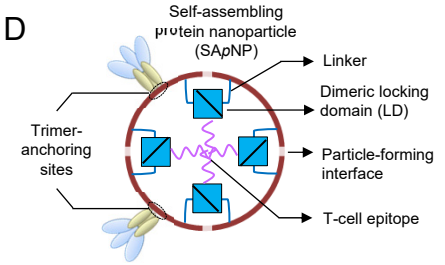

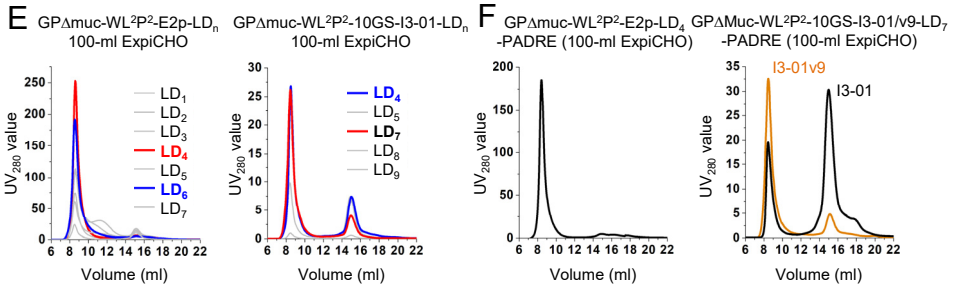

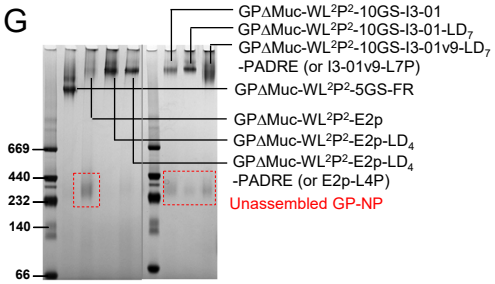

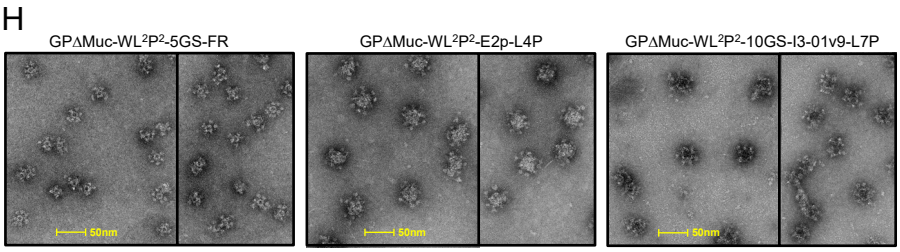

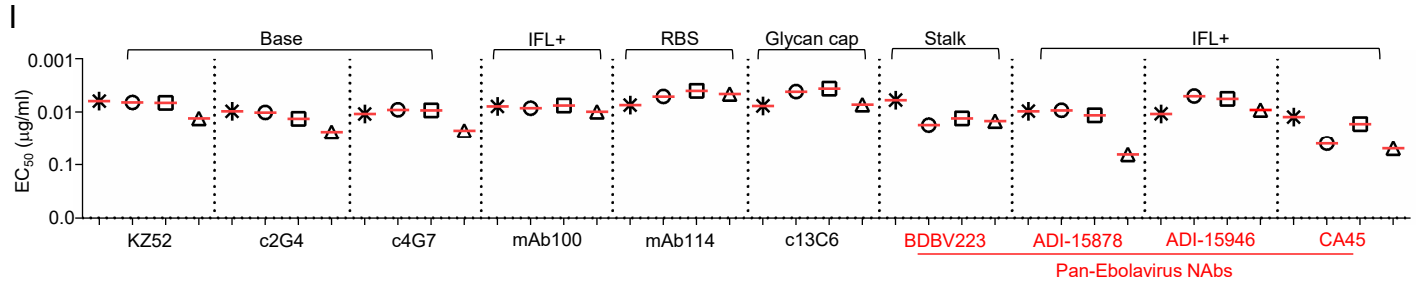

J

EBOV GP constructs:	KZ52	c2G4	c4G7	mAb100	mAb114	c13C6	BDBV223	ADI-15878	ADI-15946	CA45
GPΔmuc-WL^{2}P^2-foldon	0.67	0.53	0.60	0.81	0.85	0.50	0.63	0.67	0.49	0.79
GPΔmuc-WL^{2}P^2-5GS-FR	1.41	1.25	1.42	1.69	1.80	1.40	1.37	1.30	1.33	1.15
GPΔmuc-WL^{2}P^2-E2p-L4P	1.39	0.93	1.34	1.54	2.05	1.69	1.30	1.04	1.14	1.12
GPΔmuc-WL^{2}P^2-10GS-I3-01v9-L7P	1.09	1.01	1.30	1.63	1.63	1.39	1.41	1.07	1.26	0.83

Figure 5

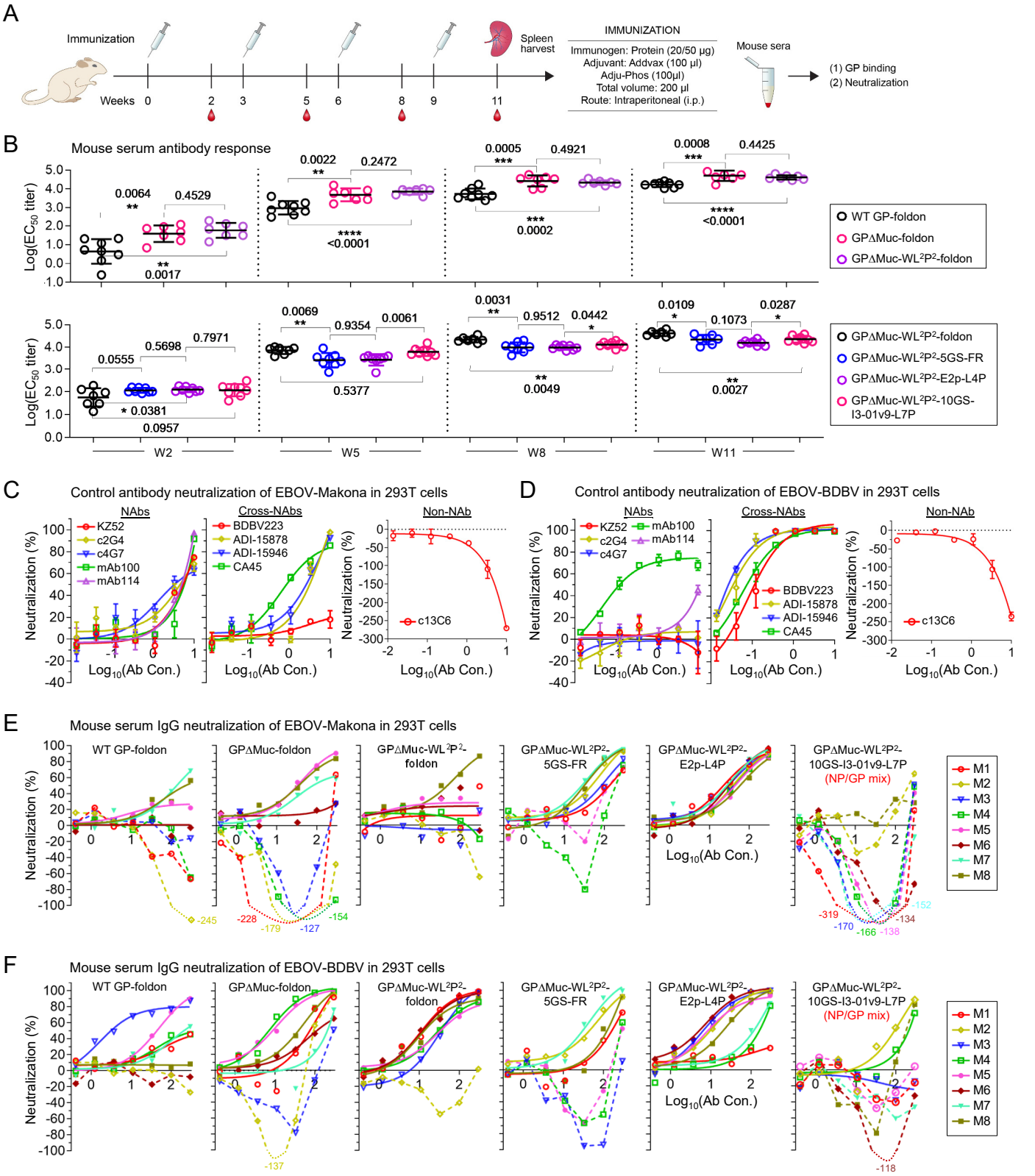
A
Immunization
Weeks 0 2 3 5 6 8 9 11
Spleen harvest
IMMUNIZATION
Immunogen: Protein (20/50 µg)
Adjuvant: Addvax (100 µl)
Adju-Phos (100µl)
Total volume: 200 µl
Route: Intraperitoneal (i.p.)
Mouse sera
(1) GP binding
(2) Neutralization
B
Mouse serum antibody response
Log(EC50 titer)
WT GP-foldon
GPΔMuc-foldon
GPΔMuc-WL2P2-foldon
GPΔMuc-WL2P2-5GS-FR
GPΔMuc-WL2P2-E2p-L4P
GPΔMuc-WL2P2-10GS-I3-01v9-L7P
W2
W5
W8
W11
C
Control antibody neutralization of EBOV-Makona in 293T cells
NAbs
Cross-NAbs
Non-NAb
KZ52
c2G4
c4G7
mAb100
mAb114
BDBV223
ADI-15878
ADI-15946
CA45
c13C6
Neutralization (%)
Log10(Ab Con.)
D
Control antibody neutralization of EBOV-BDBV in 293T cells
E
Mouse serum IgG neutralization of EBOV-Makona in 293T cells
WT GP-foldon
GPΔMuc-foldon
GPΔMuc-WL2P2-foldon
GPΔMuc-WL2P2-5GS-FR
GPΔMuc-WL2P2-E2p-L4P
GPΔMuc-WL2P2-10GS-I3-01v9-L7P
(NP/GP mix)
M1
M2
M3
M4
M5
M6
M7
M8
F
Mouse serum IgG neutralization of EBOV-BDBV in 293T cells

Figure 6

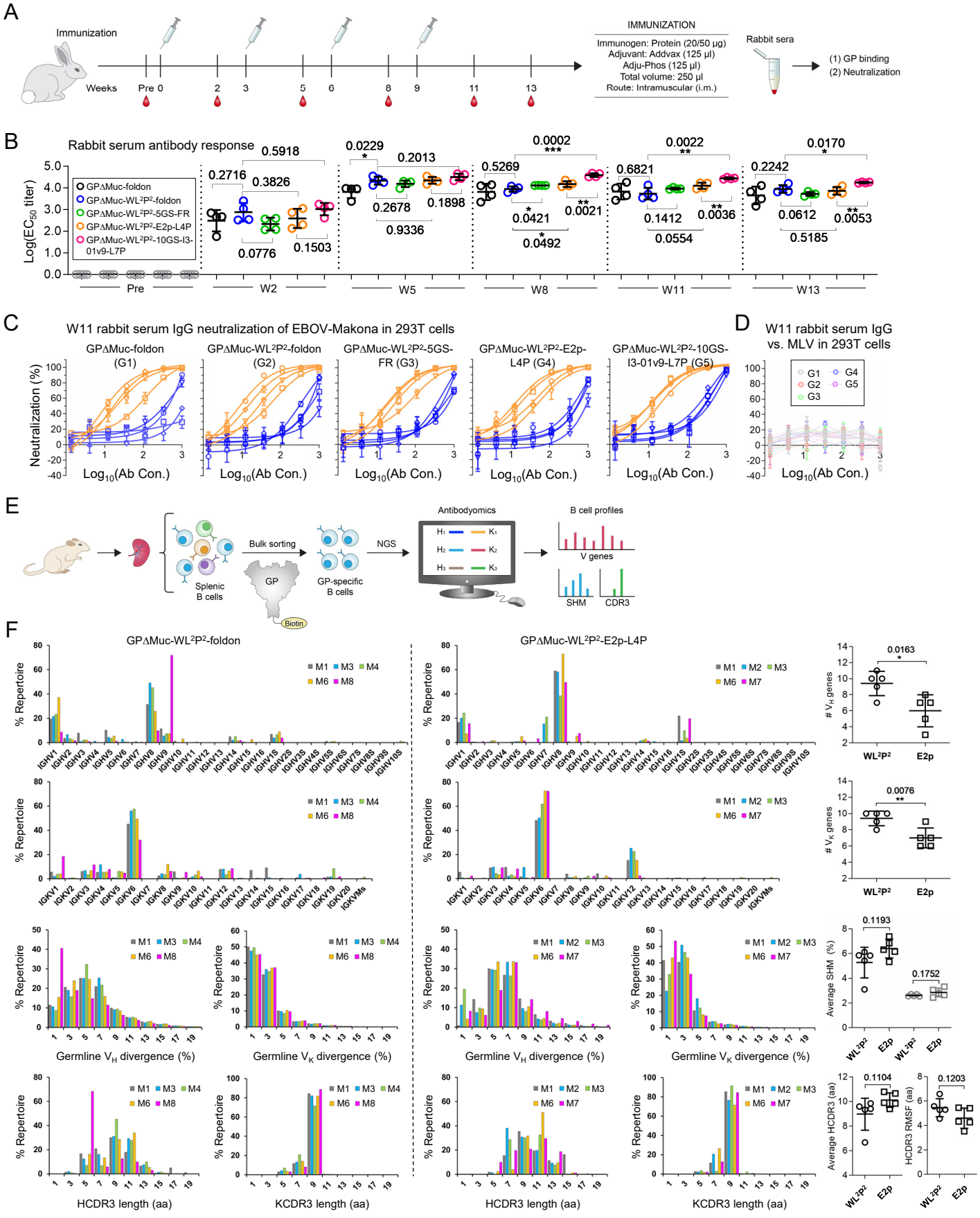
A
Immunization
Weeks
Pre 0
2
3
5
6
8
9
11
13
IMMUNIZATION
Immunogen: Protein (20/50 µg)
Adjuvant: Addvax (125 µl)
Adju-Phos (125 µl)
Total volume: 250 µl
Route: Intramuscular (i.m.)
Rabbit sera
(1) GP binding
(2) Neutralization
B
Rabbit serum antibody response
Log(EC50 titer)
GPΔMuc-foldon
GPΔMuc-WL2P2-foldon
GPΔMuc-WL2P2-5GS-FR
GPΔMuc-WL2P2-E2p-L4P
GPΔMuc-WL2P2-10GS-I3-01v9-L7P
Pre
W2
W5
W8
W11
W13
C
W11 rabbit serum IgG neutralization of EBOV-Makona in 293T cells
GPΔMuc-foldon (G1)
GPΔMuc-WL2P2-foldon (G2)
GPΔMuc-WL2P2-5GS-FR (G3)
GPΔMuc-WL2P2-E2p-L4P (G4)
GPΔMuc-WL2P2-10GS-I3-01v9-L7P (G5)
Neutralization (%)
Log10(Ab Con.)
D
W11 rabbit serum IgG vs. MLV in 293T cells
E
Splenic B cells
Bulk sorting
GP
Biotin
GP-specific B cells
NGS
Antibodyomics
B cell profiles
V genes
SHM
CDR3
F
GPΔMuc-WL2P2-foldon
GPΔMuc-WL2P2-E2p-L4P
% Repertoire
Germline VH divergence (%)
Germline VK divergence (%)
HCDR3 length (aa)
KCDR3 length (aa)
VH genes
VK genes
Average SHM (%)
Average HCDR3 (aa)
HCDR3 RMSF (aa)
WL2P2
E2p

fig. S1

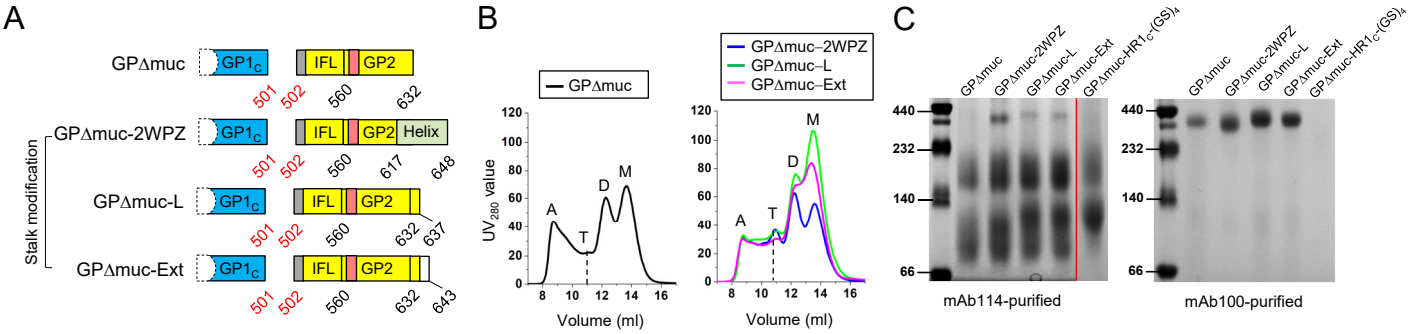

D **Antigenic profiling of four mAb100/SEC-purified, stalk-modified EBOV GP/GPΔmuc-foldon trimers**

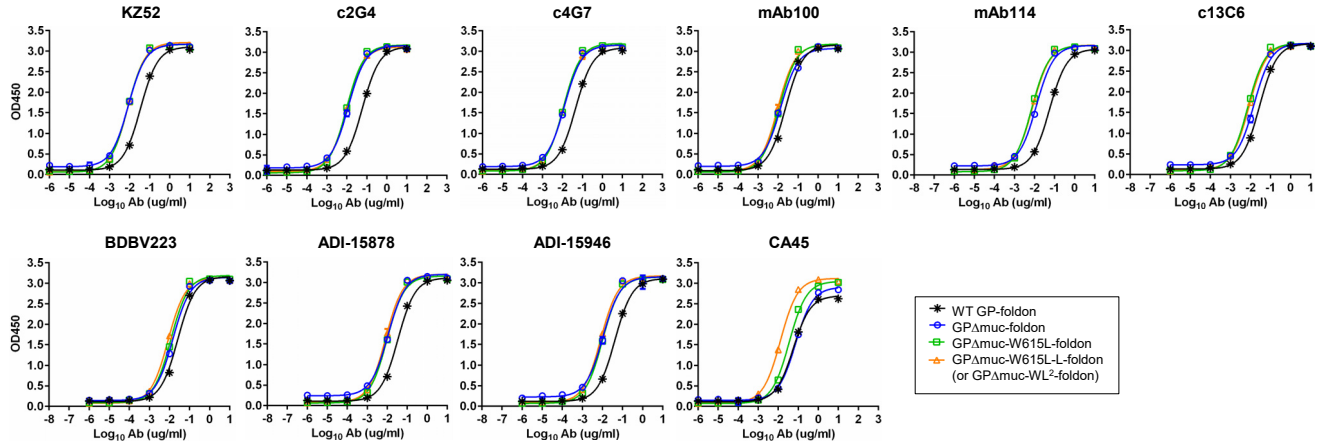

E **EC_{50} values of four EBOV GP/GPΔmuc trimers binding to 10 antibodies [a].**

	KZ52	C2G4	C4G7	MAb100	MAb114	C13C6	BDBV223	ADI-15878	ADI-15946	CA45
WT GP-foldon	0.035	0.059	0.045	0.024	0.056	0.028	0.026	0.034	0.042	0.056
GPΔmuc-foldon	0.009	0.012	0.013	0.013	0.012	0.015	0.015	0.011	0.010	0.073
GPΔmuc-W615L-foldon	0.008	0.009	0.011	0.011	0.007	0.007	0.012	0.010	0.010	0.035
GPΔmuc-WL^2-foldon	0.008	0.010	0.011	0.010	0.008	0.008	0.008	0.008	0.008	0.013

[a] EC_{50} values were calculated from the besting fitting in GraphPad Prism v8.4.3.

F **Antigenic profiling of an mAb100/SEC-purified, stalk/$HR1_C$-modified EBOV GPΔmuc-foldon trimer**

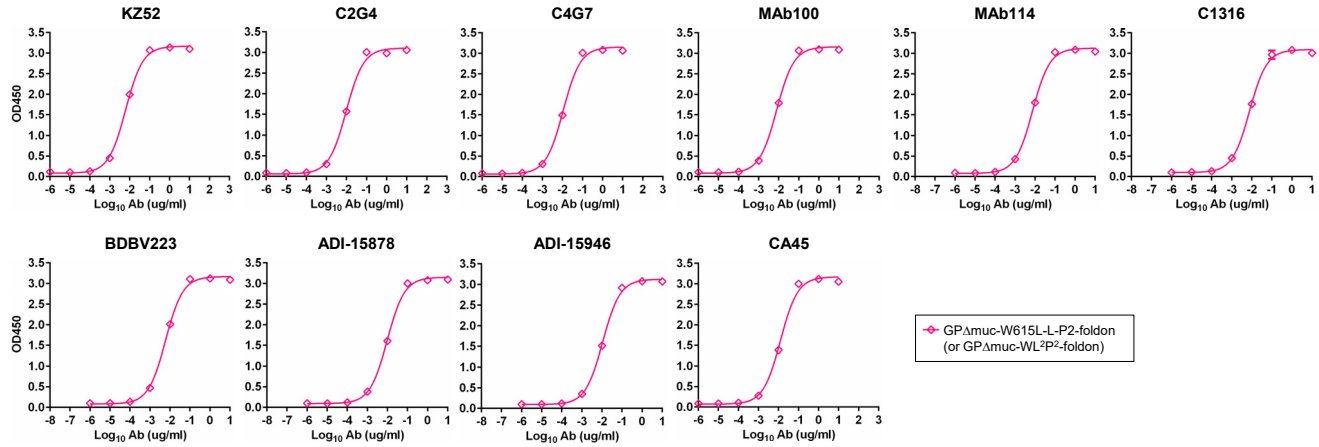

G **EC_{50} values of a stalk/$HR1_C$-modified EBOV GPΔmuc trimer binding to 10 antibodies [a].**

	KZ52	C2G4	C4G7	MAb100	MAb114	C1316	BDBV223	ADI-15878	ADI-15946	CA45
GPΔMuc-WL^2P^2-foldon	0.006	0.010	0.011	0.008	0.007	0.008	0.006	0.010	0.011	0.012

[a] EC_{50} values were calculated from the besting fitting in GraphPad Prism v8.4.3.

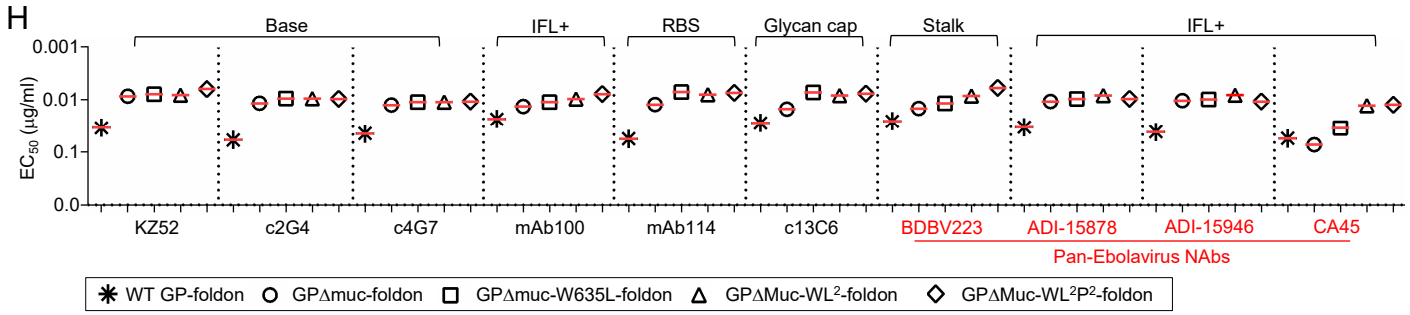

fig. S1. Design, screening, and antigenic characterization of EBOV GPΔmuc trimers with modified stalk and $HR1_C$. (A) Schematic representation of a mucin-deleted GP (GPΔmuc) and three stalk designs (GPΔmuc-2WPZ, GPΔmuc-L, and GPΔmuc-Ext). **(B)** SEC profiles of four GPΔmuc constructs obtained from a Superdex 200 10/300 column following transient expression in 250 ml HEK293 F cells and mAb114 purification. Left: the SEC curve of GPΔmuc shown in black line; Right: three stalk designs shown in blue, green, and magenta lines for GPΔmuc-2WPZ, -L, and -Ext, respectively. **(C)** BN-PAGE of GPΔmuc proteins purified by mAb114 (left) and mAb110 (right) columns. Of note, an additional GPΔmuc construct with the 8-aa $HR1_C$ replaced by a flexible $(GS)_4$ loop is included for comparison. The red line indicates that the BN-PAGE gel of GPΔmuc-$HR1_C$-$(GS)_4$ was generated in a different experiment. **(D)** ELISA curves of four mAb100/SEC-purified, stalk-modified EBOV GP/GPΔmuc-foldon trimers binding to 10 antibodies. (**E**) Summary of EC_{50} values (μg/ml) of EBOV GP/GPΔmuc-foldon trimers binding to 10 antibodies. **(F)** ELISA curves of an mAb100/SEC-purified, stalk/$HR1_C$-modified EBOV GPΔmuc-foldon trimer binding to 10 antibodies. (**G**) Summary of EC_{50} values (μg/ml) of a stalk/$HR1_C$-modified EBOV GPΔmuc-foldon trimer binding to 10 antibodies. **(H)** Plot of EC_{50} (μg/ml) values of five GP/GPΔmuc-foldon trimers binding to 10 antibodies. Four pan-Ebolavirus NAbs are colored in red. In **(E)** and **(G)**, EC_{50} values were calculated for all ELISA data in Prism version 8.4.3.

A

Inter-protomer disulfide bond (SS) mutations

#	Res1	Res2	$d_{C\beta}$	Comments
SS1	TYR534	PHE153	3.82	IFL-head
SS2	ALA538	GLY91	3.99	IFL-head
SS3	THR520	ALA575	4.01	IFL-NHR
—	TRP615	ILE603	4.14	Hydrophobic cluster
SS4	ILE532	GLY157	4.20	IFL-head
SS5	ASP522	ALA575	4.41	IFL-NHR
	GLU611	HIS602	4.59	SS cysteine
SS6	LYS56	GLY599	4.60	Stalk (HR2)
—	CYS609	THR600	4.62	SS cysteine
	TRP531	GLN567	4.73	$d_{C\beta}$ > **cutoff**

A C_β-C_β distance of 4.72 Å as the indicator of S-S bond formation

B

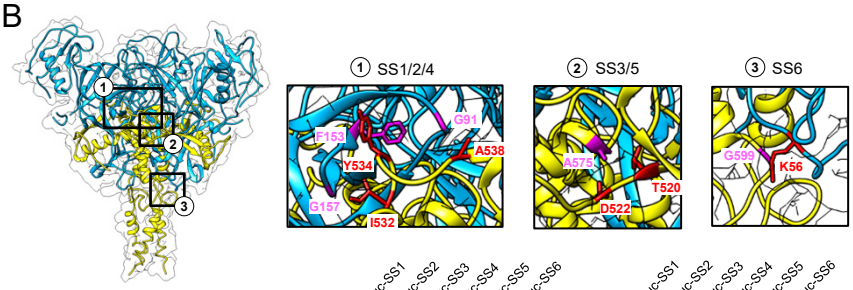

C

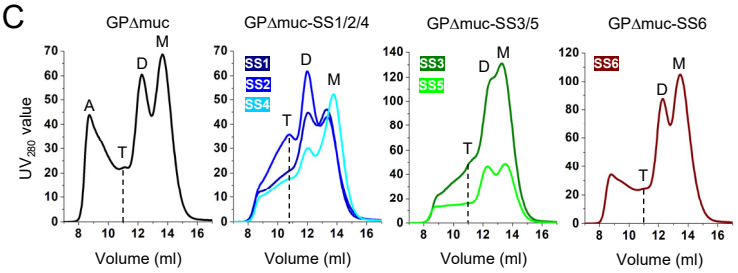

D

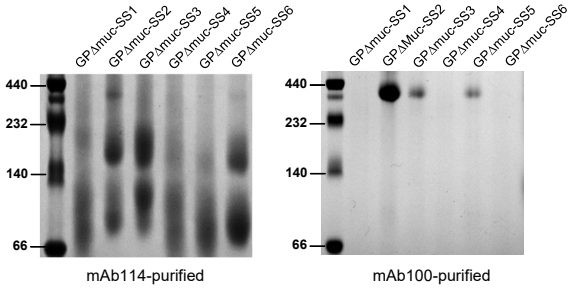

E **Antigenic screening of mAb100-purified GPΔmuc-SS2/3/5 trimers against six representative antibodies**

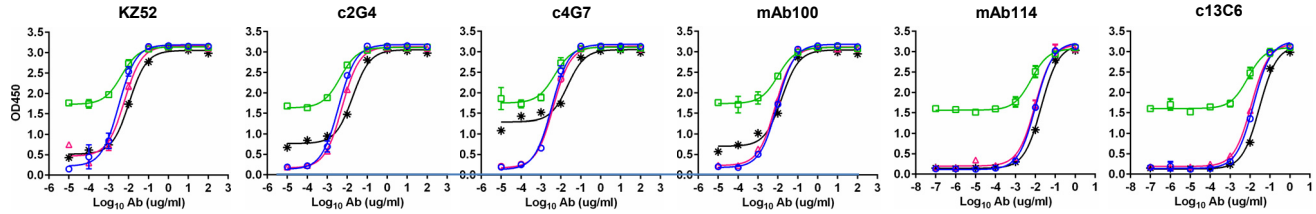

F **EC_{50} values of EBOV GPΔmuc-SS2/3/5 trimers binding to six representative antibodies [a].**

	KZ52	c2G4	c4G7	mAb100	mAb114	c13C6
GPΔmuc	0.011	0.019	0.022	0.016	0.020	0.030
GPΔmuc-SS2	0.003	0.014	0.021	0.014	0.013	0.017
GPΔmuc-SS3[b]	0.004	0.030	0.016	0.029	0.014	0.023
GPΔmuc-SS5	0.006	0.011	0.006	0.019	0.015	0.024

[a] EC_{50} values were calculated from the besting fitting in GraphPad Prism 8.4.3.
[b] GPΔmuc and GPΔmuc-SS3 showed high baselines likely due to the formation of higher molecular weight (m.w.) aggregates. EC_{50} is calculated as an estimate of the binding affinity in these cases.

G

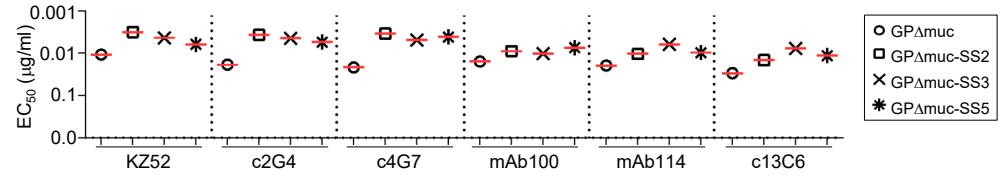

fig. S2. Design and characterization of EBOV GPΔMuc trimers with inter-protomer disulfide bonds. (A) Inter-protomer disulfide bond (SS) mutations identified using the atomic structure of a WT GPΔmuc trimer (PDB: 5JQ3) with residue numbers, C_β-C_β distance, and location listed as the key parameters for selection. **(B)** Structural model and molecular surface of EBOV GPmMuc trimer (PDB: 5JQ3) in transparent molecular surface with the three SS classes labeled according to their locations. Zoomed-in views of the three SS classes, SS1/2/4, SS3/5, and SS6, are shown on the right. **(C)** SEC profiles of HEK293 F-expressed, mAb114-purified GPΔmuc and SS mutants (A: aggregate; T: trimer; D: dimer; M: monomer). **(D)** BN-PAGE of six SS mutants after purification using an mAb114 column (left) and an mAb100 column (right). **(E)** ELISA curves of mAb100-purified GPΔmuc and SS2/3/5 mutants binding to six representative antibodies. **(F)** EC_{50} values of mAb100-purified GPΔmuc and SS2/3/5 mutants binding to six antibodies. EC_{50} values were calculated for all ELISA data in Prism 8.4.3. **(G)** Plot of EC_{50} (μg/ml) values of GPΔMuc and SS2/3/5 mutants binding to six antibodies.

fig. S3

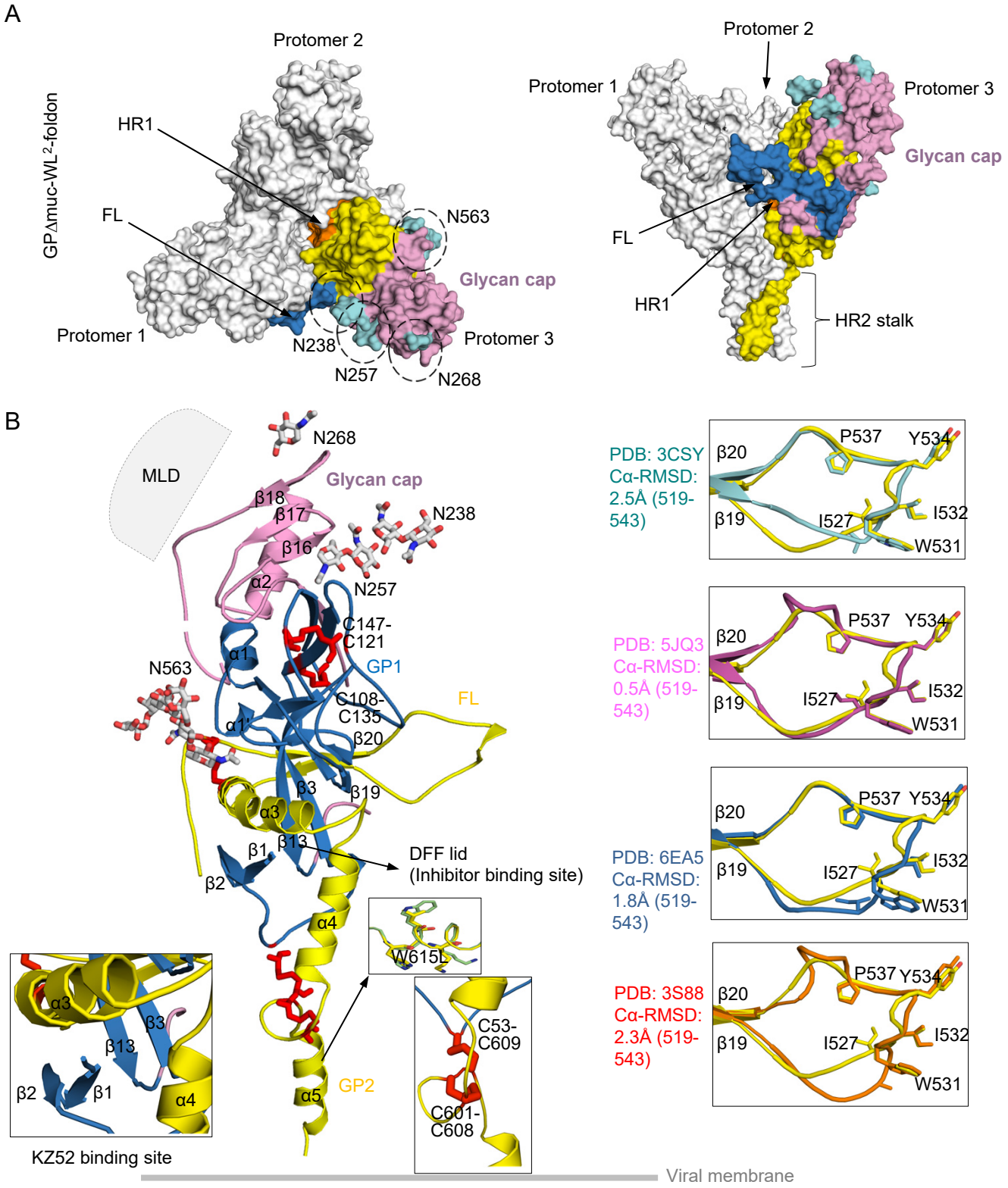

fig. S3. A 2.3 Å-resolution structure of GPΔmuc-WL^2-foldon. (A) Molecular surface of GPΔmuc-WL^2-foldon in top view and side view. Protomers 1 and 2 are colored in light grey and 3 is colored differently for various structural components: HR1 (orange), IFL(blue), glycan cap (pink), and HR2 (yellow). N-linked glycans at N238, N257, N268 and N563 are highlighted in circles. **(B)** Ribbon diagram of a GPΔmuc-WL^2-foldon protomer with the color scheme as in (A). Glycans are shown in a stick model and disulfide bonds are shown as red sticks. The mucin domain is shown as a grey oval. Binding sites for KZ52 and small-molecule inhibitors are indicated. The W615L mutation and two critical disulfide bonds (C53-C609 and C601-C608) are shown as insets. Superposed IFLs (R519-E543) from WL^2 and known structures (PDBs: 3CSY,5JQ3, 6EA5 and 3S88) are shown as insets (right), with Cα RMSD values of 1.8-2.5Å.

fig. S4

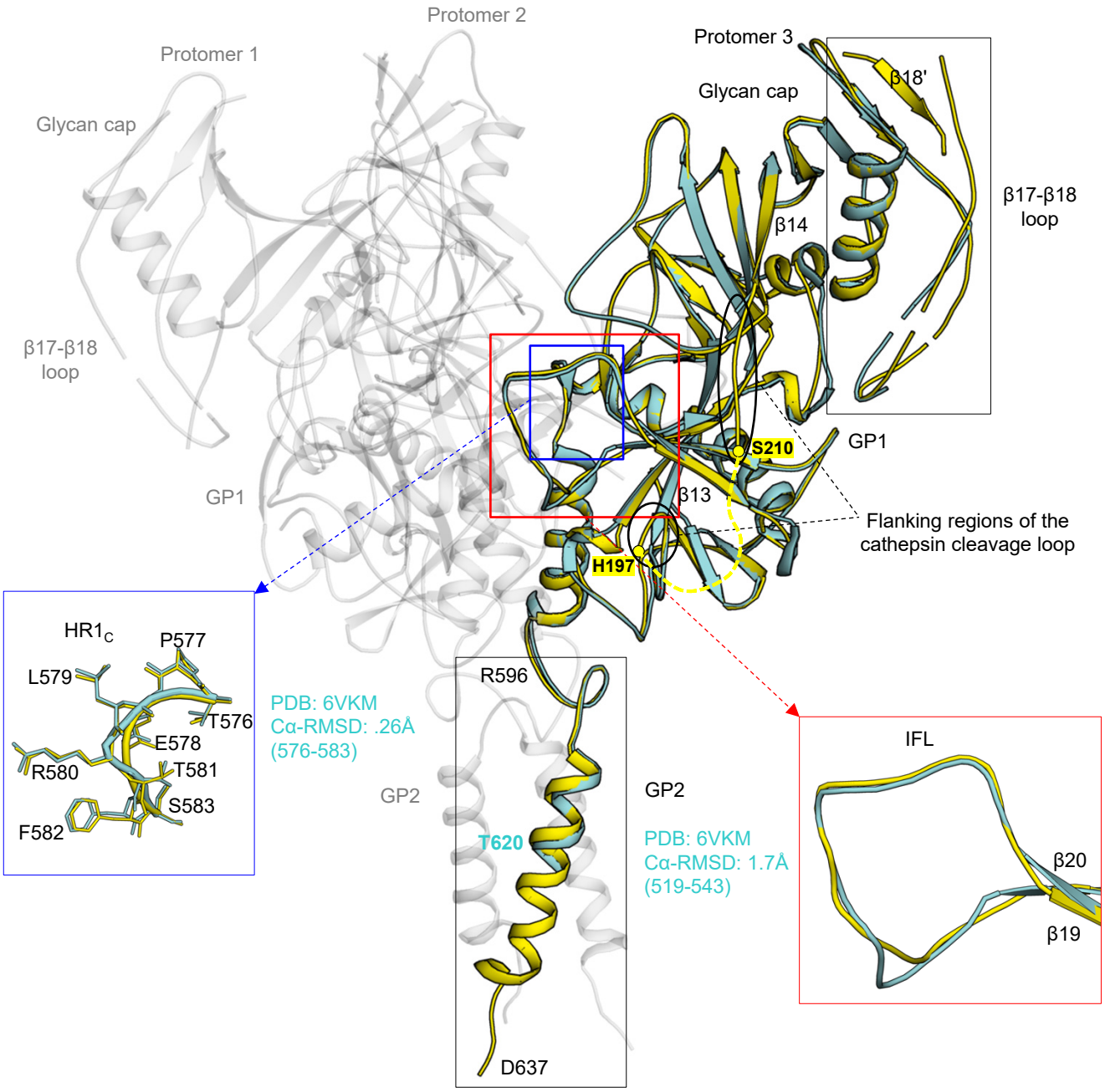

fig. S4. Structural comparison of Mayinga GPΔmuc-WL^2-foldon and Makona GPΔmuc with the T577P/R588E mutation (PDB: 6VKM). In the GPΔmuc-WL^2-foldon trimer, Protomers 1/2 and 3 are shown in light grey and yellow, respectively. One protomer from the Makona GPΔmuc (PDB: 6VKM) is superimposed onto protomer 3 and shown in cyan. Superimposed HR1$_C$ regions and internal fusion loops (IFL) from the two structures are shown in the bottom left and right insets, respectively. The flanking regions of the cathepsin cleavage loop (between β13 and β14, aa 190-210) are indicated in a black oval. H197 and S210 are labeled. The unstructured cathepsin cleavage loop between H197 and S210 is indicated as a yellow dashed line.

fig. S5

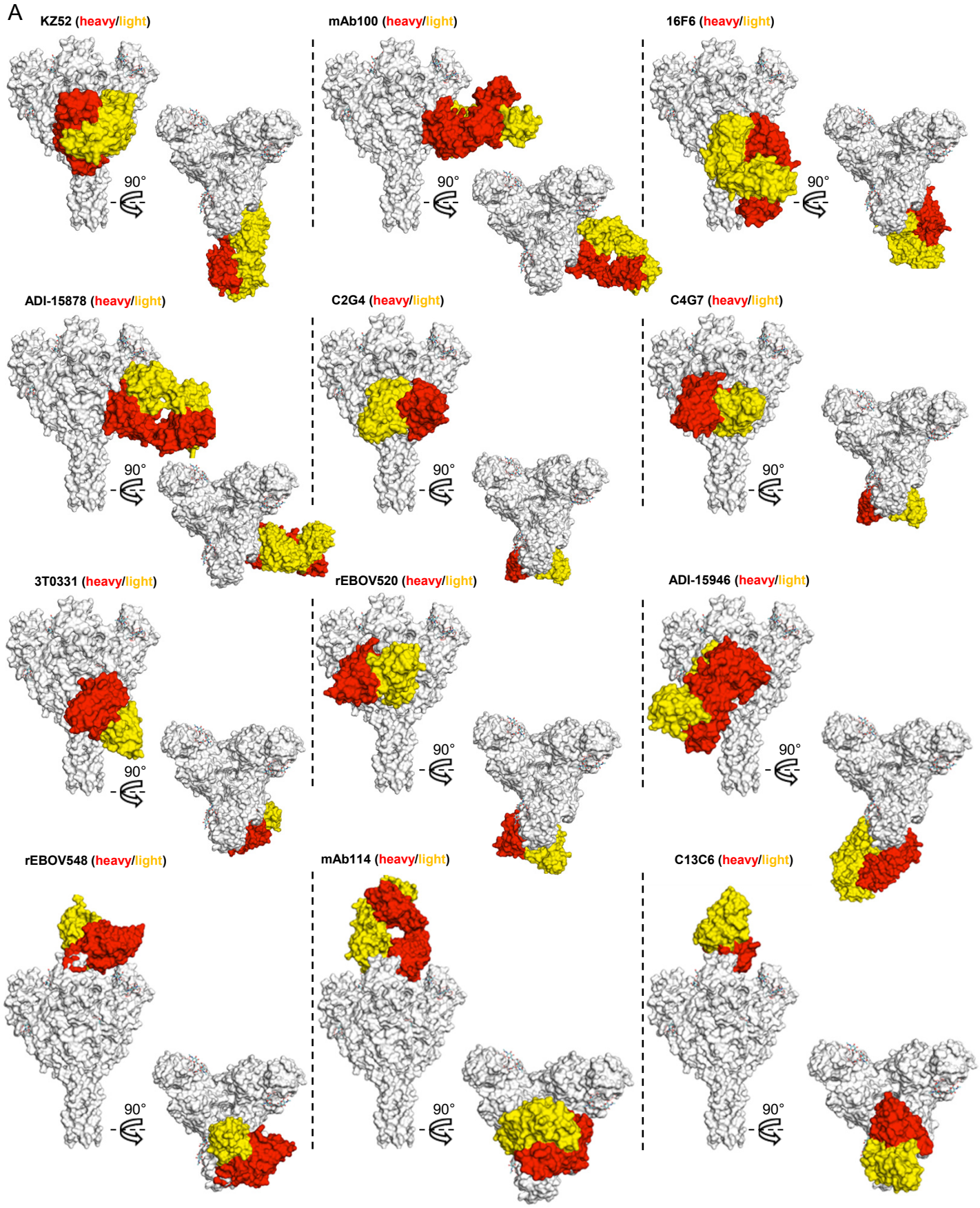
A
KZ52 (heavy/light)
mAb100 (heavy/light)
16F6 (heavy/light)
ADI-15878 (heavy/light)
C2G4 (heavy/light)
C4G7 (heavy/light)
3T0331 (heavy/light)
rEBOV520 (heavy/light)
ADI-15946 (heavy/light)
rEBOV548 (heavy/light)
mAb114 (heavy/light)
C13C6 (heavy/light)
90°

fig. S5

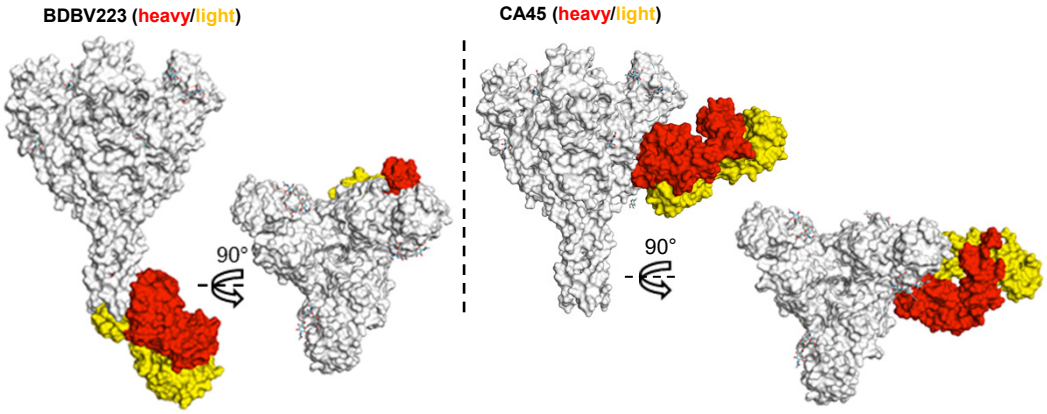

B

```
     32                 47                60
5KEN -IPLGVIHNSTLQVSDVDKLVCRDKLSST C4G7
5KEL -IPLGVIHNSTLQVSDVDKLVCRDKLSST C2G4/C13C6
3CSY SIPLGVIHNSVLQVSDVDKLVCRDKLSST KZ52
3S88 SMPLGVVTNSTLEVTEIDQLVCKDHLAST 16F6
6EA5 -IPLGVVHNNTLQVSDIDKLVCRDKLSST ADI-15878
5FHC SIPLGVIHNSTLQVSDVDKLVCRDKLSST mAB100/mAB114
6PCI SIPLGVIHNSTLQVSDVDKLVCRDKLSST rEBOV548/rEBOV520
6MAM SIPLGVIHNSTLQVSDVDKLVCRDKLSST ADI-15946
6QD7 SIPLGVIHNSALQVSDVDKLVCRDKLSST 3T0331
6N7J ---------------------------- BDBV223
6EAY SIPLGVIHNSTLQVSDVDKLVCRDKLSST CA45

                70                                  100                   120
5KEN NQLRSVGLNLEGNGVATDVPSATKRWGFRSGVPPKVVNYEAGEWAENCYNLEIKKPDGSE C4G7
5KEL NQLRSVGLNLEGNGVATDVPSATKRWGFRSGVPPKVVNYEAGEWAENCYNLEIKKPDGSE C2G4/C13C6
3CSY NQLRSVGLNLEGNGVATDVPSATKRWGFRSGVPPKVVNYEAGEWAENCYNLEIKKPDGSE KZ52
3S88 DQLKSVGLNLEGSGVSTDIPSATKRWGFRSGVPPKVVSYEAGEWAENCYNLEIKKPDGSE 16F6
6EA5 SQLASVGLNLEGNGVATDVPTATKRWGFRAGVPPKVVNYEAGEWAENCYNLDIKKADGSE ADI-15878
5FHC NQLRSVGLNLEGNGVATDVPSATKRWGFRSGVPPKVVNYEAGEWAENCYNLEIKKPDGSE mAB100/mAB114
6PCI NQLRSVGLNLEGNGVATDVPSVTKRWGFRSGVPPKVVNYEAGEWAENCYNLEIKKPDGSE rEBOV548/rEBOV520
6MAM NQLRSVGLNLEGNGVATDVPSATKRWGFRSGVPPKVVNYEAGEWAENCYNLEIKKPDGSE ADI-15946
6QD7 NQLRSVGLNLEGNGVATDVPSATKRWGFRSGVPPKVVNYEAGEWAENCYNLEIKKPDGSE 3T0331
6N7J ------------------------------------------------------------ BDBV223
6EAY NQLRSVGLNLEGNGVATDVPSATKRWGFRSGVPPKVVNYEAGEWAENCYNLEIKKPDGSE CA45

     136            186                        211                                240
5KEN RYVHKVSGTGPCALPQAKKDFFSSHPLREPVNATEDPSSGYYSTTIRYQATGFGTNETEYLFEVDNLT C4G7
5KEL RYVHKVSGTGPCALPQAKKDFFSSHPLREPVNATEDPSSGYYSTTIRYQATGFGTNETEYLFEVDNLT C2G4/C13C6
3CSY RYVHKVSGTGPCALPQAKKDFFSSHPLREPVNATEDPSSGYYSTTIRYQATGFGTNEVEYLFEVDNLT KZ52
3S88 RYVHKAQGTGPCPLAKPKETFLQSPPIREAVNYTENTSSYYATSYLEYEIENFGAQHSTTLFKIDNNT 16F6
6EA5 RYVHKVSGTGPCPLPETKKDFFEI------------------------------------------ ADI-15878
5FHC RYVHKVSGTGPCALPQAKKDFFSSHPLREPVNATEDPSSGYYSTTIRYQATGFGTNETEYLFEVDNLT mAB100/mAB114
6PCI RYVHKVSGTGPCALPQAKKDFFSSHPLREPVNATEDPSSGYYSTTIRYQATGFGTNETEYLFEVDNLT rEBOV548/rEBOV520
6MAM RYVHKVSGTGPCALPQAKKDFFSSHPLREPVNATEDPSSGYYSTTIRYQATGFGN------------- ADI-15946
6QD7 RYVHKVSGTGPCALPQAKKDFFSSHPLREPVNATEDPSSGYYSTTIRYQATGFGTNETEYLFEVDNLT 3T0331
6N7J ------------------------------------------------------------ BDBV223
6EAY RYVHKVSGTGPCALPQAKKDFFSSHPLREPVNATEDPSSGYYSTTIRYQATGFGTNETEYLFEVDNLT CA45

     241                                270                          302
5KEN YVQLESRFTPQFLLQLNETIYTSGKRSNTTGKLIWKVNPEIDTTIGEWAFWETKKNLIRSEELSFA-- C4G7
5KEL YVQLESRFTPQFLLQLNETIYTSGKRSNTTGKLIWKVNPEIDTTIGEWAFWETKKNLIRSEELSFTVV C2G4/C13C6
3CSY YVQLESRFTPQFLLQLNETIYTSGKRSNTTGKLIWKVNPEIDTTIGEWAFWETKKNLIRSEELSFTVV KZ52
3S88 FVRLDRPHTPQFLFQLNDTIHLHQQLSNTTGRLIWTLDANINADIGEWAFWENKKNLLRGEELSFEAL 16F6
6EA5 ------------------------------------------------------------------- ADI-15878
5FHC YVQLESRFTPQFLLQLNETIYTSGKRSNTTGKLIWKVNPEIDTTIGEWAFWETKKNLIRSEELSFSR- mAB100/mAB114
6PCI YVQLESRFTPQFLLQLNETIYASGKRSNTTGKLIWKVNPEIDTTIGEWAFWETKKNLIRSEELSFTN- rEBOV548/rEBOV520
6MAM ------------------------------------------------------------------- ADI-15946
6QD7 YVQLESRFTPQFLLQLNETIYTSGKRSNTTGKLIWKVNPEIDTTIGEWAFWETKKNLIRSEELSFTVV 3T0331
6N7J ------------------------------------------------------------------- BDBV223
6EAY YVQLESRFTPQFLLQLNETIYTSGKRSNTTGKLIWKVNPEIDTTIGEWAFWETKKNLIRSEELSFTVV CA45

     502                        545                  619
5KEN --IVNAQPKCNPNLHYWTTQDEGAAITEGLMHNQDGLICGLRQLANETTQAL---------------- C4G7
5KEL EAIVNAQPKCNPNLHYWTTQDEGAAITEGLMHNQDGLICGLRQLANETTQALTDKIDQIIHDFVDKTL C2G4/C13C6
3CSY EAIVNAQPKCNPNLHYWTTQDEGAAITEGLMHNQDGLICGLRQLANETTQALTDKIDQIIHDFVD--- KZ52
3S88 QTNTKATGKCNPNLHYWTAQEQHNAATEGLMHNQNALVCGLRQLANETTQAL--TSPIVKSFNRN--- 16F6
6EA5 --TLRTQAKCNPNLHYWTTQDEGAAITEGIMHNQNGLICGLRQLANETTQAL---------------- ADI-15878
5FHC EAIVNAQPKCNPNLHYWTTQDEGAAIIEGLMHNQDGLICGLRQLANETTQAL---------------- mAB100/mAB114
6PCI EVIVNAQPKCNPNLHFWTTQDEGAAITEGLMHNQDGLICGLRQLANETTQALTDKIDQIIHDDDDKAG rEBOV548/rEBOV520
6MAM EAIVNAQPKCNPNLHYWTTQDEGAAIIEGLMHNQDGLICGLRQLANETTQAL---------------- ADI-15946
6QD7 EAIVNAQPKCNPNLHYWTTQDEGAAIIEGLMHNQDGLICGLRQLANETTQALTDKIDQIIHDFVDGSG 3T0331
6N7J ------------------------------------------------------TDKIDQIIHDFIDKPL BDBV223
6EAY EAIVNAQPKCNPNLHYWTTQDEGAAITEGLMHNQDGLICGLRQLANETTQALTDKIDQIIHDFVDKTL CA45
```

GP1

GP2

fig. S5. Structural analysis of known GP/antibody complexes. (A) Molecular surface models of GPΔmuc-WL^{2}P^2/antibody complexes by docking the GPΔmuc-WL^{2}P^2-foldon structure into previously determined GP/antibody complexes. Antibody heavy and light chains are shown in red and yellow molecular surfaces, respectively. **(B)** Sequence analysis of antibody-contacting residues (≤ 4.0 Å) in GP1 and GP2. In ClustalW alignment, contacting residues shared by at least two antibodies are colored in red, while contacting residues unique to the antibody in blue.

fig. S6

A

Dimeric locking domains (LD) for stabilizing the NP-forming interface

>**LD1** 1NI8_A (**40aa** after C-terminal deletion)
SEALKILNNIRTLRAQARECTLETLEEMLEKLEVVVNERR~~**EEESAA**~~

>**LD2** 4AYA_B (**44aa** after N-/C-terminal deletion)
MNDCYSKLKELVPSIPQNKKVSKMEILQHVIDYILDLQIALDSH

>**LD3** 1OVX_A (**50aa** after N-terminal deletion)
~~**GHHHHHHTDKRKDGSGK**~~LLYCSFCGKSQHEVRKLIAGPSVYICDECVDLCNDIIREEIKEVAPHRER

>**LD4** 2MG4_A (**58aa** after N-terminal deletion)
~~**MEKRPRTE**~~FSEEQKKALDLAFYFDRRLTPEWRRYLSQRLGLNEEQIERWFRRKEQQIGWSHPQFEK

>**LD5** 2JV7_A (**78aa, without deletion**)
DQPSVGDAFDKYNEAVRVFTQLSSAANCDWAACLSSLSASSAACIAAVGELGLDVPLDLACAATATSSATEACKGCLW

>**LD6** 1JR5_A (88aa after N-terminal deletion)
~~**MN**~~KNIDTVREIITVASILIKFSREDIVENRANFIAFLNEIGVTHEGRKLNQNSFRKIVSELTQEDKKTLIDEFNEGFEGVYRYLEMYTNK

>**LD7** 1PZQ_A (46aa after N-/C-terminal deletion)
~~**GSAA**~~SPAVDIGDRLDELEKALEALSAEDGHDDVGQRLESLLRRWNSRRAD~~**APSTSAISED**~~

>LD8 1R2A_A (**39aa** after N-terminal deletion)
~~**HMGHIQI**~~PPGLTELLQGYTVEVLRQQPPDLVDFAVEYFTRLREARR

>LD9 2JRX_A (**65aa** after N-/C-terminal deletion and glycan deletion)
~~**MPQISR**~~YSDEQVEQLLAELLNVLEKHKAPTDLSLMVLGNMVTNLINT**A**IAPAQRQAIANSFARALQSSINE~~**DKAHLEHHHHHH**~~

B

Antigenic evaluation of NPs presenting a stabilized GPΔmuc trimer

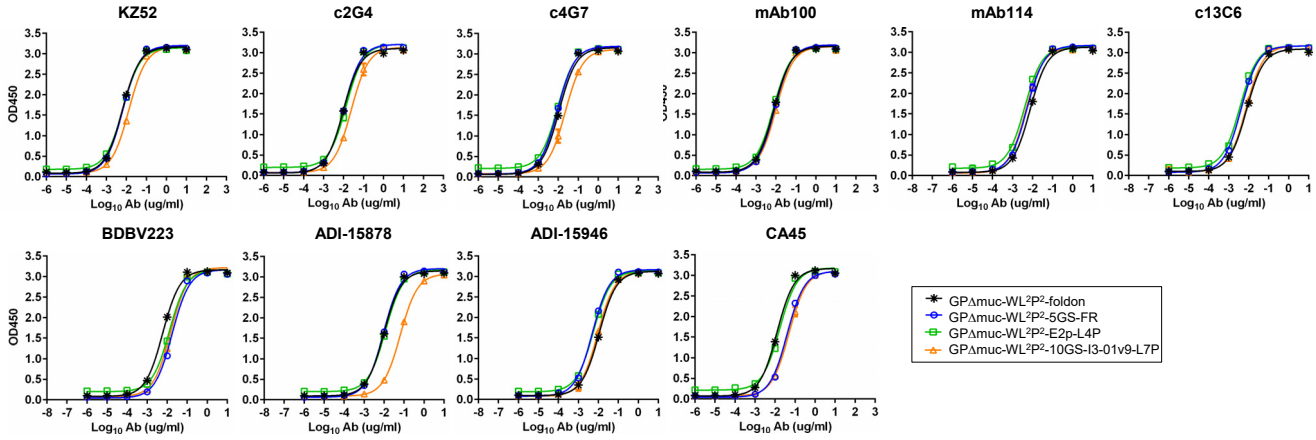

C

EC_{50} values of EBOV GPΔmuc trimer and nanoparticles binding to 10 antibodies [a].

	KZ52	c2G4	c4G7	mAb100	mAb114	c13C6	BDBV223	ADI-15878	ADI-15946	CA45
GPΔmuc-WL^2P^2-foldon	0.006	0.010	0.011	0.008	0.007	0.008	0.006	0.010	0.011	0.012
GPΔmuc-WL^2P^2-5GS-FR	0.007	0.010	0.009	0.009	0.005	0.004	0.018	0.009	0.005	0.040
GPΔmuc-WL^2P^2-E2p-L4P	0.007	0.013	0.009	0.008	0.004	0.004	0.013	0.012	0.006	0.017
GPΔmuc-WL^2P^2-10GS-I3-01v9-L7P	0.013	0.024	0.023	0.010	0.005	0.007	0.015	0.065	0.009	0.049

[a] EC_{50} values were calculated from the besting fitting in GraphPad Prism 8.4.3.

fig. S6

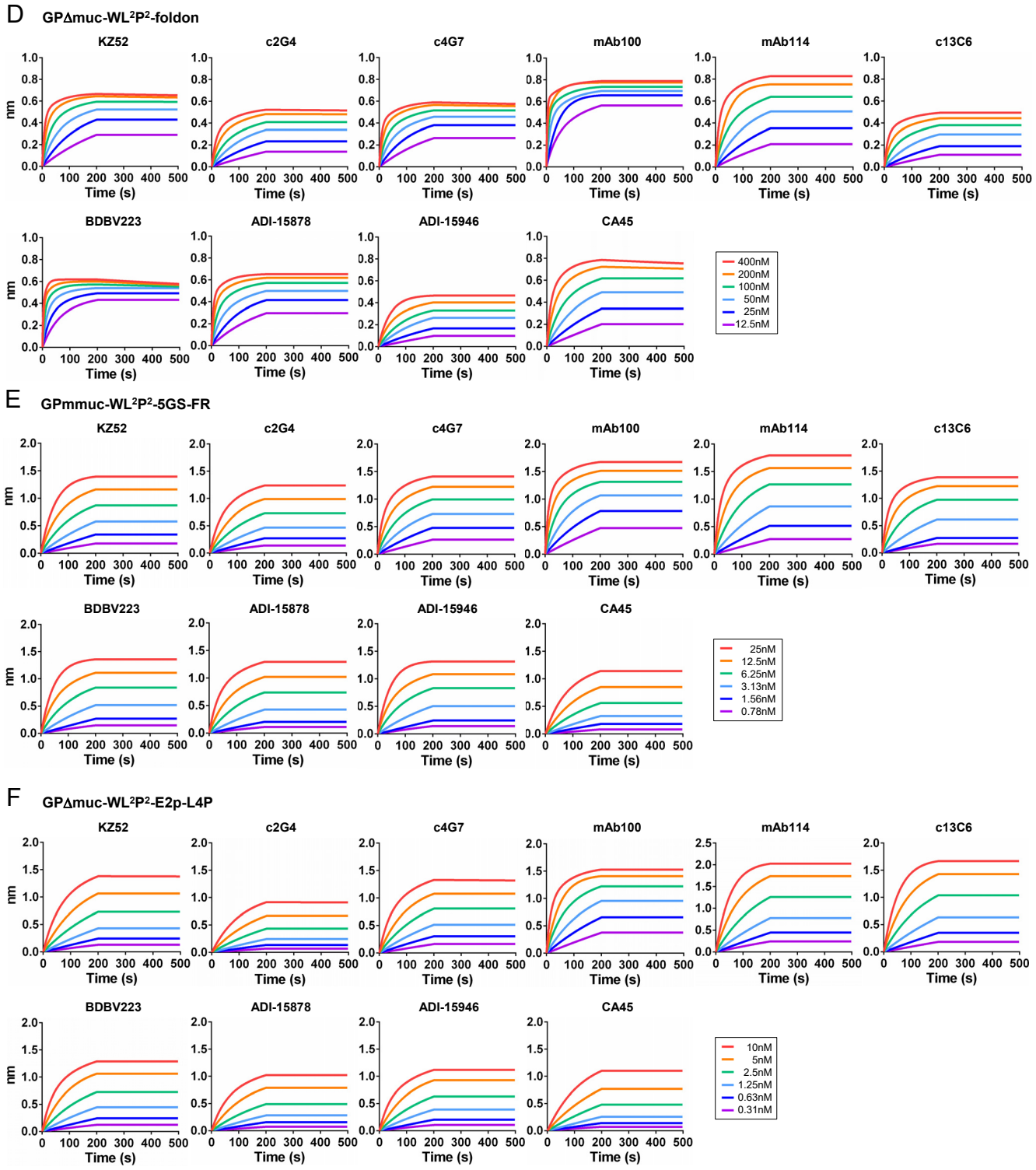
D
GPΔmuc-WL²P²-foldon
KZ52
c2G4
c4G7
mAb100
mAb114
c13C6
BDBV223
ADI-15878
ADI-15946
CA45
nm
Time (s)
400nM
200nM
100nM
50nM
25nM
12.5nM
E
GPmmuc-WL²P²-5GS-FR
25nM
12.5nM
6.25nM
3.13nM
1.56nM
0.78nM
F
GPΔmuc-WL²P²-E2p-L4P
10nM
5nM
2.5nM
1.25nM
0.63nM
0.31nM

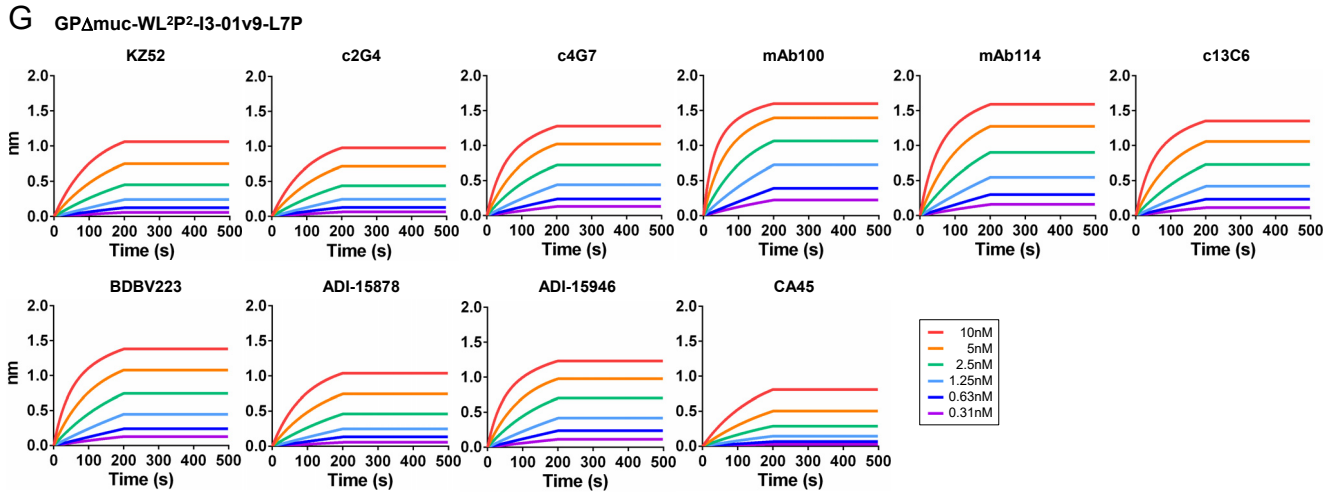

fig. S6. Design and characterization of multilayered EBOV GPΔmuc-presenting NPs. (A) Locking domains (LD) identified from the Protein Data Bank (PDB) for stabilizing the NP-forming interface. In addition to sequences, PDB IDs and number of residues after N- and C-terminal deletion are provided. **(B)-(C)** Antigenic evaluation by ELISA. Binding of FR and reengineered 60-meric E2p (E2p-LD4-PADRE, or E2p-L4P) and I3-01v9 (I3-01v9-LD7-PADRE, or I3-01v9-L7P) NPs that present a stabilized GPΔmuc-WL^{2}P^2 trimer to 10 antibodies with ELISA curves shown in **(B)** and EC_{50} values (μg/ml) summarized in **(C)**. All GP-NPs were expressed transiently in ExpiCHO cells, purified by a mAb100 column, and further purified by SEC on a Superose 6 10/300 GL column. **(D)-(G)** Antigenic evaluation by BLI using Octet96. Binding kinetics of GPΔmuc-WL^{2}P^2-foldon **(D)** and GPΔmuc-WL^{2}P^2 on FR **(E)**, E2p-L4P **(F)**, and I3-01v9-L7P **(G)** NPs to 10 antibodies. BLI sensorgrams were obtained from an Octet RED96 instrument using a series of six concentrations (400-12.5 nM by twofold dilution for GPΔmuc; 25-0.78 nM and 10-0.31 nM by twofold dilution for FR and E2p-L4p/I3-01v9-L7P, respectively) and quantitation biosensors (see Materials and Methods). I3-01v9 is a variant of I3-01 with a redesigned NP-forming interface based on the PDB structure (1VLW). I3-01v9 was reported in our previous study with a construct name “1VLW-v9”.

fig. S7

A

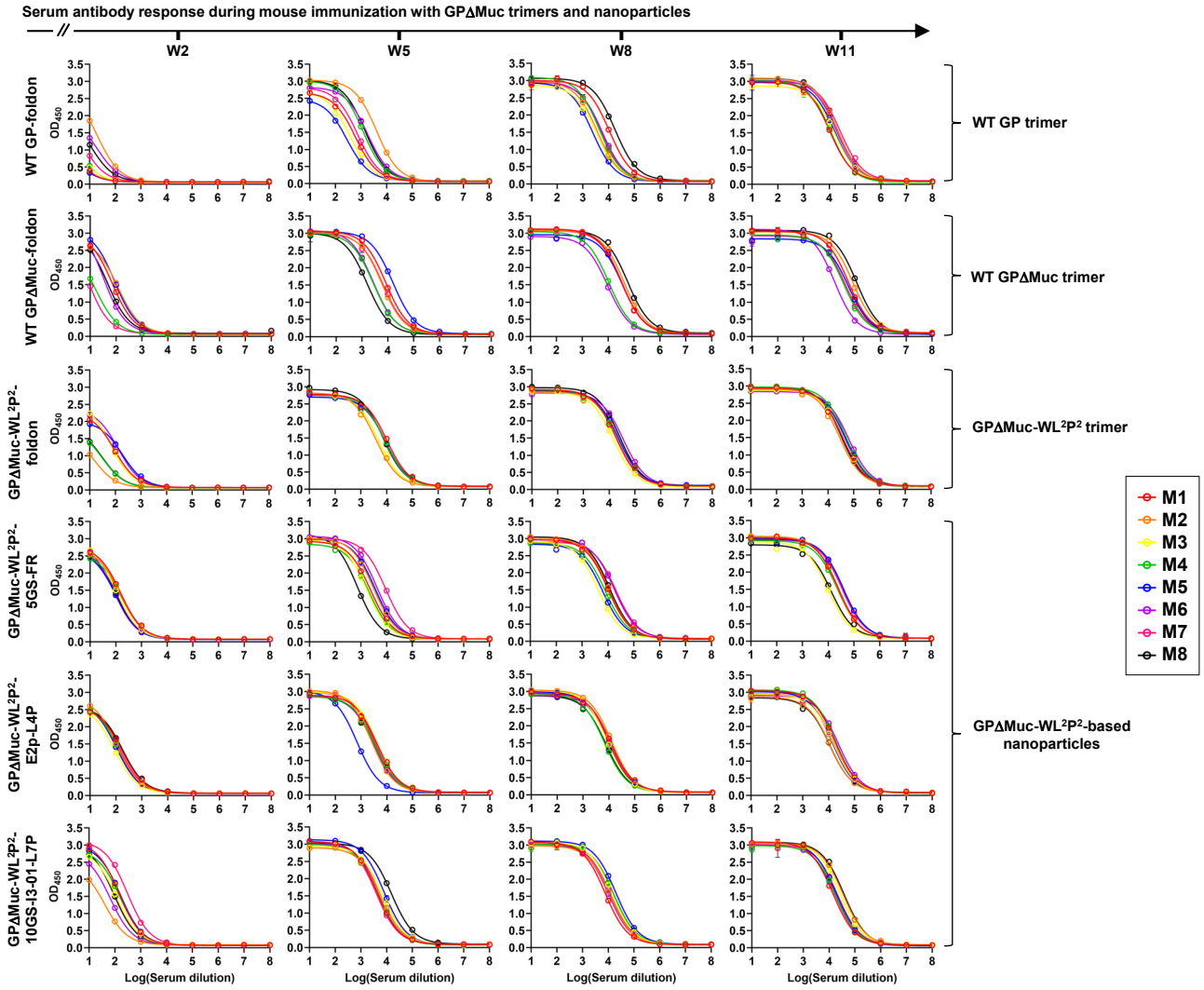

B

EC_{50} titers (fold of dilution) of mouse sera binding to EBOV GP trimers[a]

	W2			W5			W8			W11		
	WT GP-Foldon	WT GPΔMuc-foldon	GPΔMuc-WL2P2-foldon	WT GP-Foldon	WT GPΔMuc-foldon	GPΔMuc-WL2P2-foldon	WT GP-Foldon	WT GPΔMuc-foldon	GPΔMuc-WL2P2-foldon	WT GP-Foldon	WT GPΔMuc-foldon	GPΔMuc-WL2P2-foldon
M1	<1	71	93	607	8377	10280	10740	32034	18532	10467	56041	36300
M2	21	119	14	4050	5879	3894	3663	40677	20082	20353	83513	28303
M3	5	–	67	376	–	4851	3323	–	14595	16418	–	37914
M4	1	16	31	1183	2755	8470	4338	10690	19570	11262	37135	49211
M5	3	89	187	289	15768	8994	2382	35240	22712	16546	56785	46695
M6	20	31	127	1804	2752	8816	5651	9447	35455	18888	16351	64055
M7	5	7	–	740	6293	–	5066	33547	–	26293	42415	–
M8	12	46	31	1449	1591	7248	17622	56265	25518	20626	117745	33217

[a] The EC_{50} values were calculated from the besting fitting in GraphPad Prism 8.

C

EC_{50} titers (fold of dilution) of mouse sera binding to EBOV GPΔMuc-WL²P²-presenting nanoparticles [a]

	W2			W5			W8			W11		
	GPΔMuc-WL²P²-5GS-FR	GPΔMuc-WL²P²-E2p-L4P	GPΔMuc-WL²P²-10GS-I3-01v9-L7P	GPΔMuc-WL²P²-5GS-FR	GPΔMuc-WL²P²-E2p-L4P	GPΔMuc-WL²P²-10GS-I3-01v9-L7P	GPΔMuc-WL²P²-5GS-FR	GPΔMuc-WL²P²-E2p-L4P	GPΔMuc-WL²P²-10GS-I3-01v9-L7P	GPΔMuc-WL²P²-5GS-FR	GPΔMuc-WL²P²-E2p-L4P	GPΔMuc-WL²P²-10GS-I3-01v9-L7P
M1	153	172	148	2367	4154	4389	9932	11715	7637	24325	17631	13984
M2	146	112	41	3115	2559	5927	10324	12671	11689	22640	11150	34464
M3	102	86	115	1691	4077	7196	4239	8701	14184	10166	15309	26621
M4	159	121	159	2053	3426	4860	7750	6774	16144	23135	18605	18439
M5	99	106	165	3598	692.1	8006	6227	9166	19698	38846	13793	19315
M6	84	105	67	4238	2973	5440	17428	12140	10331		24189	17649
M7	101	142	305	9029	3443	3872	20184	10342	11975	34598	15778	21201
M8	104	178	93	725.6	3022	15325	11421	7550	16234	13170	11012	37636

[a] The EC_{50} values were calculated from the besting fitting in GraphPad Prism 8.

D

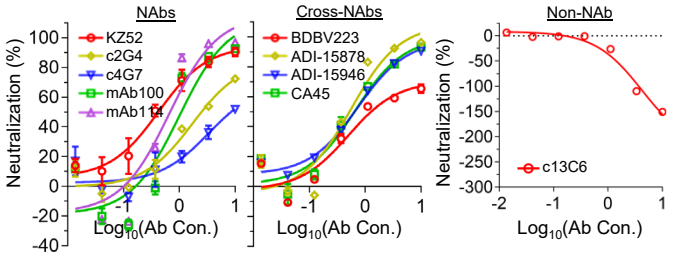

E

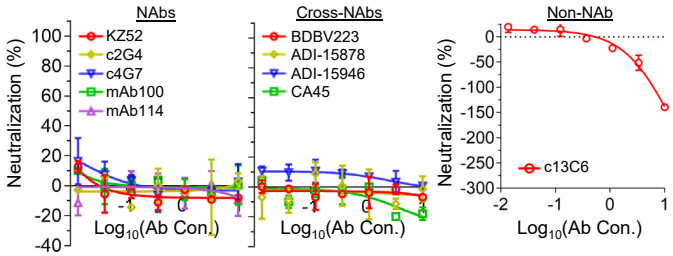

F

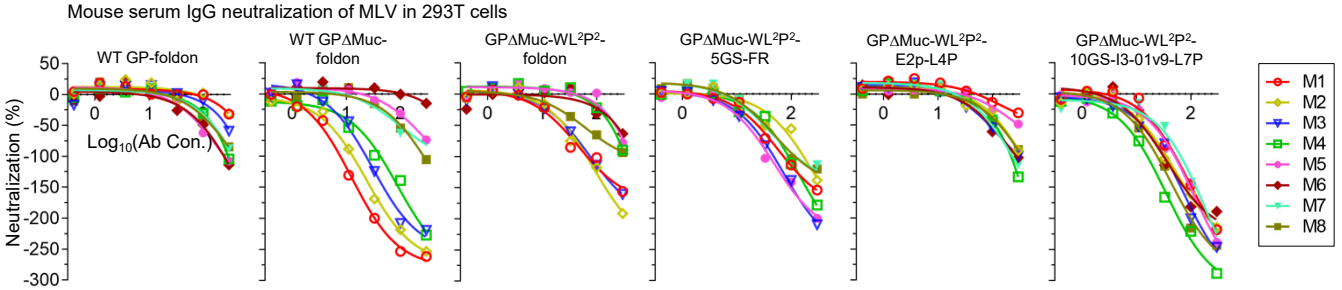

fig. S7. Immunogenicity assessment of EBOV GP/GPΔmuc trimers and GPΔmuc-presenting NPs in BALB/c mice. (A) ELISA binding curves of mouse serum from three trimer groups, in which mice were immunized with WT GP-foldon, GPΔMuc-foldon, and GPΔMuc-WL²P²-fold trimers, and three NP groups, in which mice were immunized with FR, E2p-L4P, and I3-01v9-L7P NPs presenting GPΔMuc-WL²P², to GPΔMuc-WL²P² at w2, w5, w8, and w11. **(B)** EC_{50} titers measured for the three trimer groups. **(C)** EC_{50} titers measured for the three NP groups. The EC_{50} titer was measured in the unit of fold of dilution. Of note, serum binding at w2 did not reach the plateau (or saturation) to allow for accurate determination of EC_{50} titers. Nonetheless, the EC_{50} values calculated in Prism were used as a quantitative measure of binding antibody titers to facilitate the comparison of different vaccine groups at w2. **(D)** Ebolavirus-pp (Makona C15) neutralization by 10 ebolavirus-specific antibodies in TZM-bl cells. **(E)** MLV-pp neutralization by 10 ebolavirus-specific antibodies in 293 T cells. **(F)** MLV-pp neutralization by purified mouse serum IgGs in 293 T cells starting at 300μg/ml with three-fold dilution. Mouse IgGs were collected from all six vaccine groups at w11.

fig. S8

A

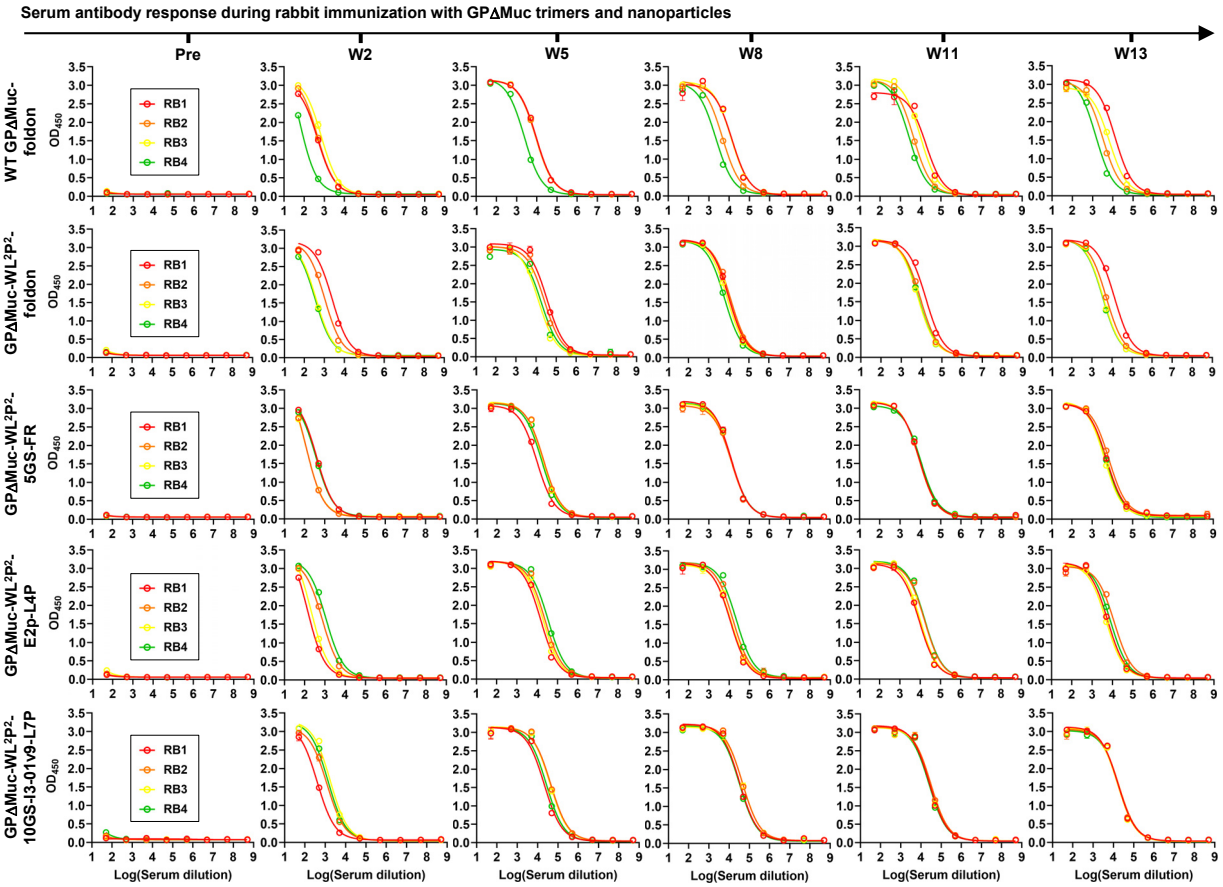

B

EC_{50} titers (fold of dilution) of rabbit sera binding to EBOV GP trimers[a]

	W2		W5		W8		W11		W13	
	WT GPΔMuc-foldon	GPΔMuc-WL2P2-foldon	WT GPΔMuc-foldon	GPΔMuc-WL2P2-foldon	WT GPΔMuc-foldon	GPΔMuc-WL2P2-foldon	WT GPΔMuc-foldon	GPΔMuc-WL2P2-foldon	WT GPΔMuc-foldon	GPΔMuc-WL2P2-foldon
M1	464	2428	9404	35115	13868	10110	18135	16116	12777	13338
M2	456	1044	8904	26144	4647	12073	4446	8694	3143	5177
M3	701	378	8943	13273	12652	8363	9807	6517	6681	3586
M4	57	336	2392	18008	2220	6092	2663	6901	1443	3424

[a] The EC_{50} values were calculated from the besting fitting in GraphPad Prism 8.4.3.

EC_{50} titers (fold of dilution) of mouse sera binding to EBOV WT GPΔMuc-presenting nanoparticles [a]

	W2			W5			W8			W11		
	WT GPΔMuc-5GS-FR	WT GPΔMuc-E2p-L4P	WT GPΔMuc-10GS-I3-01v9-L7P	WT GPΔMuc-5GS-FR	WT GPΔMuc-E2p-L4P	WT GPΔMuc-10GS-I3-01v9-L7P	WT GPΔMuc-5GS-FR	WT GPΔMuc-E2p-L4P	WT GPΔMuc-10GS-I3-01v9-L7P	WT GPΔMuc-5GS-FR	WT GPΔMuc-E2p-L4P	WT GPΔMuc-10GS-I3-01v9-L7P
M1	393	133	404	9406	14736	21261	12961	11405	32895	9041	8972	26363
M2	117	735	1207	20093	23950	44607	12927	15609	45311	8893	16560	31073
M3	120	201	1774	18894	19727	41440	12770	12457	47664	8644	9954	28526
M4	368	1126	1382	16116	34695	27116	13140	22771	32291	10558	16803	25205

	W13		
	WT GPΔMuc-5GS-FR	WT GPΔMuc-E2p-L4P	WT GPΔMuc-10GS-I3-01v9-L7P
M1	5272	5795	16907
M2	6817	12387	18398
M3	4146	4889	16645
M4	5047	8066	18753

The EC_{50} values were calculated from the besting fitting in GraphPad Prism 8.4.3.

fig. S8

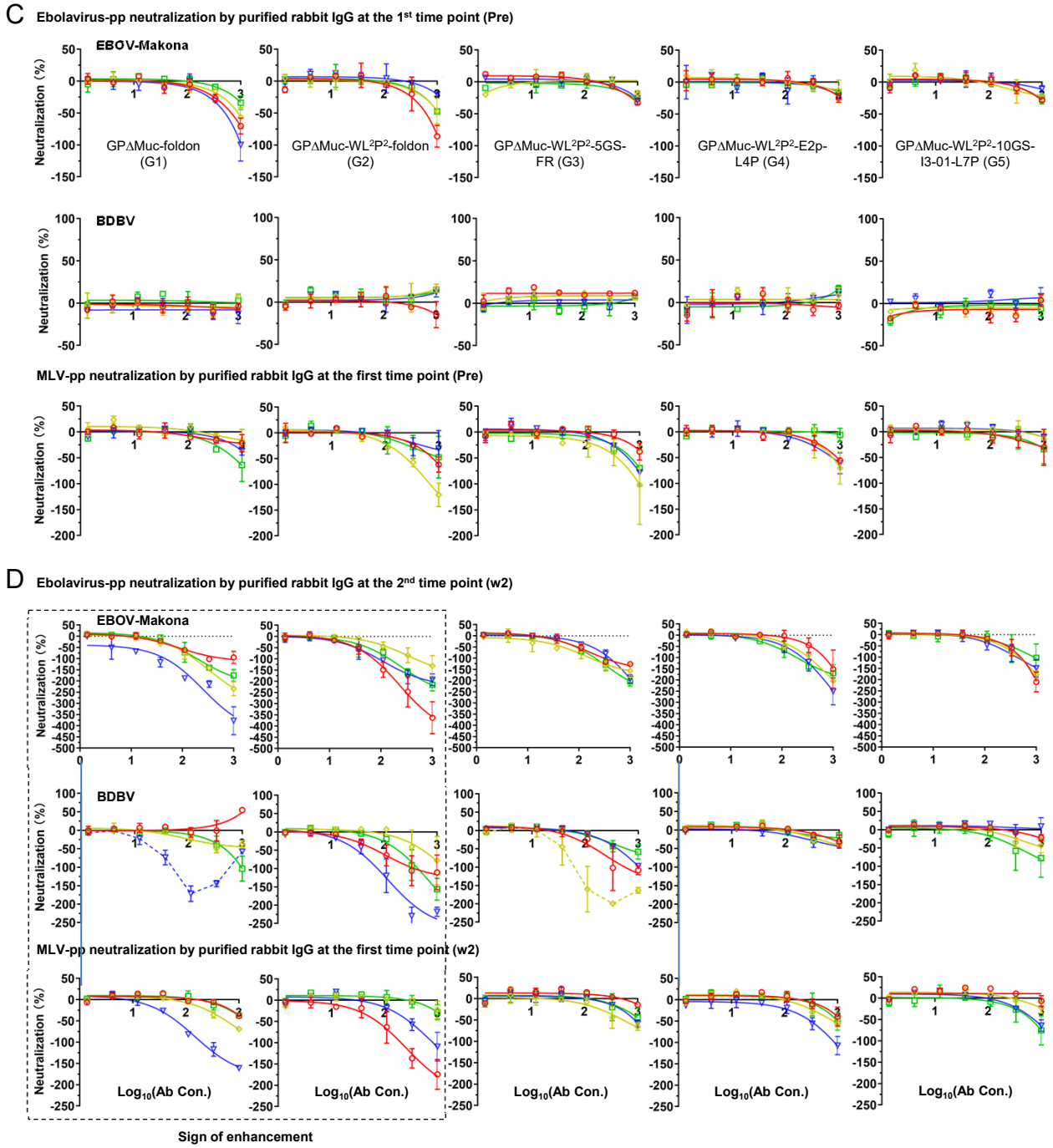
C
Ebolavirus-pp neutralization by purified rabbit IgG at the 1st time point (Pre)
EBOV-Makona
BDBV
Neutralization (%)
GPΔMuc-foldon (G1)
GPΔMuc-WL2P2-foldon (G2)
GPΔMuc-WL2P2-5GS-FR (G3)
GPΔMuc-WL2P2-E2p-L4P (G4)
GPΔMuc-WL2P2-10GS-I3-01-L7P (G5)
MLV-pp neutralization by purified rabbit IgG at the first time point (Pre)
D
Ebolavirus-pp neutralization by purified rabbit IgG at the 2nd time point (w2)
EBOV-Makona
BDBV
MLV-pp neutralization by purified rabbit IgG at the first time point (w2)
Log10(Ab Con.)
Sign of enhancement

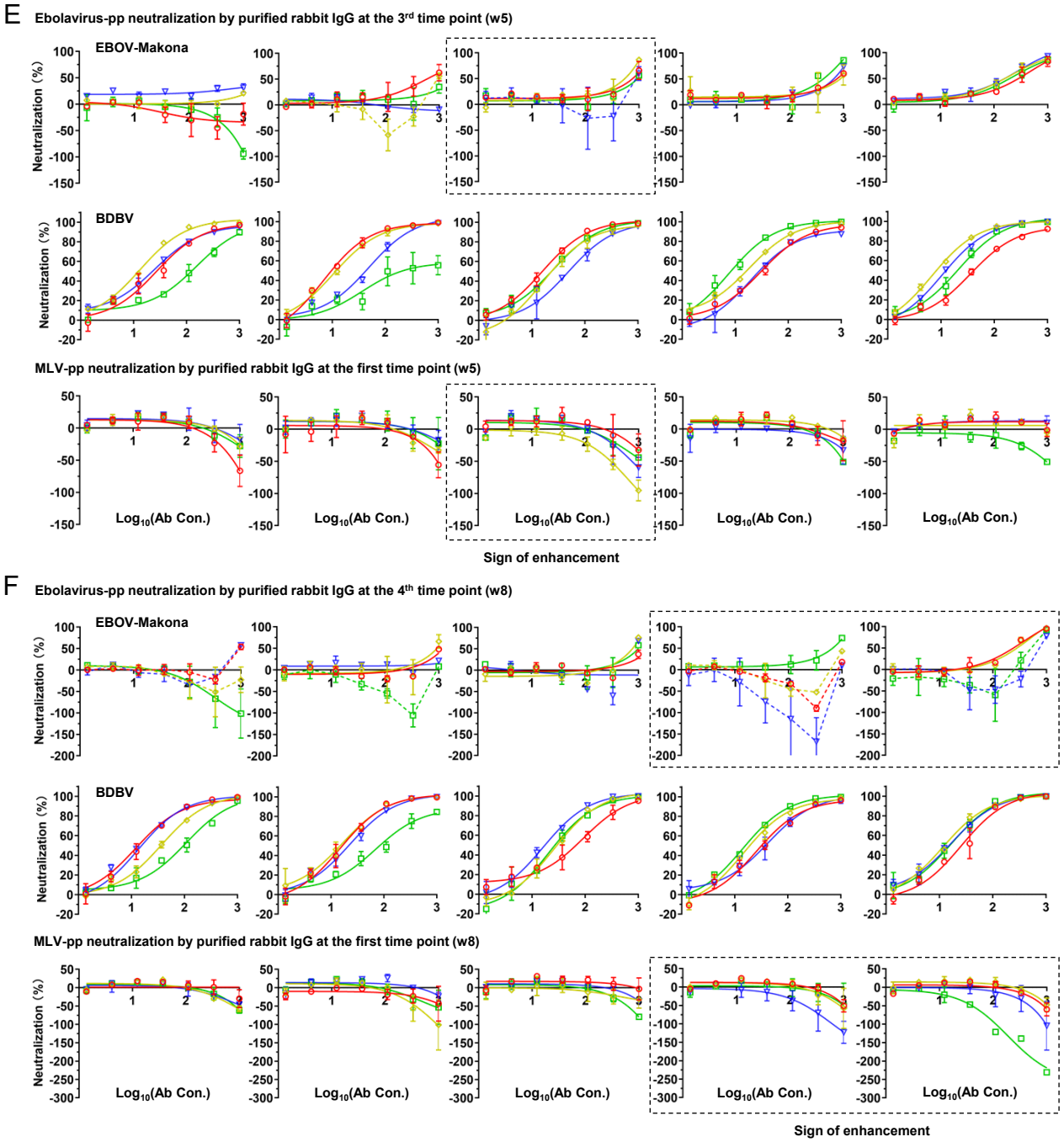

fig. S8. Immunogenicity assessment of EBOV GP/GPΔmuc trimers and GPΔmuc-presenting NPs in rabbits. (A) ELISA binding curves of rabbit serum from two trimer groups, in which rabbits were immunized with GPΔMuc-foldon and GPΔMuc-WL^{2}P^2-fold trimers, and three NP groups, in which rabbits were immunized with FR, E2p-L4P, and I3-01v9-L7P NPs presenting GPΔMuc-WL^{2}P^2, to GPΔMuc-WL^{2}P^2 at w0, w2, w5, w8, w11, and w13. **(B)** EC_{50} titers measured for the two trimer groups and three NP groups. The EC_{50} titer was measured in the unit of fold of dilution. Of note, serum binding at w2 did not reach the plateau (or saturation), but the OD_{450} values were approximately at the same level as those obtained at w5 (fully plateaued). Therefore, the EC_{50} values calculated in Prism were considered sufficiently accurate to facilitate the comparison of different vaccine groups at w2. Ebolavirus-pp (EBOV-Makona and BDBV) and MLV-pp neutralization by purified rabbit IgGs from w2, w5, and w8 in 293 T cells is shown in **(C)**, **(D)**, **(E)** and **(F)**. Data points that do not fit a sigmodal dose response model are shown as dashed lines. Signs of enhanced pseudovirus infection for the two GPΔmuc trimer groups, the FR group, and the two multilayered 60-meric NP groups are observed at w2, w5, and w8, respectively, and are highlighted in dashed rectangles.

fig. S9

A

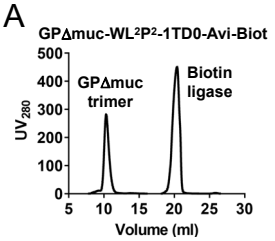

B

EBOV GPΔmuc-specific sorting of mouse splenic B cells from five vaccine groups

GPΔmuc-Foldon			GPΔmuc-WL²P²-Foldon			GPΔmuc-WL²P²-5GS-FR			GPΔmuc-WL²P²-E2p-L4P			GPΔmuc-WL²P²-10GS-I3-01v9-L7P		
Mouse	Sorted B cells	%Splenic B cells	Mouse	Sorted B cells	%Splenic B cells	Mouse	Sorted B cells	%Splenic B cells	Mouse	Sorted B cells	%Splenic B cells	Mouse	Sorted B cells	%Splenic B cells
G5-1	760	0.03579	G7-1	1134	0.07849	G3-1	1856	0.07481	G4-1	1360	0.07285	G10-2	401	0.07874
G5-3	582	0.04646	G7-3	585	0.18874	G3-2	1146	0.04230	G4-2	906	0.09027	G10-3	602	0.10956
G5-6	857	0.04580	G7-4	1043	0.18983	G3-5	1362	0.04844	G4-3	1369	0.08957	G10-4	443	0.06507
G5-7	1065	0.04149	G7-6	949	0.19321	G3-7	2864	0.10775	G4-6	1400	0.08291	G10-5	871	0.04330
G5-8	752	0.04904	G7-8	982	0.09138	G3-8	843	0.06591	G4-7	1485	0.05536	G10-8	372	0.05807

C

Next-generation sequencing (NGS) data obtained for Ebola GP-specific mouse splenic B cells [a]

Vaccine antigen	Mouse	Chain	N_{Chain}	N_{Step5}	<Length>	N_{Usable}
GPΔmuc -foldon	G5-1	H [b]	241,888	152,926	369.7	83,074
		K	320,999	271421	335.3	244,765
	G5-3	H [b]	151,041	38,965	365.7	25,901
		K	254,461	190,810	332.5	159,340
	G5-6	H	164,049	72,966	364.3	54,123
		K	149,922	122,358	328.8	112,897
	G5-7	H [b]	127,583	31,333	362.8	21,695
		K	132,822	101,243	331.6	86,936
	G5-8	H [b]	416,364	146,889	363.5	98,999
		K	319,964	245,757	331.5	219,409
GPΔmuc-WL²P² -foldon	G7-1	H [b]	372,642	174,424	363.5	116,260
		K	147,494	121,251	330.8	107536
	G7-3	H [b]	225,662	109,976	363.4	75,064
		K	207,512	158,440	332.6	142,203
	G7-4	H [b]	195,714	58,996	364.4	39,423
		K	181,907	143,388	333.8	126,382
	G7-6	H [b]	203,093	49,877	361.0	34,366
		K	234,578	193,315	334.7	174,967
	G7-8	H [b]	193,745	96,042	352.4	75,369
		K	166,563	138,767	334.7	118,193
GPΔmuc-WL²P² -5GS-FR [c]	G3-1	H [b]	181,414	15,426	361.6	9,391
		K	172,971	110,166	333.9	99,231
	G3-2	H [b]	196,037	24,375	366.4	15,433
		K	165,297	118,826	332.0	106,667
	G3-5	H [b]	171,116	13,134	367.4	8,154
		K	202,059	149,466	335.5	133,378
	G3-7	H [b]	149,991	10,289	365.4	6,028
		K	192,304	132,601	329.7	120,184
	G3-8	H	250,631	171,124	362.3	132,011
		K	234,322	162,071	328.2	139,171

Vaccine antigen	Mouse	Chain	N_{Chain}	N_{Usable}	<Length>	$Perc_{Usable}$
GPΔmuc-WL²P² -E2p-L4P	G4-1	H	132,044	55,538	362.8	42,292
		K	173,895	138,355	331.8	118,788
	G4-2	H	95,696	71,107	360.5	57,045
		K	155,727	132,125	335.0	117,275
	G4-3	H	105,559	85,392	362.1	72,646
		K	75,330	59,105	332.3	48,150
	G4-6	H	139,269	106,616	365.5	84,238
		K	146,092	113,590	335.2	105,666
	G4-7	H [b, d]	672,503	542,016	365.2	369,668
		K	519,784	405,118	333.6	362,987
GPΔmuc-WL²P² -10GS-I3-01v9 -L7P	G10-2	H	452,882	268,275	365.5	212,617
		K	290,177	258,708	328.5	233,447
	G10-3	H	470,021	278,422	362.0	210,314
		K	223,350	207,358	333.2	191,472
	G10-4	H	297,056	261,706	363.5	215,196
		K	226,568	203,176	336.7	187,416
	G10-5	H	190,727	138,889	366.4	106,419
		K	237,420	197,478	331.3	183,103
	G10-8	H	260,502	90,086	364.6	72,427
		K	350,497	270,707	334.3	229,614

[a] Listed items include the vaccine antigen, mouse sample ID, number of VH/VK chains prior to the antibodyomics pipeline processing, number of VH/VK chains at step 5 of the pipeline processing, average read length, and number of usable chains after removing fragments with a V-gene alignment of 250bp or shorter.

[b] Due to the difficulty in library preparation, a smaller heavy chain dataset was obtained for a number of mouse samples, especially those from the trimer and FR groups. Two additional Ion S5 sequencing runs using the Ion 530 chip was performed to obtain more heavy chain reads to facilitate the profile analysis.

[c] G3-1, 5, and 7 showed especially low read-out and the profiles were only used for qualitative comparison with other vaccine groups but not for statistical analysis.

[d] Due to the large size of the dataset obtained from the additional NGS run, pre-filtering with a read length cutoff of 400bp was performed before merging it with the heavy chain dataset obtained from the initial run.

D

GPΔmuc-foldon group

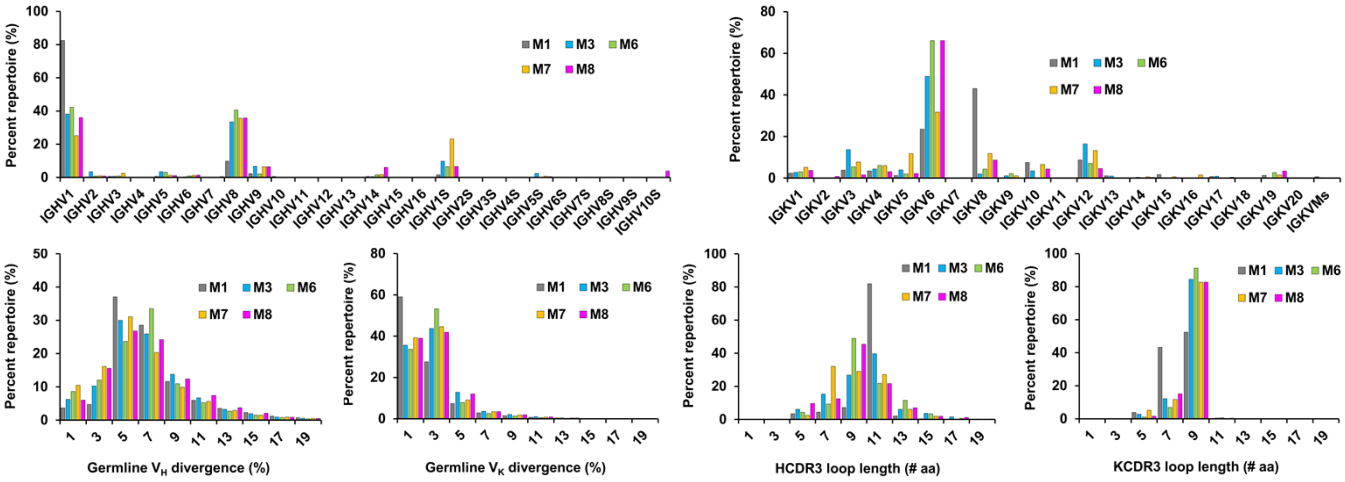

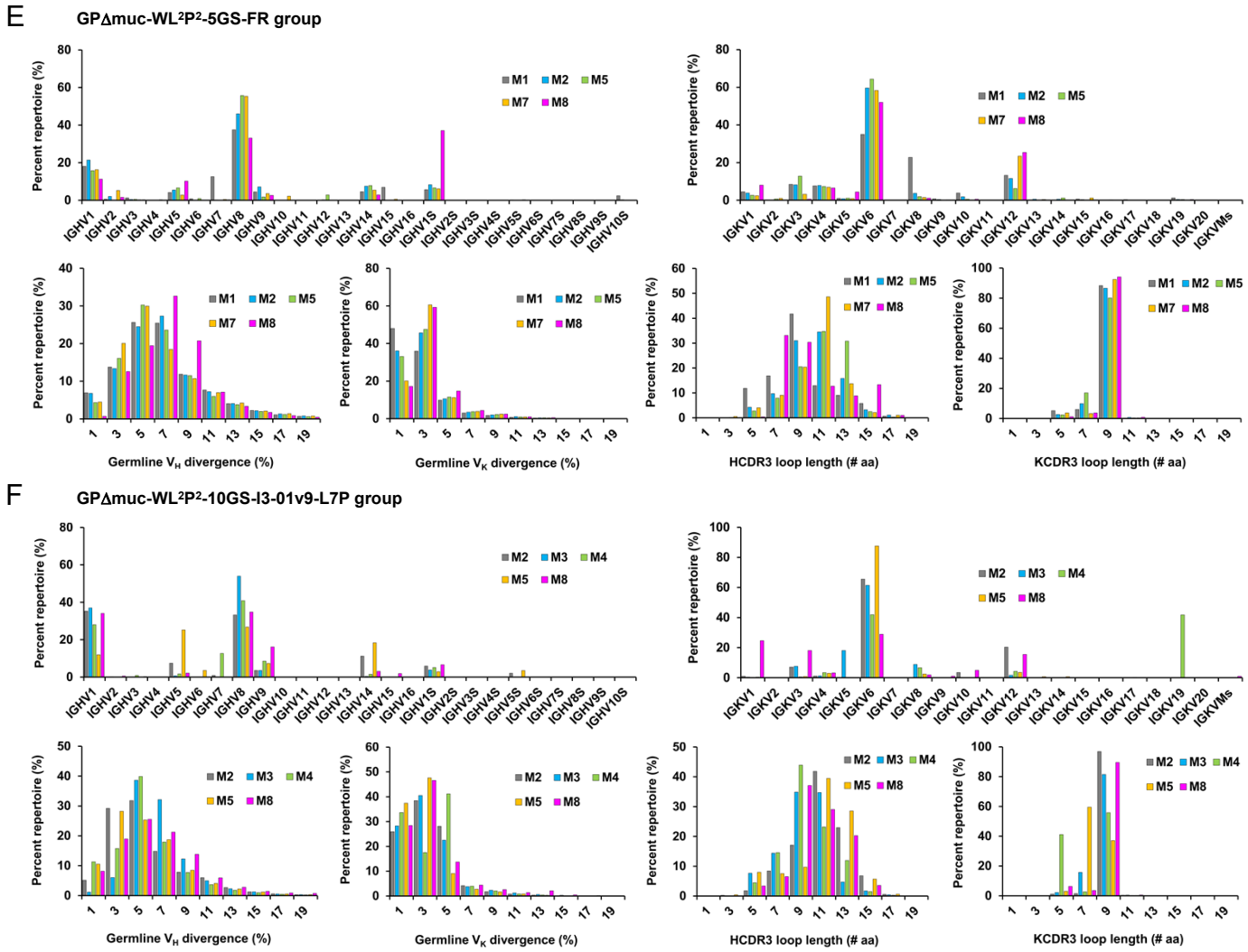

fig. S9. Unbiased NGS repertoire analysis of bulk-sorted Ebola GP-specific mouse splenic B cells. (**A**) SEC profile of a biotinylated Avi-tagged Ebola GPΔmuc trimer, termed GPΔmuc-WL^{2}P^2-1TD0-Avi-Biot, obtained from a HiLoad Superdex 200 16/600 column. 1TD0 is a trimeric scaffold used to stabilize GPΔmuc in a trimeric state and to deselect B cells directed to foldon in the two trimer groups. (**B**) Summary of Ebola GPΔmuc-specific bulk sorting of mouse splenic B cells from five vaccine groups. (**C**) Antibodyomics analysis of NGS data obtained for Ebola GPΔmuc-specific mouse splenic B cells. Distribution of critical B-cell properties are shown for three vaccine groups, in which mice were immunized with **(D)** GPΔmuc-foldon, **(E)** GPΔmuc-WL^{2}P^2-5GS-FR, and **(F)** GPΔmuc-WL^{2}P^2-10GS-I3-01v9-L7P. For each group, distributions are shown for germline VH/VK gene usage (top), germline VH/VK divergence (bottom left) and CDRH/K3 loop length (bottom right).

Table S1. Data collection and refinement statistics for redesigned EBOV GPΔmuc trimers.

Data Collection	**GPΔmuc-WL^2-foldon**	**GPΔmuc-WL^{2}P^2-foldon**
Beamline	APS 23-ID-D	SSRL 12-2
Wavelength (Å)	1.0332	0.97946
Resolution (Å)[a]	49.05-2.28 (2.34-2.28)	49.39-3.20 (3.26-3.20)
Space group	R32	P321
Unit cell (Å) (°)	114.58, 114.58, 312.38 90 90 120	114.06, 114.06, 136.22 90 90 120
Total reflections	156,593	153,527
Unique reflections	34,904 (1725)	17343 (864)
Multiplicity	4.5 (3.3)	8.9 (8.7)
Completeness (%)	96.4 (97.3)	99.9 (99.8)
Mean (I)/ σ_I	8.0 (0.9)	8.4 (0.45)
R_{meas}[c](%)	16.8 (147)	31.9 (557)
R_{pim}[d](%)	7.4 (77.5)	10.8 (187)
$CC_{1/2}$[e](%)	78.1 (32.5)	77.6 (31.3)
Refinement		
Refinement resolution (Å)[a]	49.05-2.28 (2.34-2.28)	49.39 - 3.20 (3.26 - 3.20)
# reflections in refinement (work/free)	33188/1715	16245/837
R_{work} (%)	19.7 (34.8)	28.5 (51.3)
R_{free} (%)	23.4 (37.5)	32.9 (48.2)
# Protein atoms	2942	3123
# Carbohydrate atoms	153	139
# Waters	66	0
# Protein residues	374	398
Bond r.m.s. deviation (Å)	0.014	0.013
Angle r.m.s. deviation (º)	1.99	1.48
Ramachandran favoured, allowed, outliers (%)(*83*)	96.9, 3.1, 0.0	92.1, 7.9, 0.0
Clashscore[f]	7.0	15.0
Wilson B (Å^2)	38	67
Average B (Å^2)	60	80
Protein	59	80
PDB ID	7JPI	7JPH

[a]Numbers in parentheses are for highest resolution shell
[b]$R_{merge} = \Sigma_{hkl} \Sigma_{i=1,n}|I_i(hkl) - \langle I(hkl)\rangle| / \Sigma_{hkl} \Sigma_{i=1,n} I_i(hkl)$
[c]$R_{meas} = \Sigma_{hkl} \sqrt{(n/n-1)} \Sigma_{i=1,n}|I_i(hkl) - \langle I(hkl)\rangle| / \Sigma_{hkl} \Sigma_{i=1,n} I_i(hkl)$
[d]$R_{pim} = \Sigma_{hkl} \sqrt{(1/n-1)} \Sigma_{i=1,n}|I_i(hkl) - \langle I(hkl)\rangle| / \Sigma_{hkl} \Sigma_{i=1,n} I_i(hkl)$
[e]$CC_{1/2}$ = Pearson Correlation Coefficient between two random half datasets
[f] Number of unfavorable all-atom steric overlaps ≥ 0.4Å per 1000 atoms